# RESEARCH PERFORMANCE FINAL REPORT

| | |
|---|---|
| **Federal Agency and Organization Element to Which Report is Submitted:** | Office of Surface Mining Reclamation and Enforcement<br>Department of Interior |
| **Federal Grant or Other Identifying Number Assigned by the Agency:** | S23AC00070-00 |
| **Name of Program Direct:** | Lisa Henderson; lhenderson@osmre.gov<br>Sean Chisholm; schisholm@osmre.gov<br>Jody Davin; jdavin@osmre.gov |
| **Project Title:** | Enhanced Dewatering of Acid Mine Drainage Sludge Using an Efficient, Low-cost, and Modular Process Circuit |
| **PI Name, Title and Contact Information:** | Wencai Zhang, Ph.D., Assistant Professor<br>Virginia Polytechnic Institute and State University<br>Holden Hall, Room 391<br>410 Old Turner St, Blacksburg, VA 24060<br>Phone: (540) 231-8110 (Work)<br>Phone: (859) 351-6264 (Mobile)<br>Email: wencaizhang@vt.edu |
| **Submission Date:** | October 18, 2025 |
| **UEI Number:** | QDE5UHE5XD16 |
| **Recipient Organization:** | Virginia Polytechnic Institute and State University (VT)<br>300 Turner St NW Suite 4200, Blacksburg, VA 24061 |
| **VT's Contract Administrator:** | Jessica Lynn Mills<br>jfahrman@vt.edu |
| **Project/Grant Period:** | 07/01/2023 – 06/30/2025 |
| **Report Authors:** | Wencai Zhang (PI), Xu Wang (Investigator), Peidong Liu (Investigator) |

# TABLE OF CONTENTS

## TABLE OF FIGURES

## TABLE OF TABLES

## 1. PUBLIC EXECUTIVE SUMMARY

### Purpose of the Research

The primary objective of this project is to develop, optimize, and validate the proposed circuit. the specific technical and economic metrics that will be achieved using the proposed circuit include: (1) solids content in the sludge is improved to greater than 30 wt.%; (2) the clean water generated from the proposed circuit complies with the coal mining effluent guidelines and standards formulated by the U.S. Environmental Protection Agency (EPA); and (3) the cost of the proposed circuit is close to or less than that of the existing circuits.

### Importance and Impact

Acid mine drainage (AMD) stands as a prevalent environmental challenge across numerous mining sites. The proposed circuit can provide a much faster dewatering kinetics for AMD sludge than conventional circuits that largely rely on sedimentation in clarifiers to achieve a satisfactory performance, normally taking several to tens of hours. The proposed circuit also has a smaller footprint and thereby a high modularity, which is a promising choice when the AMD of mining companies is distributed in different areas with relatively small volumes.

### Schedule & Milestone Status

*Task 1.0 – Sample Collection and Characterization*

- Description: Collect a sufficient volume (e.g., 250 gallon) of acid mine drainage (AMD) samples from a mining company for subsequent tests. Characterize the pH/Eh, elemental composition, redox potential, and dissolved solids of the samples.
- Task due date: 9/30/2023
- Status: Completed

*Task 2.0 – Precipitation Tests*

- Description: Determine the experimental conditions generating qualified clean water using the AMD samples collected in Task 1.0. The experimental conditions include the type and dosages (i.e., solution pH) of neutralizing agent ($Na_2CO_3$, NaOH, and CaO). The elemental

compositions of filtrate will be analyzed using inductively coupled plasma mass spectrometry (ICP-MS), to calculate metal removal and evaluate the quality of the filtrate.

- Task due date: 1/31/2024
- Status: Completed

*Task 3.0 – Precipitate Flotation Tests*

Precipitate flotation tests will be carried out in two phases, corresponding to Subtasks 3.1 and 3.2. The primary objective of this task is to optimize flotation conditions to remove over 95% of the precipitates from the solutions.

*Subtask 3.1 – Batch Flotation Tests*

- Description: In the first phase, the tests will be conducted in batch mode using a micro flotation column. The effect of flotation pH, flocculant type and dosage, collector dosage, conditioning time, frother type and dosage, and air flowrate on the flotation recovery of both precipitates and water will be evaluated through a comprehensive parametric study. The experimental conditions providing the highest recovery of precipitates, but the lowest recovery of water will be determined.
- Task due date: 5/31/2024
- Status: Completed

*Subtask 3.2 – Continuous Flotation Tests*

- Description: In the second phase, the precipitate flotation tests will be conducted in continuous mode using a flotation column. The optimum conditions determined in Subtask 3.1 will be employed to generate a sufficient volume of lower water content sludge for subsequent filtration tests.
- Task due date: 9/31/2024
- Status: Completed

*Task 4.0 – Filtration Tests*

- Description: Filtration tests will be performed on the lower water content sludge generated in Task 3.0. A benchtop plate and vacuum filtration will be used in this task. The effect of filtration time on the solids content of filter cakes will be evaluated.
- Task due date: 1/31/2025

- Status: Completed

*Task 5.0 – High-Density Sludge Tests*

- Description: The bench-scale high-density sludge experiments will be conducted to determine the optimum dewatering performance. Neutralizer (e.g. lime) and flocculant will be employed in the high-density sludge tests, and the effect of residence time in the clarifier on the sludge solids content will be evaluated.
- Task due date: 4/31/2025
- Status: Completed

*Task 6.0 – Process circuit Design and Techno-Economic Analysis*

- Description: Based on experimental tests (Tasks 2.0 - 5.0), a processing circuit will be designed for a 10,000 gallon/day capacity. Techno-economic analysis will estimate both capital and operating costs. A high-density sludge circuit with the same capacity will also be designed and estimated. Systematic comparisons between the proposed circuit and the high-density circuit will be performed in terms of different aspects, such as sludge solids content, capital and operating costs, and adoptability.
- Task due date: 7/31/2025
- Status: Completed

*Task 7.0 – Fundamental Studies*

- Description: Reveal fundamental mechanisms controlling the precipitate flotation and filtration of acid mine drainage sludge. The fundamental studies will include characterizations of sludge precipitate particles (e.g., particle size and mineralogy), mechanism of precipitation formation, and interactions between conditioners (flocculants and collectors) and sludge precipitate particles (e.g., adsorption mechanisms).
- Task due date: 7/31/2025
- Status: Completed

## 2. ACCOMPLISHMENTS AND OBJECTIVES

### 2.1 Objectives

Efficient dewatering of acid mine drainage sludge is necessary to reduce disposal costs and improve the viability of reusing the sludge for other purposes, such as low-cost adsorbents and building materials. Some existing dewatering circuits can generate sludge with as high as 30 wt.% solids content; however, nearly all the circuits rely on sedimentation in clarifiers, which is a relatively slow process and normally takes several to tens of hours. Therefore, clarifiers are required to have a large volume to provide enough residence time, and the existing circuits usually occupy a large footprint and have a low degree of modularity, which make the circuits difficult to assemble, dissemble, and relocate. As a result, the existing dewatering circuits are not suitable when the acid mine drainage of mining companies is distributed in different areas with relatively small volumes. In this case, centralized processing or installing a new processing plant in each area is unfeasible due to high transportation and construction costs. To address this dilemma, an innovative process circuit consisting of lime neutralization, precipitate flotation, and filtration is proposed, which is advantageous over the existing circuits in several aspects, such as low footprint and high modularity. The **primary objective** of this project is to develop, optimize, and validate the proposed circuit. In this project, the specific technical and economic metrics that will be achieved using the proposed circuit include: (1) solids content in the sludge is improved to greater than 30 wt.%; (2) the clean water generated from the proposed circuit complies with the coal mining effluent guidelines and standards formulated by the U.S. Environmental Protection Agency (EPA); and (3) the cost of the proposed circuit is close to or less than that of the existing circuits.

### 2.2 Approach

The primary objective of this project is to develop, optimize, and validate an efficient, cost-effective, and modular process circuit that can be used to enhance the dewatering efficiency of acid mine drainage sludge. In this project, the specific technical and economic metrics that will be achieved using the proposed circuit include: (1) solids content in the sludge is improved to greater than 30 wt.%; (2) the clean water generated from the proposed circuit complies with the coal mining effluent guidelines and standards formulated by the U.S. Environmental Protection Agency (EPA); and (3) the cost of the proposed circuit is close to or less than that of the high-density sludge

circuit. To achieve these metrics, several different experimental methodologies will be employed, and descriptions of the major methodologies are given as follows:

- *Sample Collection/Precipitation*: Acid mine drainage samples will be collected from coal mines, and upon delivery to the laboratory, the samples will be characterized and subjected to precipitation tests using lime as the neutralizing agent. The effect of lime dosage (i.e., solution pH) and conditioning time on the removal of metal ions from the solutions will be evaluated. The resulting sludges will be used as feeds for precipitate flotation tests.

- *Precipitate Flotation Tests*: Precipitate flotation tests will be carried out in two phases. In the first phase, the tests will be conducted in batch mode using a micro flotation column, in order to assess the effect of different factors on the flotation performance. Findings from the first phase will be used to guide the second phase of the precipitate flotation tests, which will be conducted in continuous mode using a flotation column. A sufficient amount of sludges with a lower water content than the raw sludges will be generated in the second phase, which will be used as feeds for filtration tests.

- *Filtration Tests*: Filtration tests will be performed on the lower water content sludge obtained through precipitate flotation. As discussed in Section D, different types of filters are used in the mining industry, such as vacuum filter, belt filter, and filter press; whereas, given the facilities and equipment available to the team, a benchtop plate and frame filter press will be used in this task. The effect of feed pressure, filtration time, and filter aid on the solids content of filter cakes will be evaluated. Operating conditioning providing the highest solids content will be determined.

- *High-Density Sludge Tests*: A benchtop high-density sludge system consisting of a lime/slurry mixer, a lime reactor, a floc tank, a clarifier, and pumps will be constructed. Performance of the system will be optimized to achieve through parametric studies. The optimum performance and corresponding experimental conditions will be used to compare the proposed circuit and the high-density sludge circuit.

- *Process Circuit Design and Techno-Economic Analysis*: Based on experimental conditions and results of neutralization, precipitate flotation, and filtration tests, a process circuit with a predetermined processing capacity will be designed, and techno-economic analysis will be

performed on each step of the circuit to evaluate its viability. Techno-economic analysis will also be performed on the high-density sludge circuit based on high-density sludge test results. Techno-economic analysis results will be used to compared the proposed circuit and the high-density sludge circuit.

- *Fundamental Studies*: To better understand the mechanisms controlling the performance of precipitate flotation and filtration, fundamental studies will be conducted, which included but not limited to characterizations of precipitate particles, adsorption studies of collectors on precipitate surfaces, as well as formation and stability of aerated flocs. Fundamental study results will be valuable additions to the science of acid mine drainage sludge dewatering and precipitate flotation.

**2.3 Accomplishment Summary**

- **PFD process defined & validated:** Full precipitation–flotation–dewatering (PFD) circuit designed; continuous operation showed stable, high metal-ion removal (>98%) and dense sludge (26.6 wt%).
- **Chemistry optimized:** Compared to NaOH and $Na_2CO_3$, CaO identified as the most effective precipitation condition by ICP-MS, removing most metal ions >98%.
- **Flotation window established:** Optimal set includes pH 10.0, A-100 flocculant 10 mg/L, sodium oleate 400 mg/L, 60 s conditioning; frothers of 100 mg/L MIBC or 0.4 g/L ethanol both effective; reagent doses can be reduced in continuous mode.
- **Speciation–precipitation alignment:** Log C-pH calculations confirm precipitation order ($Fe^{3+} \rightarrow Al^{3+} \rightarrow Zn^{2+} \rightarrow Sn^{2+} \rightarrow Cd^{2+} \rightarrow Co^{2+} \rightarrow Ni^{2+} \rightarrow Mn^{2+} \rightarrow Mg^{2+}$) and thresholds (e.g., $Fe(OH)_3 \geq$ pH 2.1; $Al(OH)_3 \geq 3.8$ but unstable > 11.4; $Co(OH)_2 \geq 7.4$; $Ni(OH)_2 \geq 8.7$; $Zn(OH)_2 \geq 7.7$; $Mn(OH)_2 \geq 9.6$; $Cd(OH)_2 \geq 10.2$; $Mg(OH)_2 \geq 9.4$, $Sn(OH)_2 \geq 3.5$); Tin was determined as $Sn^{2+}$ instead of $Sn^{4+}$. The precipitation sequence of metal ions in experimental results largely consists with the theoretical sequence.
- **Process intensification:** Shortening the flotation column improves PFD flotation efficiency. The continuous flotation showed significant long-term stability and reliability, with high removal efficiencies of metal ions.
- **Mechanistic insights:** Flocculant and collector chemically adsorb on precipitate surfaces. The total interaction energies between precipitate particles during flotation were calculated

according to DLVO theoretical, indicating stirring is necessary to overcome the energy barrier.

- **Techno-economic advantage:** PFD demonstrates favorable cost-effectiveness and denser sludge compared with HDS, sulfate-reduction bioprocesses, and other chemical treatments.

## 3. PROJECT ACTIVITIES

### TASK 1.0 – SAMPLE COLLECTION AND CHARACTERIZATION

The acid mine drainage was collected from a coal preparation plant that treats run-of-mine bituminous coal of the West Kentucky No. 13 (Baker) seam located in western Kentucky, USA. The collected AMD was stored in five 55-gallon tanks, as shown in Fig.1.

**Fig. 1.** Acid mine drainage collected from a mining company.

The pH value of the acid mine drainage was measured by a pH meter (AP110, Thermo Fisher Scientific, USA). The elemental composition of the original sample was tested using inductively coupled plasma mass spectrometry (ICP-MS, Thermo Electron X-Series, Thermo Fisher Scientific, USA). The elemental concentration and pH of the AMD were shown in Table. 1.

**Table. 1.** Elemental concentration (mg/L) and pH of the AMD.

| Element | Concentration (mg/L) |
|---|---|
| Mn | 8.11 |
| Co | 0.36 |
| Ni | 1.53 |
| Zn | 8.86 |
| Fe | 192.77 |
| Al | 104.48 |
| Ca | 317.23 |
| Mg | 99.69 |
| Na | 694.05 |
| Si | 8.52 |
| Cd | 0.28 |
| Sn | 0.27 |
| pH | 2.45 |

As shown in Table. 1, the initial pH value of the AMD is 2.45. The concentrations of inevitable ions in AMD, including sodium, calcium, and magnesium, are 694.05, 317.23, and 99.69 mg/L, respectively. The main metal ions affecting the emissions are aluminum and iron, with concentrations of 192.77 and 317.23 mg/L, respectively. Other trace metal ions, such as zinc, nickel, cadmium, tin, cobalt, and so on, have concentrations below 10 mg/L. In addition to metal ions with concentrations below 1 mg/L, the precipitation behavior of other ions will be characterized and analyzed.

## TASK 2.0 – PRECIPITATION TESTS

The precipitation tests were performed on the AMD to investigate the precipitation characteristics of the contaminant elements. A volume of 70 mL of AMD was measured using a cylinder for each test. Then, the solution was subjected to a pH range of 3.0 to 12.5 by adding neutralizing agent of $Na_2CO_3$, NaOH, and CaO, respectively. After the addition of neutralizing agents, the AMD was stirred at 800 r/min for 5 min to ensure complete dispersion of the base. After reaching the target pH, the suspension was separated into precipitate and filtrate by atmospheric filtration. The filtrate was diluted using 5 wt.% $HNO_3$ for ICP-MS analysis. The precipitates were dried in an oven at 60 °C for 12 h, and then weighed to calculate the recovery of containment elements. The overall procedure of precipitation test is depicted in

**Fig. 2**.

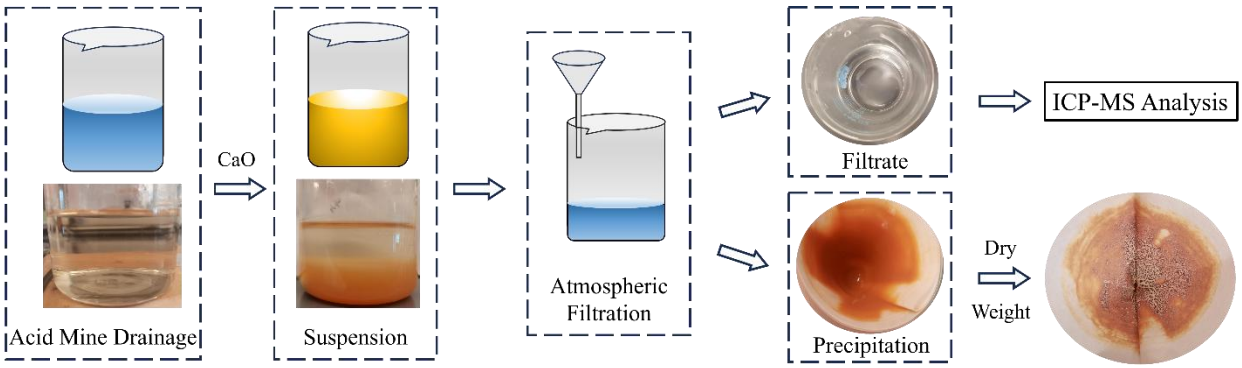


**Fig. 2.** The experimental procedure of precipitation test.

The function of pH value on the weight of the precipitation was initially investigated by altering the pH values using different dosages of neutralizing agents. The results of using CaO as a neutralizing agent are shown in Fig. 3. The weight of the precipitates generally increases with the increasing pH value. The maximum weight of precipitation is observed at a pH of 11.50, and

there is also a peak at a pH of 6.50. Further research and analysis, along with ICP-MS results, are required to explain the reasons behind the appearance of this peak. The images of the suspension before and after filtration at different pH values when CaO is used as a neutralizing agent are shown in Fig. 4. There is almost no precipitate form at a pH as low as 3.00, and the filtrate is in light yellow, which indicates high concentration of metal ions in filtrate. However, when the pH exceeds 5.50, a noticeable formation of precipitates is observed, resulting in a clear filtrate. As the pH of the AMD increases from 5.50 to 9.50, the weight of precipitates also significantly increases.

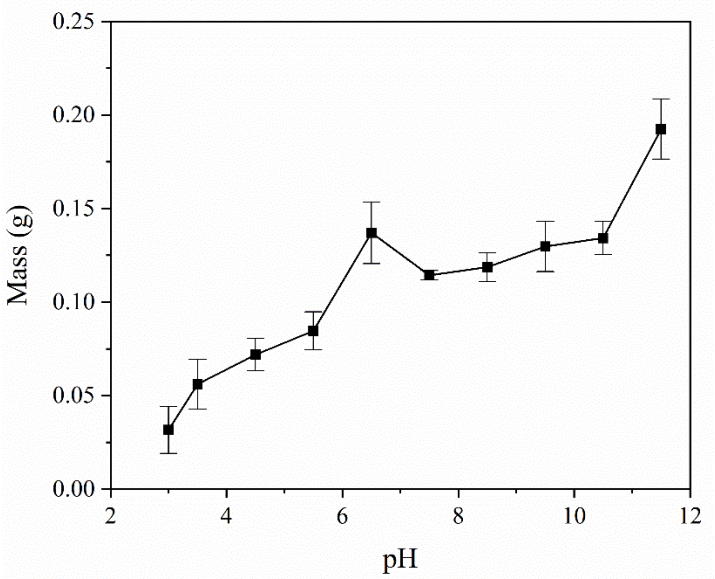


**Fig. 3.** The effect of CaO dosages on precipitation weight.

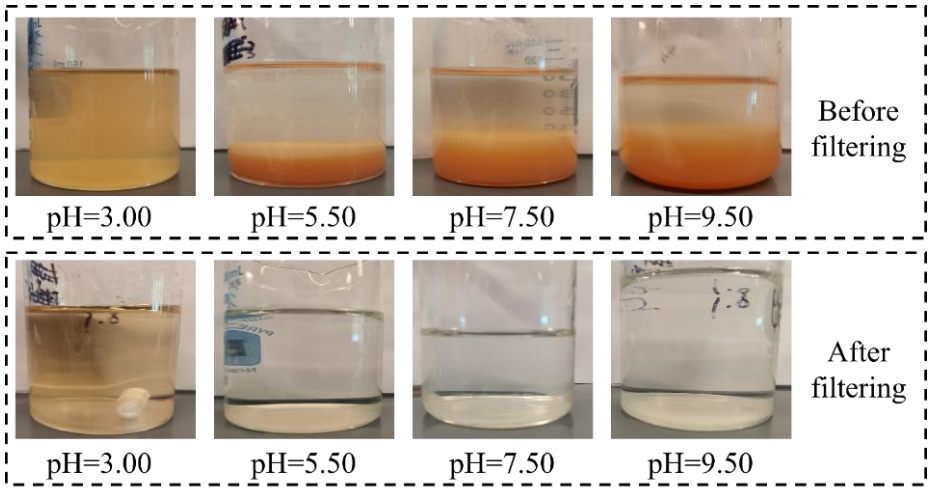

**Fig. 4.** Images of suspension at different pH values adjusted by CaO before and after filtering.

The precipitation weight of different solution pH subjected by NaOH is shown in Fig. 5. It can be observed that there is an increasing trend in precipitation weight from pH 3.00 to pH 12.50, with the highest precipitation weight at pH 12.50, which is 0.204 g. A decrease in precipitation weight is observed at pH 6.5, which requires further explanation through ICP-MS results and additional fundamental research. The images of suspension at different pH before and after filtering are shown in Fig. 6. At pH 3.0, there is almost no difference between the two images, indicating low precipitation in the AMD system. After reaching a pH of 5.50, the filtrate becomes clear, and the increase in precipitation weight is evident, as observed by the volume of the orange part.

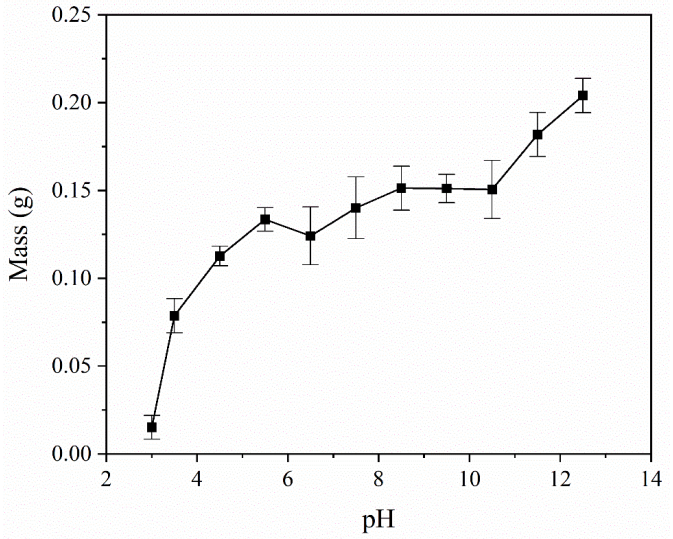

**Fig. 5.** The effect of NaOH dosage on precipitation weight.

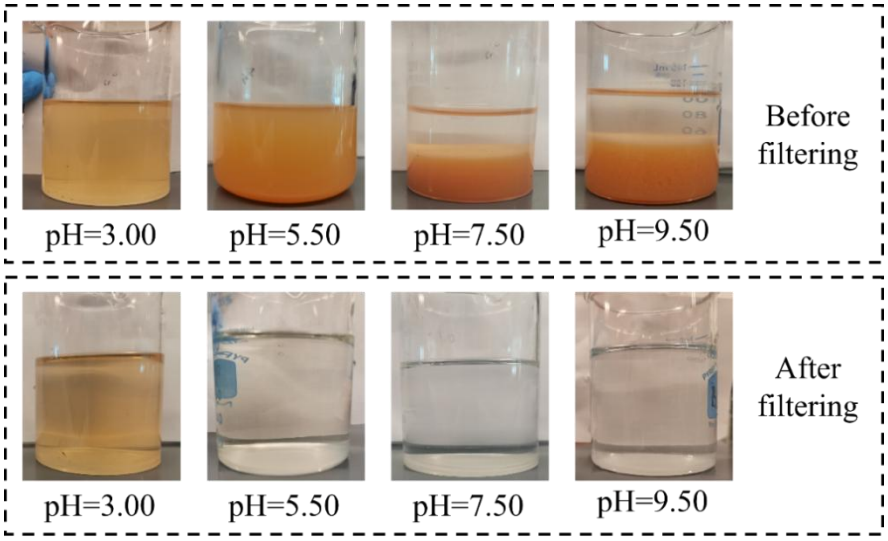


**Fig. 6.** Images of suspension at different pH values adjusted by NaOH before and after filtering.

Fig. *7* and Fig**.** ***8*** depict the effect of $Na_2CO_3$ dosage on precipitation weight and the experimental images of suspension at a pH range of 3.00 ~ 9.50. As shown in Fig. 7, a slow increasing rate of precipitation weight can be seen from pH 3.00 to 6.50, while the precipitation weight quickly increases after reaching pH of 8.50. The highest weight of precipitation appears at pH of 11.50. The exact weight of the heaviest solid is about 0.45 g, which is heavier than both CaO and NaOH. The exact mass of the heaviest solids was around 0.45 g, which is heavier compared to that of CaO and NaOH. This could be due to the binding of metal ions with carbonates. Fig. ***8*** shows that only a small amount of precipitation forms at a pH of 3.0, with solid mass as low as 0.019 g (Fig. 7). As the pH value increases, the filtrate gradually becomes clear.

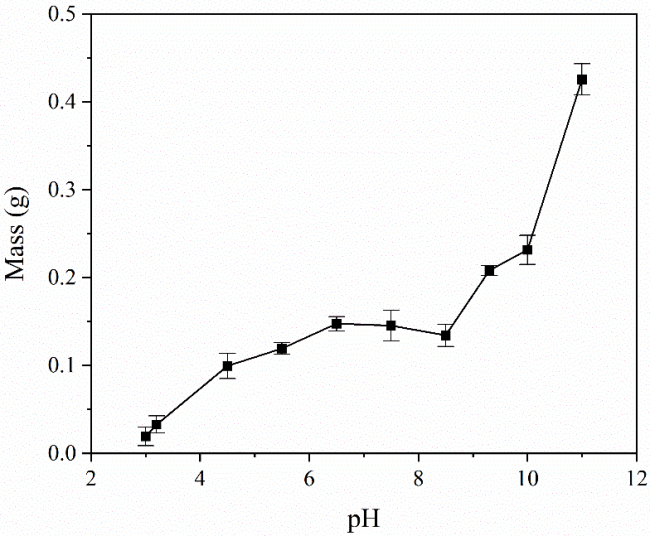


**Fig. 7.** The effect of $Na_2CO_3$ dosage on precipitation weight.

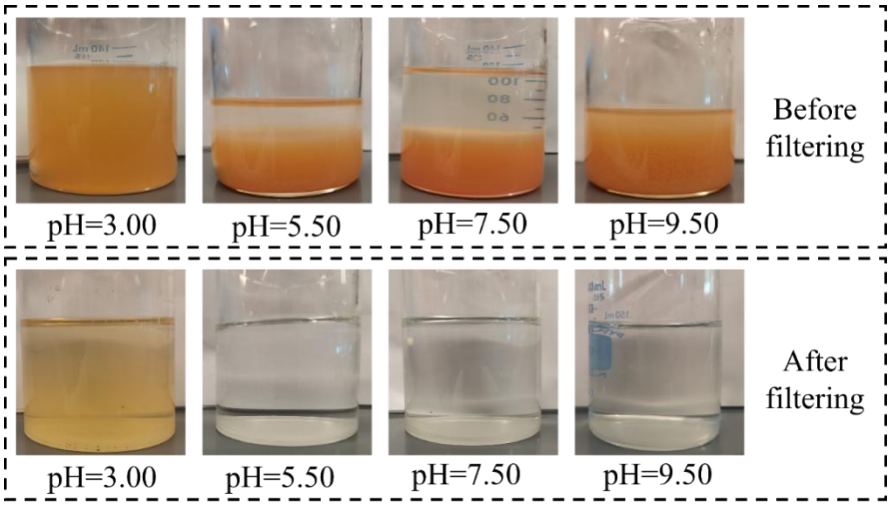


**Fig. 8.** Images of suspension at different pH values adjusted by $Ca_2CO_3$ before and after filtering.

Therefore, CaO was selected as the neutralizing agent in this study considering the precipitation effect and economic benefit. The filtrate samples using CaO as neutralizing agent were prepared and diluted 100 times with 5% $HNO_3$ solution for ICP-MS analysis. The results were shown in Figures 9-17. The recovery of metal ions was calculated as:

$$Recovery\ (\%) = \frac{c_{Me}}{c_{Me0}} \times 100 \quad (1)$$

where $c_{Me}$ and $c_{Me0}$ are the concentration of the same metal ion in filtrate and original acid mine drainage, respectively. Me represents $Fe^{3+}$, $Al^{3+}$, $Zn^{2+}$, $Sn^{2+}$, $Cd^{2+}$, $Co^{2+}$, $Ni^{2+}$, $Mn^{2+}$, and $Mg^{2+}$. The ion recovery of reflects the removal of metal ions in acid mine drainage.

The recovery of $Al^{3+}$ in AMD at different pH values is shown in Fig. 9. At pH=3.5, $Al^{3+}$ initiated the formation of $Al(OH)_3$ and achieved its peak recovery of 98.8% at pH=5.5. Although the recovery of $Al^{3+}$ experienced a slight decline with the increasing pH ranging 5.5-11.5, it still attained a recovery of 89% at pH=10.0. The decrease in the $Al^{3+}$ curve was attributed to the hydroxylation reaction of $Al(OH)_3$ as:

$$Al(OH)_3 + OH^- \rightleftharpoons Al(OH)_4^- \quad (2)$$

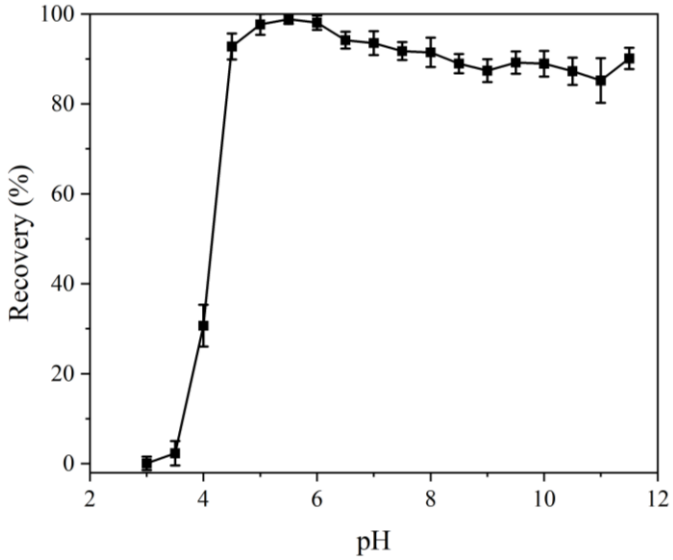


**Fig. 9.** The recovery of $Al^{3+}$ in AMD at different pH values adjusted by CaO.

Fig. **10** shows the results of $Fe^{3+}$ recovery at various pH values in AMD. Ferric initiated precipitation at a pH as low as 3.0 and achieved nearly complete precipitation at a pH of 4.0. Throughout this process, as the pH increased from 3.0 to 3.5, the recovery of $Fe^{3+}$ surged from 5.3% to 72.8%, showcasing a noteworthy improvement of 67.5%. As the pH ascends to 4.0, the recovery of $Fe^{3+}$ further elevated to 96.9%, reflecting a 24.1% enhancement. Therefore, the principal precipitation behavior of $Fe^{3+}$ occurred between pH 3.0 and 3.5. With the ongoing increase in aqueous pH, the ferric recovery remained relatively constant, stabilizing at approximately 98% until the end of the experiment.

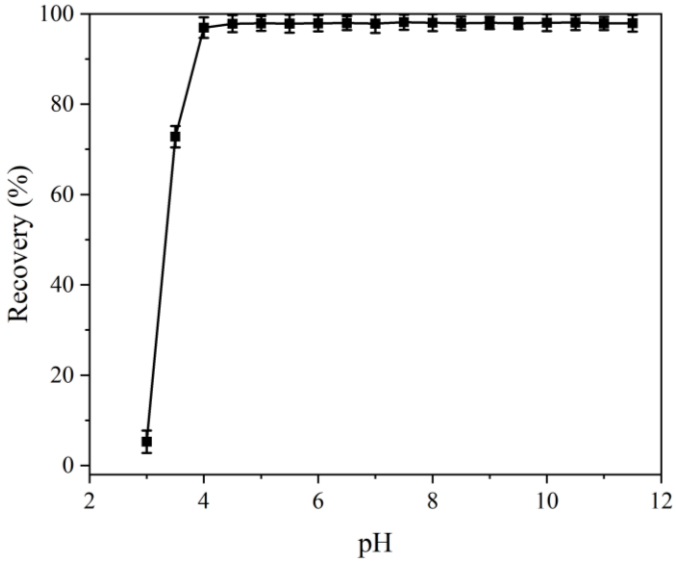


**Fig. 10.** The recovery of $Fe^{3+}$ in AMD at different pH values adjusted by CaO.

The trend of $Zn^{2+}$ recovery with different solution pH values is shown in Fig. 11. Initially, a small amount of $Zn(OH)_2$ precipitation began to form at a pH of 3.5, followed by a significant amount of precipitation occurring between pH 5.0 and 5.5, i.e. the binding of $Zn^{2+}$ with $OH^-$, forming $Zn(OH)_2$. During this period, the $Zn^{2+}$ recovery increased from 25.50% to 86.48%, then reached 97.08% at pH=6.0. As the solution pH increased from 6.0 to 11.5, the $Zn^{2+}$ recovery remained relatively constant, stabilizing at around 97%.

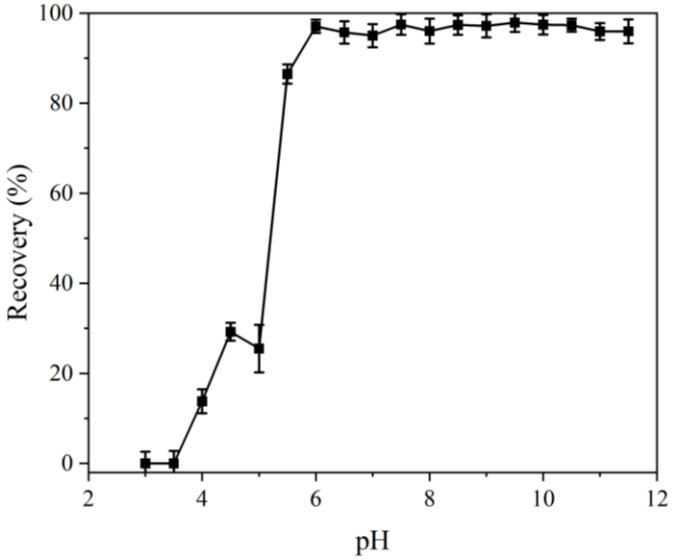


**Fig. 11.** The recovery of $Zn^{2+}$ in AMD at different pH values adjusted by CaO.

The ICP-MS results of the variation in $Sn^{2+}$ recovery as a function of solution pH are shown in Fig. 12. It can be observed that at pH=3.0, some Sn ions have already transferred to $Sn(OH)_2$,

but the proportion was minimal, with a recovery of only 8.81%. As the pH increased, the recovery of $Sn^{2+}$ steadily increased. Then at pH=6.0, $Sn^{2+}$ was essentially completely precipitated, with a recovery of 93.77%. The main precipitation behavior occurs at pH of 5.0 to 6.0 within the studied pH range. Although the $Sn^{2+}$ recovery slightly decreased to 84.64% at a pH of 8.5, it continued to increase with the increasing solution pH, ultimately stabilizing at around 97%. The decrease observed at pH=8.5 was attributed to the partially hydroxylation reaction of $Sn(OH)_2$.

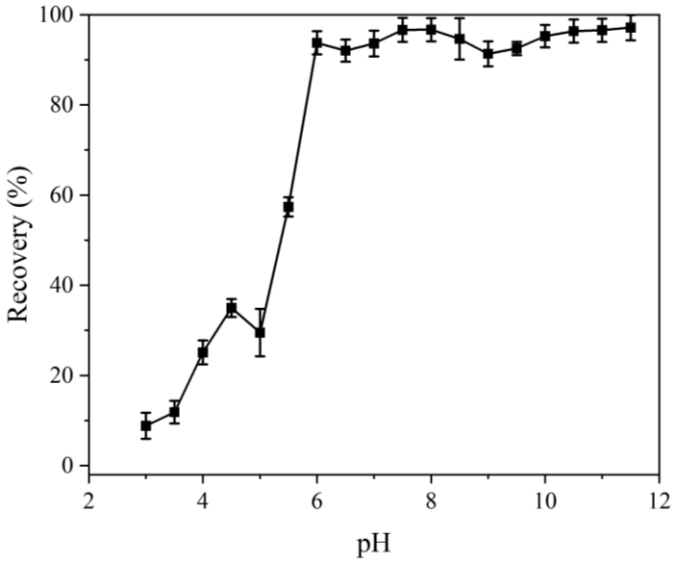


**Fig. 12.** The recovery of $Sn^{2+}$ in AMD at different pH values adjusted by CaO.

The $Cd^{2+}$ recovery at different solution pH values is shown in Fig. 13. The significant binding of $Cd^{2+}$ with hydroxide occurred between pH of 5.0 and 6.0, forming $Cd(OH)_2$. The $Cd^{2+}$ recovery rapidly increased from 17.02% to 95.95% within this pH range. Subsequently, it gradually rose to 98.18% in the pH range of 6.0 to 8.0 and finally achieved its highest recovery of 99.54% at pH of 10.0.

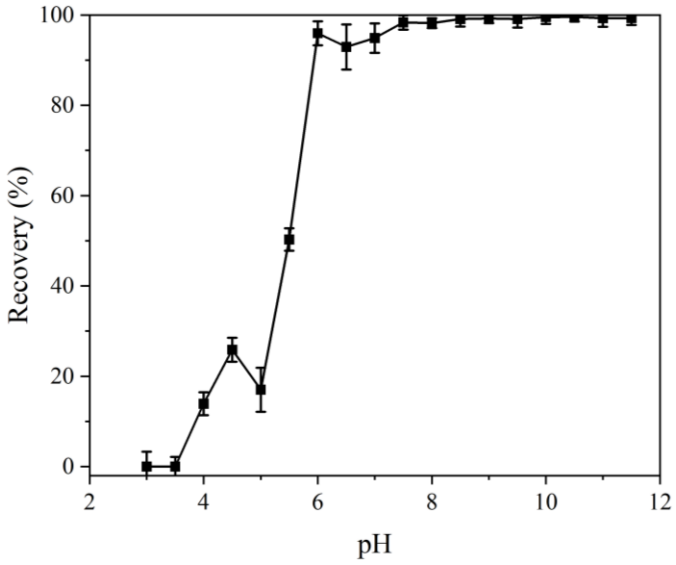


**Fig. 13.** The recovery of $Cd^{2+}$ in AMD at different pH values adjusted by CaO.

Figure Fig**. 14** shows the ICP-MS results of $Co^{2+}$ recovery at various pH values in AMD. The curve for $Co^{2+}$ exhibits a similar trend to that of $Cd^{2+}$. The precipitation behavior of cobalt ions initially started at a pH of 3.5, but mainly occurred between pH=5.0 and pH=6.0 with a recovery change from 16.86% to 93.20%. The recovery finally remained at approximately 99% after a small decrease at pH of 6.5.

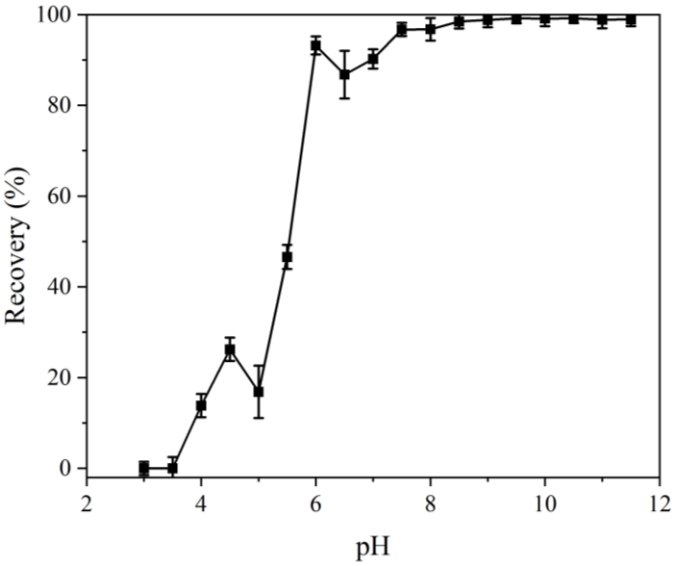


**Fig. 14.** The recovery of $Co^{2+}$ in AMD at different pH values adjusted by CaO.

Figure Fig**. 15** presents the ICP-MS results depicting the recovery of $Ni^{2+}$ at different pH values in Acid Mine Drainage. A modest amount of $Ni(OH)_2$ precipitation initiated at a pH of 3.5, followed by a substantial increase in precipitation between pH 5.0 and 5.5 with the recovery

changing from 17.06% to 90.22%. As the solution pH ascended from 6.0 to 11.5, the $Ni^{2+}$ recovery maintained a relatively constant level at around 97%, peaking at 98.08% at pH=10.0.

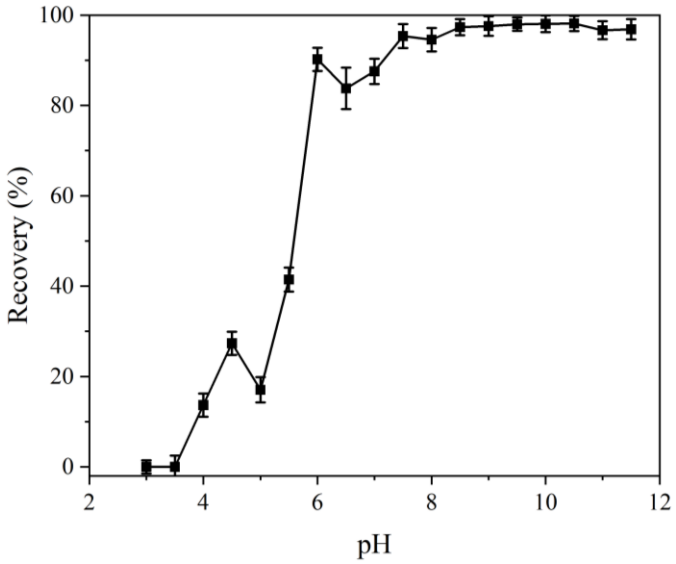


**Fig. 15.** The recovery of $Ni^{2+}$ in AMD at different pH values adjusted by CaO.

The recovery of $Mn^{2+}$ in AMD at different pH values is shown in Fig. 16. Compared with $Ni^{2+}$, the precipitation pattern of $Mn^{2+}$ exhibited a subtle variation: the majority precipitated between pH=5.0-6.0, and subsequently, as the pH rose from 6.0 to 10.0, the recovery of $Mn^{2+}$ gradually ascends from 72.8% to 98.9%.

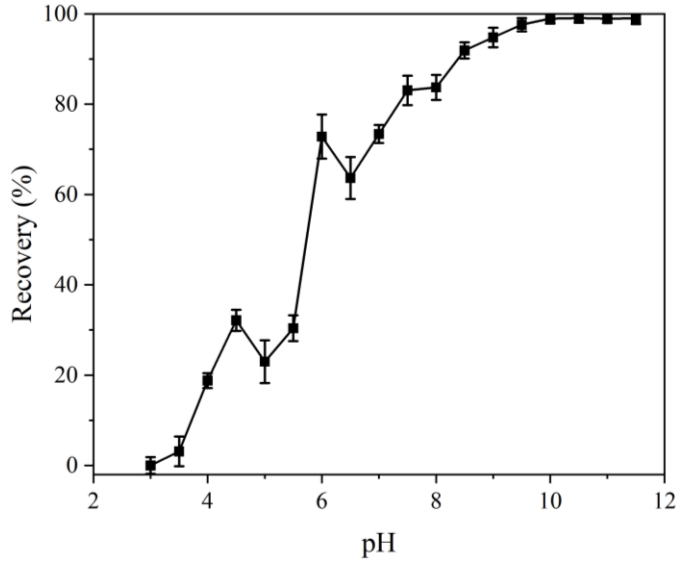


**Fig. 16.** The recovery of $Mn^{2+}$ in AMD at different pH values adjusted by CaO.

The ICP results depicting the variation in $Mg^{2+}$ recovery with different solution pH are shown in Fig. 17. When the solution pH was below 3.5, $Mg^{2+}$ didn't form precipitation. Then as the pH

increased from 4.0 to 9.0, the $Mg^{2+}$ recovery fluctuated between 10% and 30%. $Mg^{2+}$ began to rapidly precipitate to form $Mg(OH)_2$ when the pH reached approximately 9.0, and completed precipitation process at around pH of 10.5, with a recovery of 96.58%. As the pH value increases above 10.0, the recovery of metal ions generally remains stable.

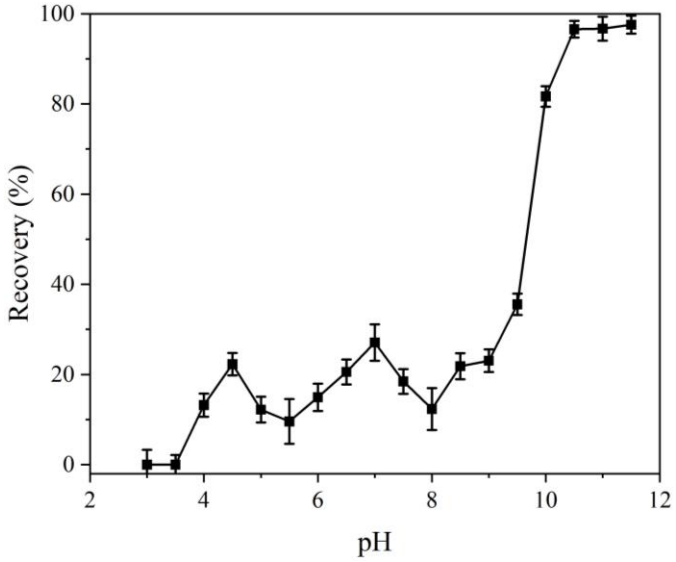


**Fig. 17.** The recovery of $Mg^{2+}$ in AMD at different pH values adjusted by CaO.

According to the ICP-MS results, Table. 2**Table. 2.** The recovery of the various metal ions at pH of 5.5 and 10.0. lists the recovery of various metal ions at pH 5.5 and 10.0. As can be seen from Table. 2, there were significant differences in the recovery of various metal ions at pH 5.5. Based on the relative recovery at this pH, the sequence in which metal ions form precipitates as the solution pH increases from 3.0 to 11.5 can be determined. It is worth noting that, although the recovery of Fe ions is slightly lower than that of aluminum ions at pH 5.5, Fe ions were essentially completely precipitated at pH 4.0, while Al ions only completely precipitated at pH 5.0, thus the precipitation pH of $Fe^{3+}$ is lower than that of $Al^{3+}$. Therefore, the order of precipitation pH of metal ions in AMD, from low to high, is as follows: $Fe^{3+}$, $Al^{3+}$, $Zn^{2+}$, $Sn^{2+}$, $Cd^{2+}$, $Co^{2+}$, $Ni^{2+}$, $Mn^{2+}$, and $Mg^{2+}$.

The recovery of all metal ions except $Al^{3+}$ and $Mg^{2+}$ was greater than 95% at pH=10.0, with the highest reaching 98.9%, according to Table. 2. The recovery of $Al^{3+}$ $^{+}$ and $Mg^{2+}$ can also reach 89% and 81.68%, respectively. Raising the pH above 10.0 will consume more neutralizing agents, which is not conducive to cost savings. Therefore, a pH of 10.0 was selected as the most effective pH value in this study.

**Table. 2.** The recovery of the various metal ions at pH of 5.5 and 10.0.

| Metal ions | Recovery / % | |
|---|---|---|
| | pH=5.5 | pH=10.0 |
| Al | 98.81 | 88.94 |
| Fe | 97.84 | 98.03 |
| Zn | 86.47 | 97.42 |
| Sn | 57.38 | 95.23 |
| Cd | 50.27 | 99.54 |
| Co | 46.57 | 99.13 |
| Ni | 41.46 | 98.08 |
| Mn | 30.39 | 98.93 |
| Mg | 9.58 | 81.68 |

Consequently, CaO was selected as the neutralizing agent in this study, and a pH of 10.0 was determined as the most effective pH value, achieving the removal of most metal ions of >95%.

## TASK 3.0 – PRECIPITATE FLOTATION TEST

Subtask 3.1 – Batch Flotation Tests

The precipitation flotation test was carried out utilizing Patridge-Smith micro-flotation cells, as shown in Fig. 18. After trans fer slurry into flotation cell, air was pumped into the cell during the flotation, and the flotation water addition was recorded. The slurry was then divided into suspension and post-floated solution. To dissolve the remaining solids in the post-floated solution, it was adjusted to a pH of 2.00 using $HNO_3$, then a small volume of the solution was diluted and analyzed using ICP-MS to calculate the removal of contained ions. The flotation removal of metal ions was calculated using the formula:

$$Flotation\ removal\ (\%) = \frac{c_1}{c_0} \times 100 \quad (3)$$

where $c_1$ and $c_0$ are the concentration of the same metal ion in post-floated solution and original AMD.

**Fig. 18.** The Patridge-Smith micro-flotation cell used in the flotation experiments.

In this section, the effect of flotation pH, collector dosage, frother type and dosage, and conditioning time on the flotation recovery of both precipitates and water was evaluated.

*I. Flotation pH*

To investigate the pH on flotation efficiencies of elements, the experiments were conducted at a pH range from 8.0 to 10.0, with an addition of 10 mg/L A-100 flocculant and 300 mg/L NaOL as collector. The flotation recoveries of metal ions were depicted in Fig. 19. As can be seen, recoveries of all metal ions increased with the increasing pH value. However, at lower pH of 8.0-9.5, the recovery of Mg is much lower than that of other ions. Moreover, the recovery of Sn showed a sharp increase when the pH reached 9.0. Therefore, to maximize the recoveries of metal ions, especially Mg, a pH of 10.0 was selected as the flotation pH for sequential experiments, which is consistent with the result of precipitation tests.

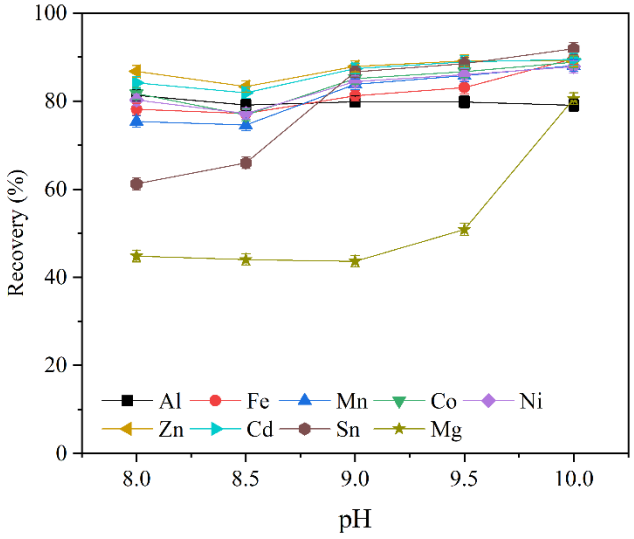


**Fig. 19.** Flotation recoveries of metal ions at varying flotation pH values.

*II. Flocculants type and dosage*

The effect of different types of flocculants on flotation recovery was investigated, as depicted in Fig. 20. Flocculants of A-100, N-100, N-300, and N-300 LMW from Kemira were selected as flocculants. The primary constituents of the flocculants consist of polyacrylamide (PAM), as indicated in the safety data sheets provided by Kemira. Among these, N-100, N-300, and N-300 LMW variants are classified as non-ionic, while A-100 is characterized as anionic. Fig. **20**(a) illustrates the effect of flocculant type on recovery of elements after flotation. The concentration of the flocculants in the solution was all 10 mg/L. It can be observed that the sample added A-100 as flocculant has the best flotation effect, followed by N-300 LMW, N-300, and N-100 in sequence. In the A-100 sample, the recoveries of various metal ions were all greater than 85%, of which $Al^{3+}$

and $Fe^{3+}$ have recovery of 88.12% and 95.68%, respectively. The $Mn^{2+}$ exhibits the highest recovery rate of 97.80%. Additionally, no matter which flocculant is used, the recovery of ions of Fe, Mn, Co, and Cd is higher than that of Al, Sn and Mg ions. Therefore, A-100 flocculant was selected as the flocculant in sequential experiments.

The effect of concentration of A-100 on ion recoveries was also investigated, and the results were shown in Fig. **20**(b). With the increase in the dosage of A-100, the recoveries of various elements in AMD exhibits a trend of initially rising and then decreasing, reaching a peak recovery of >85% when the A-100 concentration is 10 mg/L. Thus, the dosage of A-100 flocculant was determined as 10 mg/L.

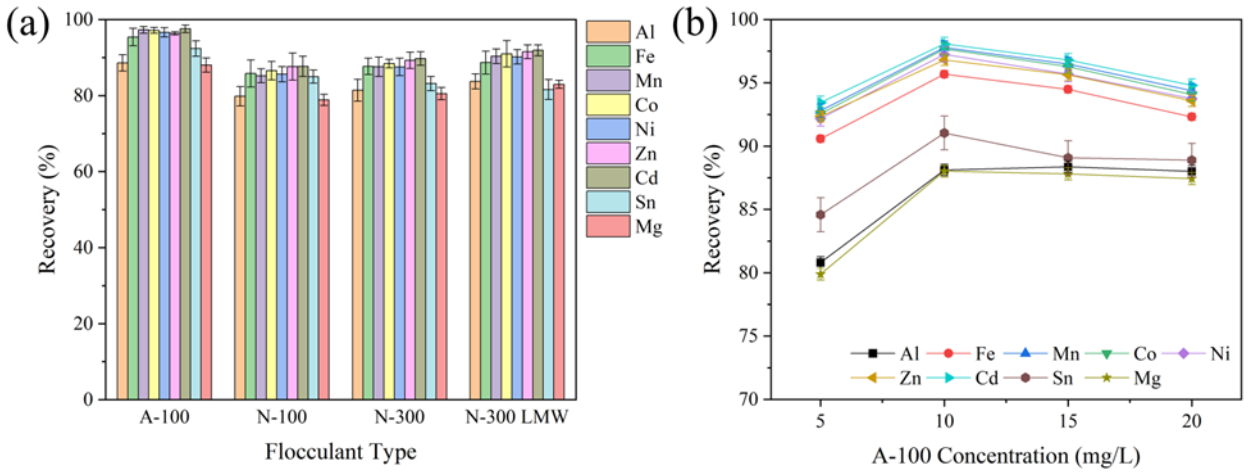


**Fig. 20.** Flotation recoveries of metal ions with (a) different types of flocculants and (b) different concentration of A-100 flocculant.

*III. Collector dosage*

Sodium oleate (NaOL) was used as the collector in this study, and the effect of NaOL dosage ranging from 100-500 mg/L on flotation recovery of metal ions was investigated. ICP-MS results shown in Fig. 21 indicated that as the concentration of sodium oleate increased from 100 mg/L to 400 mg/L, the recovery of various elements consistently increased, reaching their peak (>90%) at NaOL concentration of 400 mg/L. Specifically, the recovery of $Al^{3+}$ and $Fe^{3+}$ increased from 66.41% and 68.28% to 93.56% and 93.42%, respectively. However, excessively high concentrations of sodium oleate led to a decline in ion flotation recovery, possibly due to multilayer adsorption on the surface of precipitate particles or the formation of NaOL micelles. Simultaneously, the concentration of sodium oleate could influence the flotation effect by affecting the flotation foam

properties during the flotation process. As the concentration increases, the oleate ion accumulates on the liquid film surface, forming a dense surface membrane that impedes the drainage of adjacent liquid films, thereby enhancing the foam stability. However, when the concentration of sodium oleate was too high, the content of oleate ions in the foam increased, reducing the liquid content and, paradoxically, weakening stability. Therefore, 400 mg/L was selected as the optimal concentration of sodium oleate in the experiments.

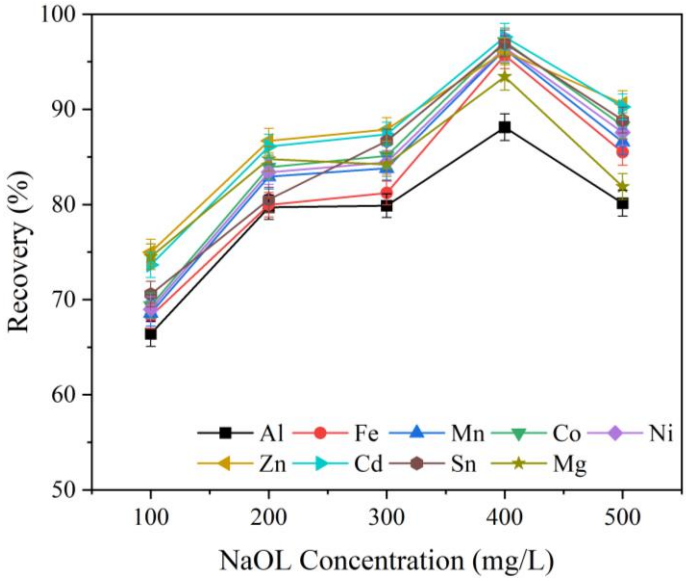


**Fig. 21.** The flotation recoveries of metal ions with different NaOL dosages.

*IV. Conditioning time*

The effect of conditioning time after adding sodium oleate on the ion recovery of the flotation process was investigated, as shown in Fig. 22. The stirring speed was maintained at 700 rpm, and the stirring durations were set at 0, 10, 60, 300, and 600 seconds. As the conditioning time increased, the recovery of metal ions exhibited a significant rise within the initial 60 seconds, escalating from ~87% to ~96%. This phenomenon can be attributed to the adsorption of oleate ions on the surface of flocculated precipitate particles induced by stirring. With prolonged stirring time, the adsorption effect became more pronounced, thereby enhancing the flotation efficiency. However, when the stirring time extended to 300 seconds and 600 seconds, the recovery declined. The observed outcome is attributed to the excessive stirring time causing partial desorption of oleate ions under the influence of shear forces. This led to a reduction in the hydrophobic effect on particles, diminishing the flotation efficiency and consequently lowering the ion recovery. Therefore, the optimal conditioning time of NaOL was determined as 60 seconds.

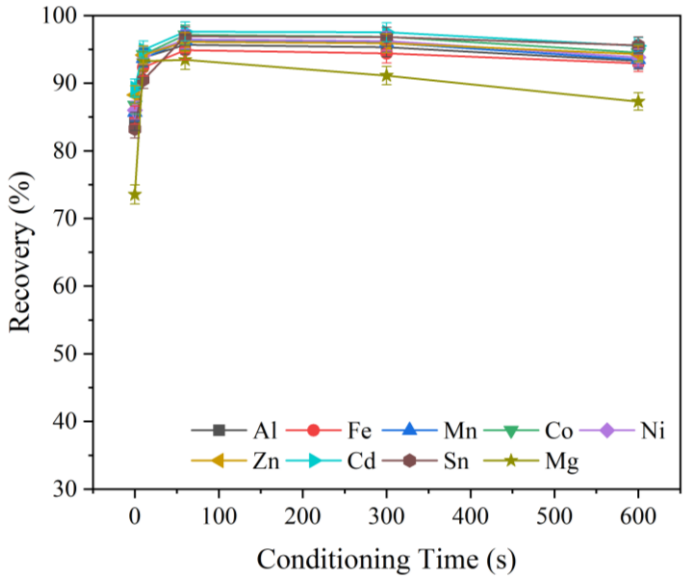


**Fig. 22.** The flotation recoveries of metal ions with different conditioning time.

i. *Frother types and dosages*

The effect of different types of frothers on flotation recovery was investigated, as depicted in Fig. 23. Frothers of methyl isobutyl carbinol (MIBC) and ethanol were selected, which is commonly used in industrial. According to Fig. 2 (a), the recovery percentages for all metals remain relatively high, generally above 80%, across the range of MIBC concentrations (30 to 300 mg/L). The recovery of $Al^{3+}$ showed an increasing trend from around 75% at 30 mg/L MIBC to approximately 90% at 100 mg/L MIBC, while the recovery of $Fe^{3+}$ reached its peak recovery of 90-95% at 100 mg/L MIBC. Metal ions of Mn, Co, Ni, Zn, Cd, Sn, Mg exhibited minimal fluctuations with a high flotation recovery, all staying within the 85-95% range. Therefore, a concentration of 100 mg/L MIBC appeared to maintain high recovery rates across all metals, with Al showing improved recovery around this concentration. The flotation efficiency as a function of ethanol concentration was similar to MIBC. The recovery percentages for all metals remained high, predominantly above 80%, across the range of ethanol concentrations (0.2 to 1.0 g/L). $Al^{3+}$ shows a slight decreasing trend after ethanol concentration of 0.4 g/L, while $Mg^{2+}$, $Fe^{3+}$, and $Zn^{2+}$ exhibited the highest and most stable recovery efficiencies, generally above 95%. To maximize the flotation recovery of metal ions, a concentration of 0.4 g/L ethanol was determined.

It is found similar flotation efficiencies when comparing MIBC and ethanol at their optimal concentrations. Therefore, both MIBC and ethanol are acceptable for efficient flotation.

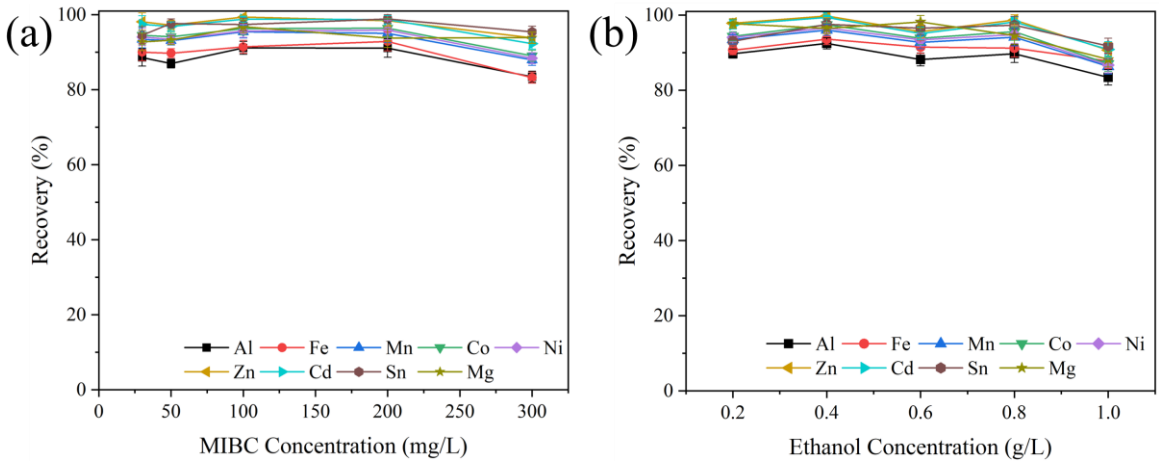


**Fig. 23.** Flotation removal of metal ions with different concentrations of (a) MIBC and (b) ethanol.

ii. *Air flowrates*

The effect of air flow rate from 0.1 to 0.6 L/min after conditioning was investigated, as depicted in Fig. 24. A significant decrease in the flotation removal of metal ions, from approximately 95% to 60%, was observed as the air flow rate increased from 0.1 L/min to 0.6 L/min. This can be explained by the fact that smaller air bubble sizes can accelerate the formation of aerated flocs, which are light and easy to float, while lower air flowrates reduce turbulence of the slurry and thereby keep the aerated flocs stable.

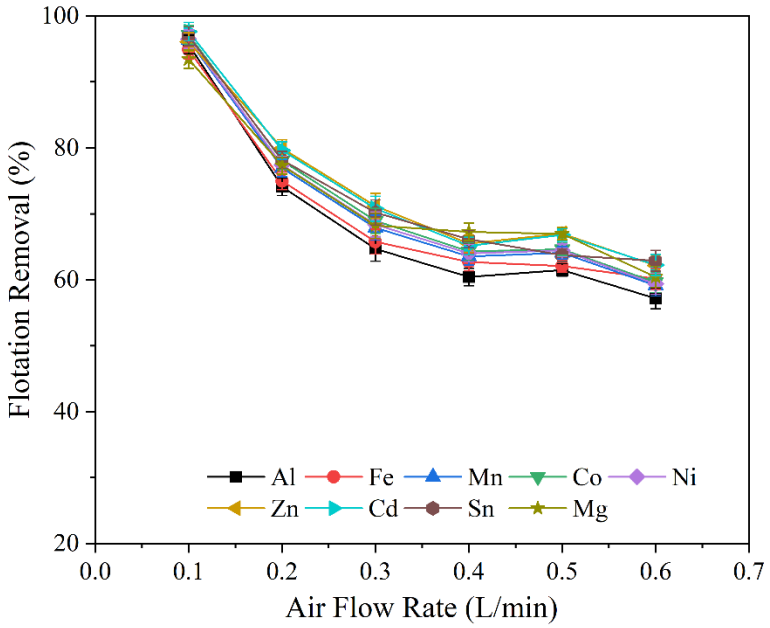

**Fig. 24.** Flotation removal of metal ions using varying air flow rate after conditioning.

Subtask 3.2 – Continuous Flotation Tests

Continuous flotation tests were conducted to evaluate the long-term stability and reliability of the PFD process. The optimum conditions determined in Subtask 3.1 were employed. MIBC was used as frother in continuous flotation tests. Reagent dosages were adjusted based on real-time conditions during the continuous tests. The flowchart and real-world equipment of the continuous flotation tests are illustrated in Fig. 25 (a) and (b), respectively. Additionally, due to the reuse of residual A-100, NaOL and frothers in the returned solution, their dosage was reduced to 10 mg/L, 100 mg/L and 30 mg/L MIBC, respectively.

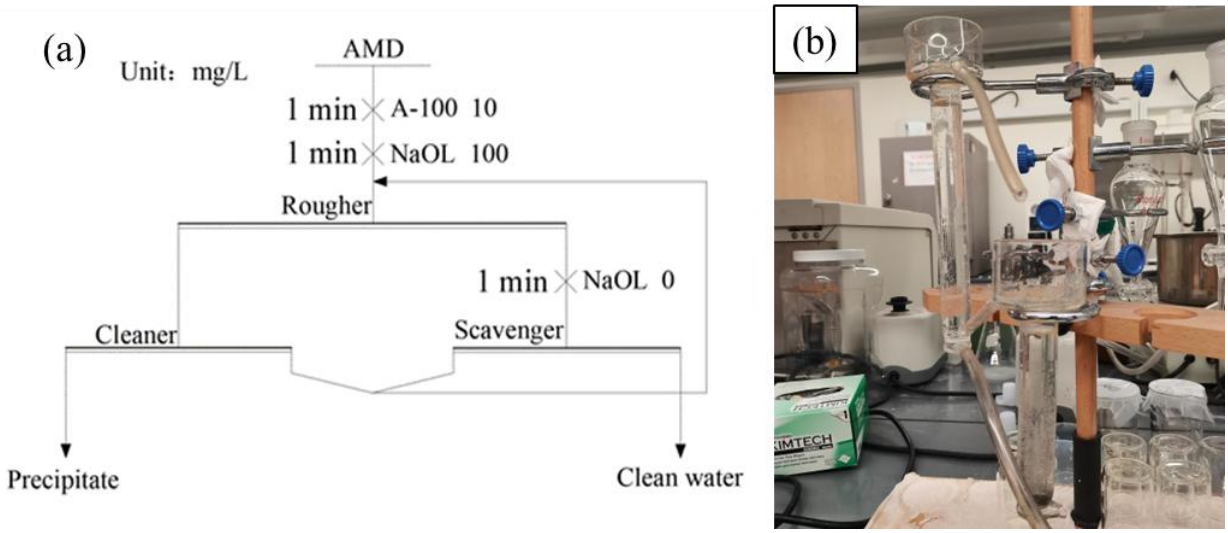


**Fig. 25.** The (a) flowchart and (b) real-world equipment for continuous flotation tests.

Detailed ICP-MS analysis was conducted, as shown in Figures 26-34, illustrating the removal efficiencies of various metals, including Al, Fe, Mn, Co, Ni, Zn, Cd, Sn, and Mg, over multiple cycles. As shown in Fig. 26, the removal efficiency of aluminum remains consistently high, close to 100%, across all 10 cycles. This stability suggests that the system is highly effective in consistently removing aluminum, with minimal variation across the cycles. Al removal from wastewater is crucial to minimize environmental impacts. The near-complete removal rate indicates that the system is well-suited for long-term, continuous operation without significant efficiency losses.

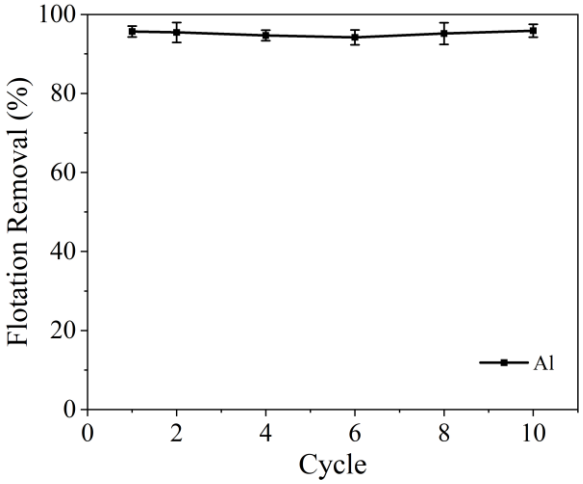


**Fig. 26.** Variation of Al concentration at different cycles of continuous flotation tests.

Iron removal remains effective, ranging from 85% to 95% over the cycles (Fig. 27). However, there is a slight decrease in removal efficiency over time, indicating that the system may experience some reduction in performance as it operates across multiple cycles. The slight downward trend in efficiency may require periodic maintenance or optimization to maintain optimal removal levels over extended use.

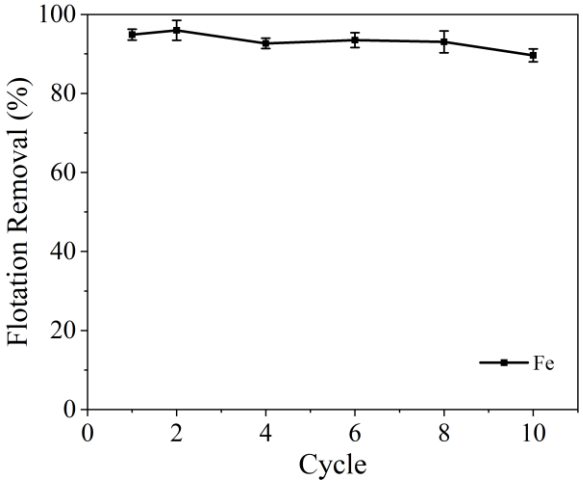


**Fig. 27.** Variation of Fe concentration at different cycles of continuous flotation tests.

Manganese removal remains highly effective, with removal percentages consistently between 90% and 95% across the cycles, as shown in Fig. 28. The system demonstrates stable performance, with minor fluctuations in removal efficiency. The consistent removal rates suggest that the system is robust and reliable, capable of maintaining high removal efficiency over long periods of operation.

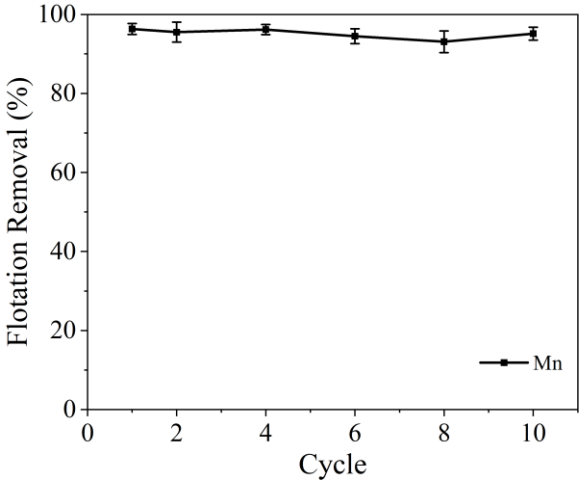


**Fig. 28.** Variation of Mn concentration at different cycles of continuous flotation tests.

Cobalt removal remains close to 100% throughout all 10 cycles, indicating excellent system performance (Fig. 29). Cobalt removal is critical for reducing environmental contamination. The minimal fluctuations in removal efficiency across the cycles indicate that the system is highly stable and effective in removing cobalt, with no significant loss in performance over time. The high removal rates make this system suitable for continuous operation.

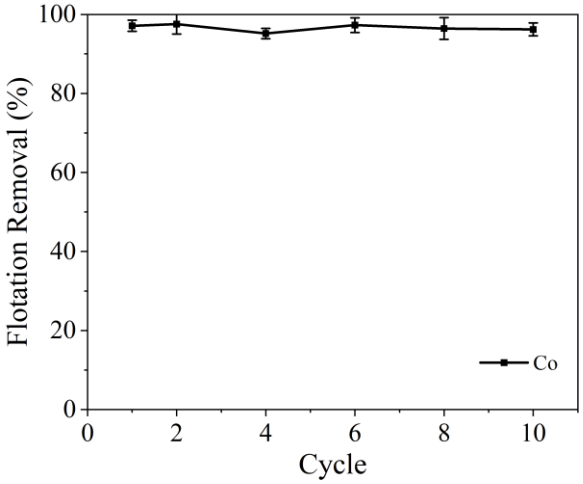


**Fig. 29.** Variation of Co concentration at different cycles of continuous flotation tests.

Nickel removal is highly efficient, ranging between 90% and 95% across the cycles (Fig. 30). While the removal process remains generally stable, there are slight variations, particularly in the middle cycles, where the efficiency dips slightly. Maintaining high nickel removal efficiency is important to reduce pollution.

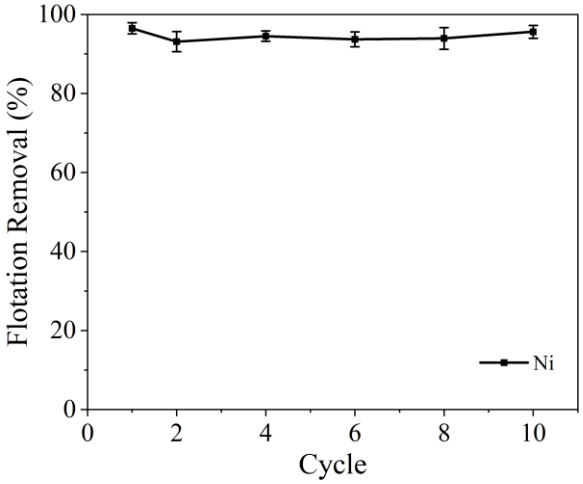


**Fig. 30.** Variation of Ni concentration at different cycles of continuous flotation tests.

The removal of zinc exhibits values between 85% and 95%, as shown in Fig. 31, with some fluctuations and a slight downward trend over time.

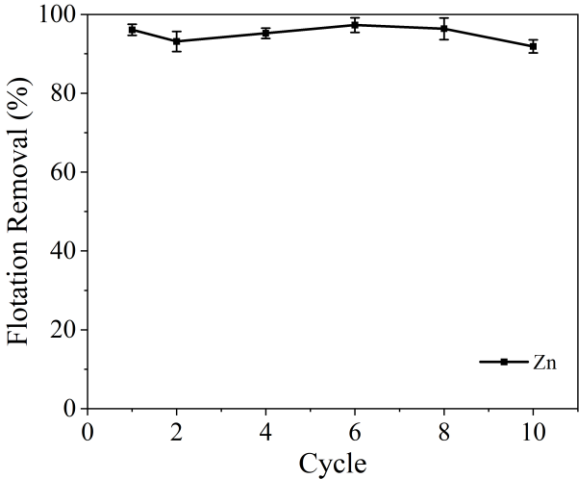


**Fig. 31.** Variation of Zn concentration at different cycles of continuous flotation tests.

Cadmium removal (Fig. 32) remains consistently high, close to 100%, with only minimal fluctuations between 95% and 100%. Cadmium is highly toxic, so its near-complete removal is essential for minimizing environmental contamination. The removal system appears stable and highly efficient over the cycles, making it reliable for long-term use.

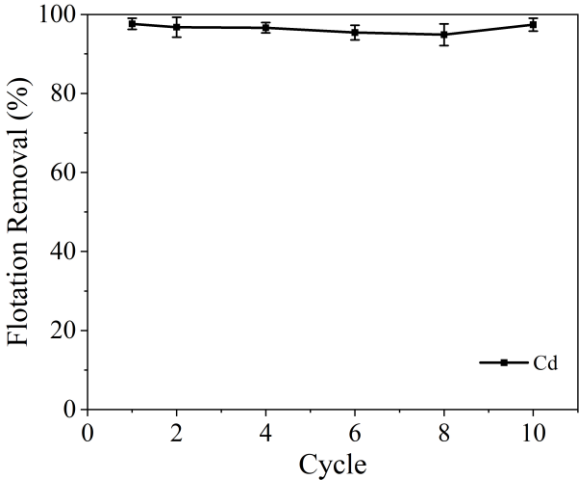


**Fig. 32.** Variation of Cd concentration at different cycles of continuous flotation tests.

Tin removal shows a slight downward trend, ranging from 90% to 95% over the cycles (Fig. 33). The minimal variation in efficiency demonstrates the reliability of the removal process for cadmium, making it a highly effective system for continuous removal.

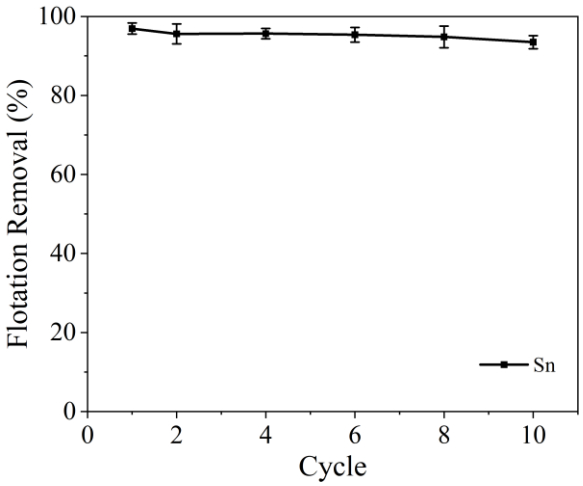


**Fig. 33.** Variation of Sn concentration at different cycles of continuous flotation tests.

Magnesium removal remains consistently high, between 90% and 95% across the cycles (Fig. 34). The system demonstrates stable removal performance, with only slight fluctuations over time. The minor fluctuations are unlikely to impact overall system performance, making the removal process reliable over long periods.

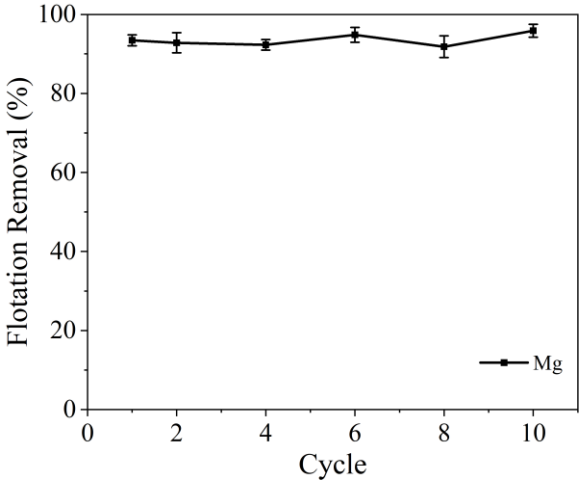


**Fig. 34.** Variation of Mg concentration at different cycles of continuous flotation tests.

Overall, the removal efficiency for all the elements analyzed remains high across the 10 cycles, with removal rates consistently above 90%. Aluminum, cadmium, cobalt, and magnesium exhibit the most stable removal rates, close to 100%, with minimal fluctuations. The high removal efficiencies across the cycles indicate that the flotation system is effective in continuous mode in removing harmful or valuable metals from AMD. Therefore, the continuous flotation system is demonstrated to be well-suited for long-term removal processes without significant losses in efficiency.

**TASK 4.0 – FILTRATION TESTS**

The filtration tests were conducted using a vacuum filtration system. This technology has advantages of: (1) The vacuum can help remove fine particles more effectively, reducing the clogging that may occur in gravity filtration and providing clearer filtrates; (2) The faster process minimizes the risk of re-dissolution of filtered substances or contamination, leading to a purer filtrate; (3) Vacuum filtration is well-suited for filtering larger volumes of liquid more quickly, making it ideal for industrial applications.

**Fig. 35.** Vacuum filtration system.

The real-world equipment for vacuum filtration system is shown in Fig. 35. The suspension obtained in air flotation test under optimal conditions will be filtrated for varying time, then the resulting sludge will be dried in an oven at 60 °C for 12 hours. To achieve efficient solid-liquid separation, 0.2 μm filter papers are utilized. The weight of filter paper was measured in advance to accurately calculate the weights of the sludge before and after drying. As a result, the solid content of the sludge was determined by calculating the difference in the weights of the sludge before and after drying.

Figure Fig**. 36** shows the solid content of the sludge increases as a function of filtration time. The data point at 0 minutes represents that the sludge was directly dried without filtration. During the initial stage (0–5 minutes), the solid content rises sharply from 0.95 wt.% to 20.47 wt.%, as most of the free water in the suspension is efficiently removed. This rapid increase is primarily due to the high permeability of the 0.2 μm filter paper and the minimal resistance from the thin sludge layer at the start of filtration. As filtration progresses (5–10 minutes), the rate of increase in solid content slows down. This is attributed to the gradual thickening of the sludge layer, which introduces additional resistance to liquid flow and reduces the efficiency of water removal. At this stage, the process transitions from free water removal to the compaction of the sludge and the elimination of interstitial water. At 10 minutes, the solid content reached 26.6 wt.%.

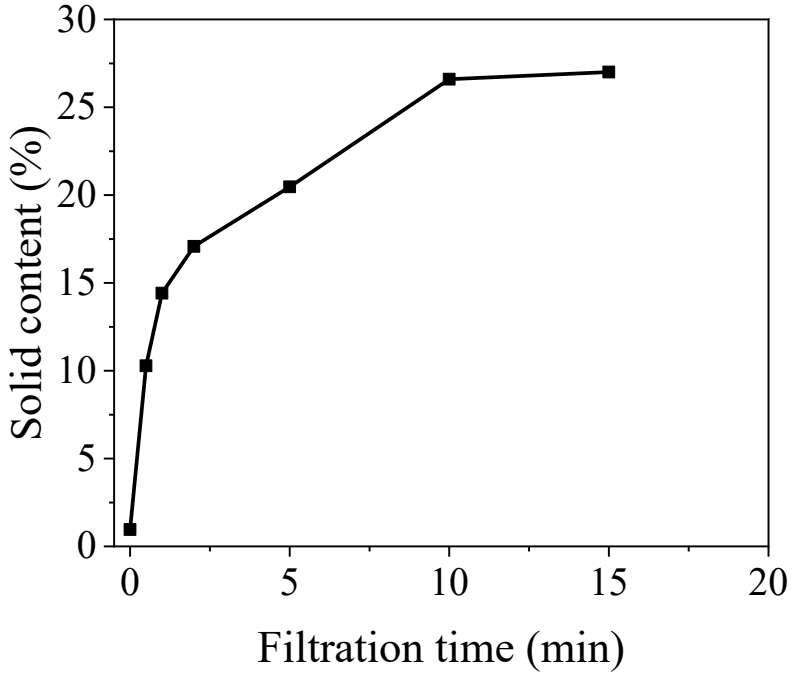


**Fig. 36.** The solid content of the sludge as a function of filtration time.

Beyond 10 minutes, the solid content begins to plateau, indicating that most of the removable water has already been extracted, with the remaining water bound within the sludge matrix. As a result, further filtration yields only marginal increases in solid content. Prolonged filtration not only offers limited benefits but also poses risks such as filter paper breakage and higher operational costs. Based on the experimental results, a filtration time of 10 minutes is sufficient to achieve a high solid content of 26.6 wt.%, ensuring an efficient balance between process effectiveness and operational practicality.

**TASK 5.0 – HIGH-DENSITY SLUDGE TESTS**

The high-density sludge circuit is the most efficient circuit that has been employed in the mining industry for acid mine drainage treatment. Therefore, for comparison purposes, high-density sludge tests are also performed on the AMD. The high-density sludge circuit consists of a lime/slurry mixer, a lime reactor, a floc tank, a clarifier, and pumps. Simulation experiments of the HDS process in AMD treatment were carried out under laboratory conditions. The optimal conditions in precipitation and air flotation experiments, including a pH of 10.0, a neutralization reagent of CaO, 10 mg/L of A-100 flocculant, and 400 mg/L of NaOL, were introduced. In each treatment, the total volume of the suspension was fixed at 3 L, and the sludge was naturally settled

for 12 hours after conditioning. After settling, the supernatant was removed as much as possible, with the minimal loss of the produced sludge. Then the fresh AMD will be supplemented into the system to maintain a total volume of 3 L, and the corresponding reagents will also be added for a new cycle. The simulated HDS system will run for several cycles, and the solid contents and ion concentration of each cycle will be evaluated. The sludge produced in the simulated HDS circuit after different cycles are shown in Fig. 37, indicating significant changes in morphology, quantity, and density as the number of treatment cycles increased.

In the early cycles (1–3), the sludge was fine and loosely packed, forming a dispersed sediment layer with low density. The particles showed limited cohesion, and the quantity of settled sludge was small due to the limited accumulation of precipitates during the initial stages. This indicated that the system required multiple cycles to begin accumulating significant amounts of sludge.

By the middle cycles (4–6), the sludge morphology became more compact, with particles forming a more cohesive structure. The quantity of settled sludge increased as more precipitates accumulated in the system. However, the density of the sludge, while improved, still suggested the presence of a considerable amount of water trapped within the sediment.

In the later cycles (8–10), the sludge became more cohesive and compact, with a denser sediment layer forming at the bottom. The quantity of sludge further increased, reflecting the cumulative nature of the treatment process. Despite these changes, the system showed a tendency to require extended treatment cycles to reach higher sludge densities, with a progressive but incremental improvement in the packing and water retention properties of the sludge.

These observations suggest that while the HDS process is capable of handling AMD treatment over multiple cycles, it inherently involves gradual accumulation and compaction of sludge, requiring significant time and repeated operations to achieve notable improvements in sludge density and morphology. The variation of the solid content of the sludge at each cycle will be evaluated.

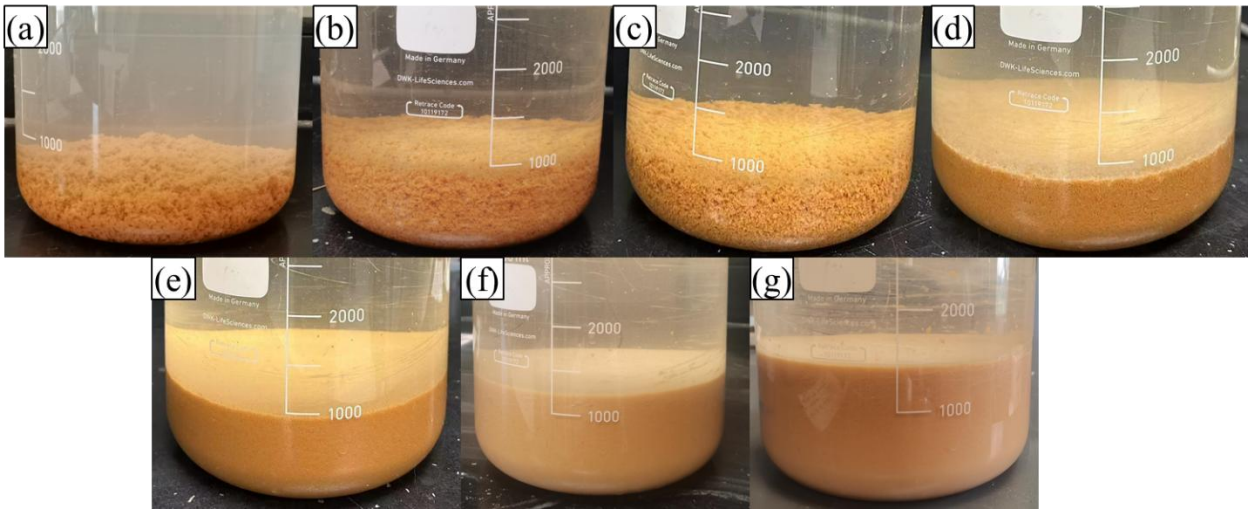


**Fig. 37.** The sludge in simulated HDS circuit after different cycles: (a) 1 cycle, (b) 2 cycles, (c) 3 cycles, (d) 4 cycles, (e) 6 cycles, (f) 8 cycles, (g) 10 cycles.

The variation of the solid content of the sludge at each cycle was evaluated, as shown in Fig. 38. A clear upward trend is observed, with sludge density gradually increasing from approximately 0.7% in the first cycle to around 6% by the tenth cycle. This progressive increase suggests that sludge recycling within the HDS system enhances particle agglomeration and promotes the formation of denser sludge over time. The steady rise across cycles highlights the cumulative effect of returning previously formed sludge to serve as nucleation sites, improving the settling and compaction characteristics of the precipitated solids. This trend confirms the effectiveness of HDS in producing increasingly dense sludge with repeated use.

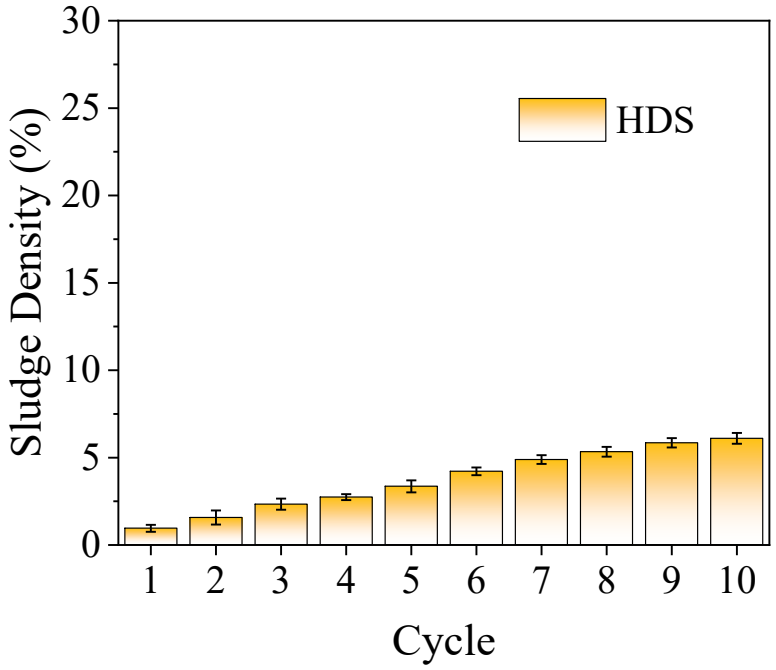


**Fig. 38.** The sludge density at different cycles in simulated HDS circuit.

## TASK 6.0 – PROCESS CIRCUIT DESIGN AND TECHNO-ECONOMIC ANALYSIS

*I. Process circuit Design*

The overall precipitation-flotation-dewatering (PFD) process circuit is successfully designed, as depicted in Fig. 39. Based on the results so far, the PFD process exhibits significant advantages of rapid solid/liquid separation and high ions removal efficiency, demonstrating significant economic benefits and potential for industrial application of AMD treatment.

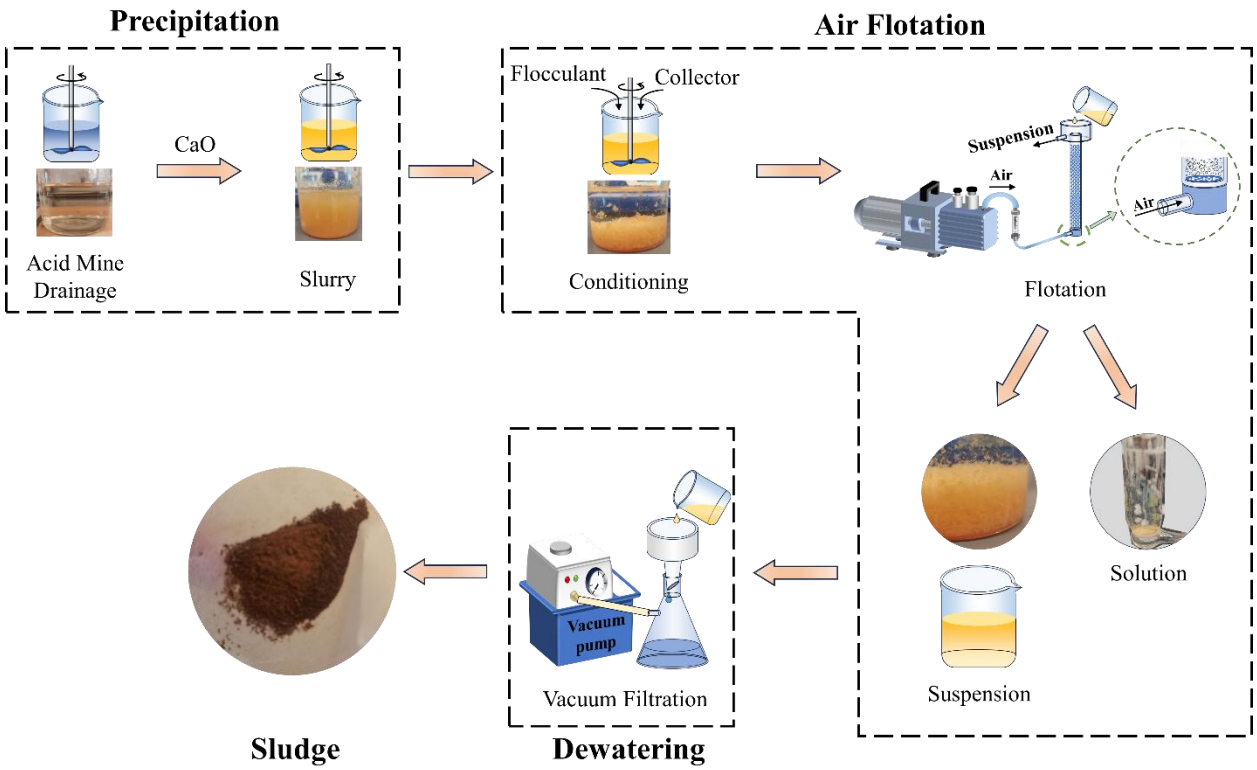


**Fig. 39.** The overall circuit of the precipitation-flotation-dewatering (PFD) process.

In previous reports, flotation experiments were conducted using a 75 mL micro-flotation cell. However, microturbulence occurred during flotation, leading to some precipitate particles remaining in the cell, as illustrated in Fig. 40(a). Thus, air flotation tests were additionally conducted using a 50 mL micro-flotation cell under optimal conditions. It's notable that the height of the 75 mL cell is 200 mm, while the 50 mL cell stands at 150 mm. The elemental contents of the treated AMD obtained with different flotation cells are also presented in Fig. 40. Enhanced removal of various ions was achieved using the 50 mL cell. As indicated in Fig. 40(b), the harmless ions of $Ca^{2+}$ and $Mg^{2+}$ were found at contents of 541.97 ppm and 1.25 ppm, respectively. Hazardous ions such as $Mn^{2+}$, $Ni^{2+}$, and $Zn^{2+}$ achieved lower contents of 0.07 ppm, 0.01 ppm, and 0.16 ppm, respectively, compared to the 70 mL cell. Meanwhile, $Co^{2+}$, $Cd^{2+}$ and $Sn^{2+}$ exhibited consistently high removals. The resulting residual liquid displayed almost no solid residue when using the 50 mL cell for flotation, as seen in Fig. 40(b). Shortening the flotation column reduced the particle flotation path, thereby improving the flotation efficiency. The flotation water addition of the air flotation using 75 mL and 50 mL cells was measured as 16 mL and 10 mL, respectively. The water quality standards, established under the EPA 40 Code (section 434.33) of Federal Regulations (CFR), signified iron content is 7.0 mg/L and total manganese content is 4.0 mg/L.

Therefore, the clean water obtained in this study meets water quality standards, and the hazardous elements were also successfully removed.

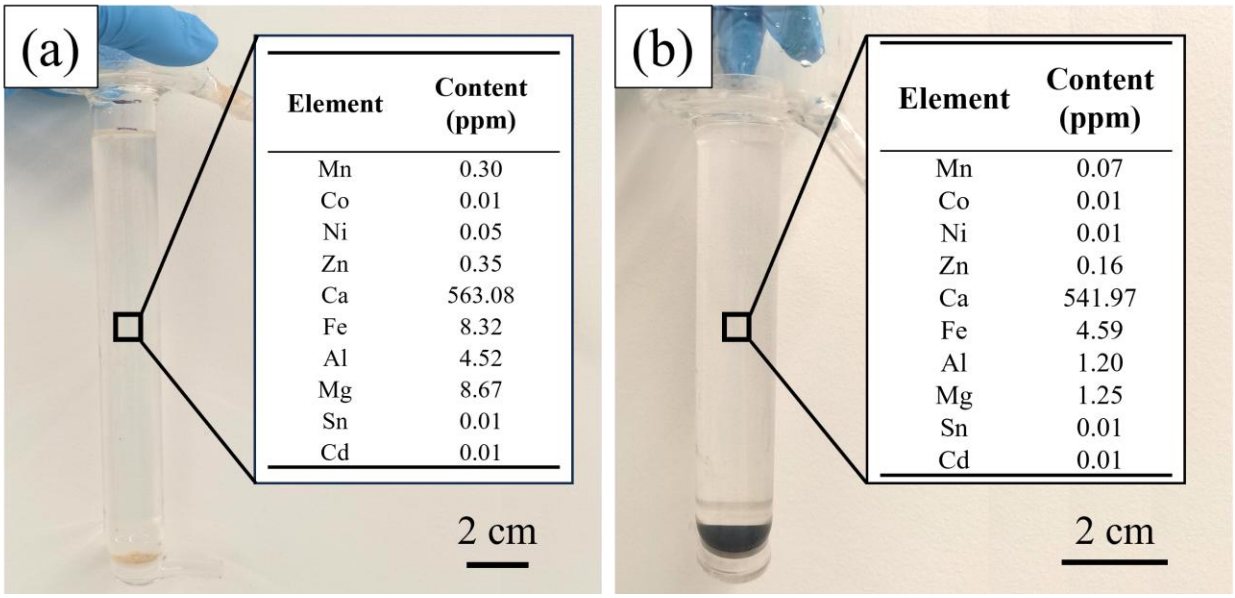


**Fig. 40.** Comparison of air flotation test conducted by (a) 75 mL cell and (b) 50 mL cell.

*II. Techno-Economic Analysis*

Several processes for treating AMD have been developed and applied since the 1960s, such as typical conventional lime neutralization process and HDS process (Aubé and Zinck 1999). Some variants of the HDS process such as Heath Steele Division (Aubé 1999), Geco Division (Aubé and Sc 2004), Mattabi (Kuyucak 2021) and Waite amulet (Amrou 2020) have been applied in industry and operating successfully for more than 20 years. The primary advantage of HDS circuits is the production of high-density sludge, which has a lower water content and higher solids concentration. This is achieved by recycling a portion of the sludge back into the neutralization reactor, where it acts as seed material for further precipitation of metals. The dense sludge formed is easier to dewater, reducing the volume and cost of sludge disposal. Although HDS systems reduce lime consumption, the need for additional reagents such as flocculants or coagulants can increase operational costs. The selection and optimization of these chemicals are crucial for efficient system performance. Researchers have made efforts to optimize the neutralization process or develop new processes. For example, two-step neutralization process was developed and reduced sludge volume of 20-80% (Herrera, Uchiyama et al. 2007). Newly agents was also used to remove >90% of several toxic or problematic metals from AMD (Matlock, Howerton and Atwood 2002). More than

99% of Al and Fe were removed with a bioelectrochemical system, and removal rates of 93%, 91%, 89% and 69% were achieved for Cd, Zn, Mn and Co respectively (Peiravi, Mote et al. 2017). Continuous alkaline barium calcium desalination process can remove sulphate from 2250 ppm to 100 ppm, and ensure no residual toxic barium is present in the treated water (Mulopo 2015). Physical methods of natural zeolites have also been applied to adsorb heavy metals from AMD, with removal efficiencies of 80%, 95%, 90% and 99% for $Fe^{3+}$, $Mn^{2+}$, $Zn^{2+}$, and $Cu^{2+}$, respectively (Motsi, Rowson and Simmons 2009). These processes exhibit high efficiency in treating AMD, but they still have disadvantages of high costs, secondary pollution, or not meet the demands for large-scale AMD treatment. Therefore, the HDS process is still the most commonly used commercial process in the AMD treatment industry.

As shown in Task 5.0, the HDS process relies on long-term sedimentation, presenting challenges such as the accumulation of bound water in sludge and extended treatment times, particularly problematic given the rapid and large-scale production of AMD by mines, which can generate hundreds to thousands of tons per day. Additionally, the thickeners in HDS have a large footprint (30-30000 $m^2$), which is difficult to assemble, disassemble, and relocate.

In contrast, the efficient PFD process developed in this study achieves effective removal of metal ions from AMD, rivaling or surpassing previous research, while the generated sludge exhibited a notably high solid content, even in comparison to the HDS process, as seen in Table 3. Unlike the HDS process, the PFD process does not require sludge recirculation and can produce high density sludge within 30 minutes, which mitigates the accumulation of bound water in the sludge and meets the rapid and large-scale demands of AMD treatment. The timely treatment of mine wastewater is critical for ensuring mine safety. For instance, slow settlement and the inability to form a dry beach when treating tailings pond wastewater significantly increase the risk of leakage and overflow, creating serious safety hazards. Therefore, the PFD process has positive environmental impacts on reducing the environmental damage of storing AMD. On the other hand, the compact flotation column in PFD occupies minimal space of 1-30 $m^2$, allowing convenient relocation when mining activities transition to new areas, thereby reducing economic burdens on mining companies and conserving precious land resources. Although the PFD process requires flotation agents such as PAM and NaOL, they can be easily degraded in the environment, and the emissions in PFD process would hardly cause adverse impacts on the environment.

**Table 3.** Comparison of PFD process and existing HDS processes.

| Site | Process | Lime | Treatment time | Sludge density (% solid) | Facility footprint |
|---|---|---|---|---|---|
| Geco | Geco HDS | Quicklime | > 20 hours | 27.8 | 30 – 30000 $m^2$ |
| Heath Steele | HDS | Quicklime | | 20.8 | |
| Mattabi | HDS | Quicklime | | 16.1 | |
| Waite amulet | HDS | Hydrated | | 18.0 | |
| This study | PFD | Quicklime | < 30 minutes | 26.6 | 1 – 30 $m^2$ |

In large-scale applications, the size of flotation columns can significantly differ from laboratory conditions. Although shortening the flotation column has been proved to efficiently improve the flotation efficiency, the most feasible size of flotation columns in practical applications depends on various factors such as available space, equipment constraints, and economic considerations. Fortunately, low-profile flotation columns are already well-established in the industry and can be designed with various diameter-to-height ratios. Therefore, the PFD process has substantial potential for large-scale application and industrial implementation.

Detail comparison between HDS and the novel PFD process used in this project was conducted. Figure Fig**. 41** compares the sludge density evolution over 10 treatment cycles between the HDS process and the PFD process on AMD treatment.

The PFD process (represented by the black line) maintains a consistently high sludge density of around 25–26% throughout all 10 cycles. This indicates excellent sludge compaction and process stability. The high and stable sludge density suggests that PFD effectively separates and concentrates metal precipitates from AMD even in the early treatment cycles.

In contrast, the HDS process (represented by the yellow bars) exhibits a gradual increase in sludge density from about 0.7% in Cycle 1 to about 6% by Cycle 10. This increasing trend reflects the cumulative buildup of recycled sludge solids in the system, which progressively enhances nucleation and precipitation of metal hydroxides. HDS relies on sludge recycling to achieve denser precipitates over time, and its performance improves as more treatment cycles are completed.

Comparatively, the PFD process provides a high sludge density from the beginning, while the HDS process requires multiple cycles to gradually approach higher sludge compaction. Even at Cycle 10, the HDS sludge density remains significantly lower than that of PFD, indicating that PFD is more efficient in achieving denser sludge under similar conditions.

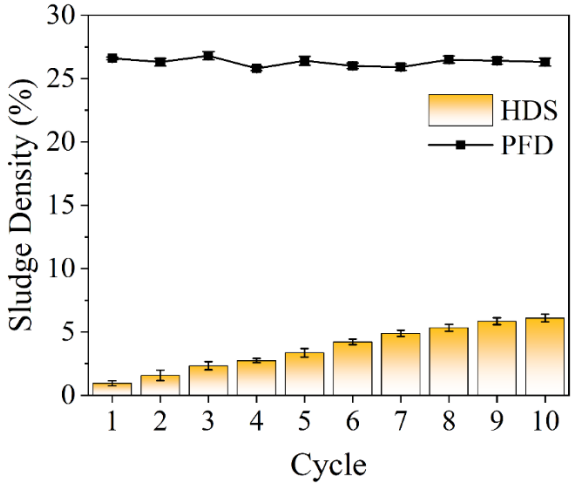


**Fig. 41.** Comparison of the sludge density at different cycles in simulated HDS and the novel PFD circuits.

The final AMD treated by continuous PFD and simulated HDS processes as well as the resulting sludge density was compared. As shown in Table 4, the results of the simulated HDS circuit showed effective ion removal after 10 days. However, the sludge density was only 6.1%, and a large amount of sludge had to be returned each time, which increased the system load and reduced the treatment efficiency. Other indexes such as sulfate, turbidity, color, and COD are also higher than PFD. In comparison, the advantages of the PFD process in terms of efficiency and speed were further revealed.

**Table 4.** Ion concentrations (mg/L), pH, turbidity (NTU), color (PtCo), COD (ppm), and sludge density (% solid) of continuous PFD and simulated HDS process.

| | HDS | PFD | | HDS | PFD |
|---|---|---|---|---|---|
| Mn | 0.02 | 0.05 | Sn | 0.01 | 0.06 |
| Co | 0.00 | 0.00 | Cd | 0.01 | 0.00 |
| Ni | 0.01 | 0.01 | Sulfate | 3810 | 3350 |
| Zn | 0.52 | 0.00 | pH | 9~10 | 9~10 |
| Ca | 894.53 | 619.44 | Turbidity | 29 | 1.1 |
| Al | 0.05 | 0.05 | Color | 153 | 19 |
| Mg | 29.99 | 19.77 | COD | 75.67 | 33.08 |
| Fe | 3.03 | 4.08 | Sludge density | 6.1 | 26~27 |

The cost analysis of PFD process was conducted and compared to HDS process. Assume the flotation column is designed as 6 meters height with a diameter of 0.8 meters, and the residence time in flotation column is 10 minutes, then the treatment ability of the PFD process would be 18 $m^3$/hour. Assume the residence time in thickener is 24 hours, then the HDS process with the same

treatment ability require a thickener of 15 meters diameter with 2.5 meters depth. An estimation of equipment and chemical costs for treating 18 $m^3$/hour AMD (sodium oleate dosage = 100 g/$m^3$, and flocculant dosage = 10 g/$m^3$; equipment costs were referred to https://www.costmine.com/ and http://www.matche.com/default.html) were presented in Table 5. Costs associated with the precipitation step were excluded since it exists in both PFD and HDS processes. It can be found that the equipment cost in the PFD process is much lower compared to that for HDS process, while the HDS process has lower chemical costs. The PFD process is easily relocatable and does not necessitate a complex pipeline transport system like the HDS process, thus offering expected further decrease in equipment costs. In addition, due to the rapid kinetics of flotation and filtration, the operational and residence time of the PFD process is significantly shorter than that of the HDS process, offering notable advantages in terms of energy usage and labor. Also, the recirculation of sludge would exacerbate the HDS system load, resulting in larger thickeners. Results from section 3.4 indicate that the treatment time in HDS process will be much longer than we expected to obtain high density sludge, thereby significantly increasing the energy consumption and labor cost. The chemical cost of PFD process is higher, which can be addressed using low-cost collectors such as waste engine oil (Fan, Zhang et al. 2021) and waste cooking oils (Cheng, Zhang et al. 2020). Additionally, the cost comparison between PFD process, sulfate-reduction-based biological process, and other chemical processes is provided in Table 6. Based on our analysis, we conclude that the PFD process exhibits satisfactory cost-effectiveness.

**Table 5.** An estimation of equipment and chemical costs for treating 18 $m^3$/hour AMD.

| | | | PFD | | HDS | |
|---|---|---|---|---|---|---|
| Equipment | Size | Unit cost ($) | Number | Cost ($) | Number | Cost ($) |
| Flotation column | 2 $m^3$ | 50,000 | 1 | 50,000 | 0 | 0 |
| Filter press | 200 $ft^2$ | 86,500 | 1 | 86,500 | 0 | 0 |
| Thickener | 15 m diameter | 305,000 | 0 | 0 | 1 | 305,000 |
| | | **Total Equipment** | | 136,500 | | 305,000 |
| Chemical | Specification | Unit cost ($/kg) | Consumption | Cost ($/hour) | Consumption | Cost ($/hour) |
| Sodium Oleate | Industrial grade | 2 | 1.8 kg/hour | 3.6 | 0 | 0 |
| Flocculant | Industrial grade | 1.5 | 0.12 kg/hour | 0.3 | 0.12 kg/hour | 0.3 |
| | | **Total chemical** | | 3.9 | | 0.3 |

**Table 6.** Cost comparison between PFD process, sulfate-reduction-based biological process, and other chemical processes.

| Process | Cost ($/m$^3$) |
|---|---|
| PFD | 2-5 |
| HDS | 5-8 (Mapukata, Mudzanani et al. 2024) |
| Sulfate-reduction-based biological process | 5-10 (Salo and Bomberg 2022) |
| Bioelectrochemical process | 5-10 (Ai, Hou et al. 2020) |
| Continuous alkaline barium calcium desalination process | 2.5-5 (Van Rooyen, van Staden and du Preez 2021) |

In conclusion, the efficient PFD process offers rapid and efficient AMD treatment, yielding high-density sludge and meeting the large-scale processing demands of AMD. Departing from the traditional sedimentation method in HDS, this innovative process employs flotation, markedly accelerating processing velocity while substantially slashing facility and land costs. Its notable industrial viability is emphasized by its compact footprint requirements and heightened efficiency, poised to supplant the HDS process as the next-generation solution for AMD treatment. This advancement not only bolsters environmental sustainability but also seamlessly aligns with the United Nations Sustainable Development Goals (SDGs) (Kefeni, Msagati and Mamba 2017, Mondejar, Avtar et al. 2021).

## TASK 7.0 – FUNDAMENTAL STUDIES

*I. Solution chemical analysis of metal ions*

As the pH value of the solution increases, precipitate of metallic hydroxide will generate. The pH at which precipitate begins to form depends on the initial concentration of metal ions. The initial molar concentrations of metal ions can be obtained from Task 1.0 after conversion. Identify the aqueous system before the precipitation appears as the homogeneous system, and the suspension system as heterogeneous system.

The reactions in iron ions homogeneous system and the corresponding reaction constants were listed in Table 7. The initial concentration of iron ions is $3.45 \times 10^{-3}$ mol/L.

**Table 7.** The reactions and the reaction constants in iron ions homogeneous system.

| Reactions | Reaction Constants | |
|---|---|---|
| $Fe^{3+} + OH^- \rightleftharpoons FeOH^{2+}$ | $\beta_{Fe1} = 10^{11.81}$ | (4) |
| $Fe^{3+} + 2OH^- \rightleftharpoons Fe(OH)_2^+$ | $\beta_{Fe2} = 10^{22.3}$ | (5) |
| $Fe^{3+} + 3OH^- \rightleftharpoons Fe(OH)_{3(aq)}$ | $\beta_{Fe3} = 10^{32.05}$ | (6) |

$$Fe^{3+} + 4OH^- \rightleftharpoons Fe(OH)_4^- \qquad \beta_{Fe4} = 10^{34.3} \tag{7}$$

where β is the reaction constant.

The calculation formulas for the concentration of each component in the iron ion homogeneous system are as follows:

$$\alpha_{Fe^{3+}} = 1 + \beta_{Fe1}[OH^-] + \beta_{Fe2}[OH^-]^2 + \beta_{Fe3}[OH^-]^3 + \beta_{Fe4}[OH^-]^4 \tag{8}$$

$$[Fe^{3+}] = C_{Fe}/\alpha_{Fe^{3+}} \tag{9}$$

$$[FeOH^{2+}] = [Fe^{3+}]\beta_{Fe1}[OH^-] \tag{10}$$

$$[Fe(OH)_2^+] = [Fe^{3+}]\beta_{Fe2}[OH^-]^2 \tag{11}$$

$$[Fe(OH)_{3(aq)}] = [Fe^{3+}]\beta_{Fe3}[OH^-]^3 \tag{12}$$

$$[Fe(OH)_4^-] = [Fe^{3+}]\beta_{Fe4}[OH^-]^4 \tag{13}$$

where $C_{Fe}$ is the total concentration of iron ions, and $\alpha_{Fe^{3+}}$ is the side reaction coefficient.

The reactions in iron ions heterogeneous system and the corresponding reaction constants were listed in Table 8.

**Table 8.** The reactions and the reaction constants in iron ions heterogeneous system

| Reactions | Reaction Constants | |
|---|---|---|
| $Fe(OH)_{3(s)} \rightleftharpoons Fe^{3+} + 3OH^-$ | $K_{Fes0} = 10^{-38.55}$ | (14) |
| $Fe(OH)_{3(s)} \rightleftharpoons Fe(OH)_2^+ + 2OH^-$ | $K_{Fes1} = \beta_{Fe1}K_{Fes0}$ | (15) |
| $Fe(OH)_{3(s)} \rightleftharpoons Fe(OH)^{2+} + OH^-$ | $K_{Fes2} = \beta_{Fe2}K_{Fes0}$ | (16) |
| $Fe(OH)_{3(s)} \rightleftharpoons Fe(OH)_{3(aq)}$ | $K_{Fes3} = \beta_{Fe3}K_{Fes0}$ | (17) |
| $Fe(OH)_{3(s)} + OH^- \rightleftharpoons Fe(OH)_4^-$ | $K_{Fes4} = \beta_{Fe4}K_{Fes0}$ | (18) |

The calculation formulas for the concentration of each component in the iron ions heterogeneous system are as follows:

$$[Fe^{3+}] = K_{Fes0}/[OH^-]^3 \tag{19}$$

$$[FeOH^{2+}] = K_{Fes1}/[OH^-]^2 \tag{20}$$

$$[Fe(OH)_2^+] = K_{Fes2}/[OH^-] \tag{21}$$

$$[Fe(OH)_3(aq)] = K_{Fes3} \tag{22}$$

$$[Fe(OH)_4^-] = K_{Fes4}[OH^-] \tag{23}$$

$$\left[Fe(OH)_{3(s)}\right] = C_{Fe} - [Fe^{3+}] - [FeOH^{2+}] - [Fe(OH)_2^+] - [Fe(OH)_{3(aq)}] - [Fe(OH)_4^-] \tag{24}$$

Based on the formulars below, the species distribution of 3.45 × $10^{-3}$ mol/L iron ions were calculated, as shown in Fig. 42.

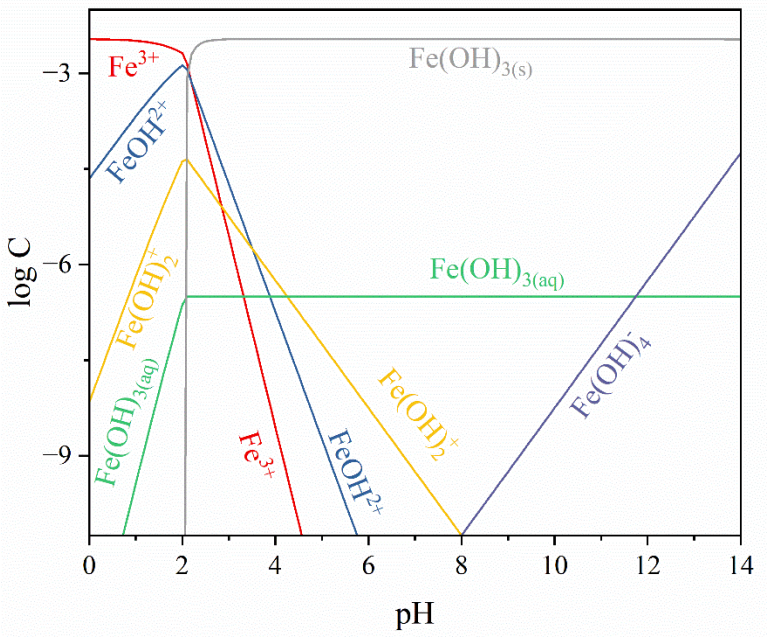


**Fig. 42.** Species distribution diagram of 3.45 × $10^{-3}$ mol/L iron ions.

As shown in Fig. 42, theoretically, $Fe(OH)_{3(s)}$ first showed up at a pH as low as 2.1 and maintained stable till pH of 14.0, as the increase of pH. Also, the concentrations of $Fe(OH)_2^+$ and $Fe(OH)^{2+}$ increase and then decrease after reaching the highest concentration at a pH value of 2.1. The anion specie of $Fe(OH)_4^-$ appears at a pH of 8.0 and increases with the increasing pH value.

The initial concentration of aluminum ions is 3.87 × $10^{-3}$ mol/L. The reactions in aluminum ions homogeneous system and the corresponding reaction constants were listed in Table 9.

**Table 9.** The reactions and the reaction constants in aluminum ions homogeneous system.

| Reactions | Reaction Constants | |
|---|---|---|
| $Al^{3+} + OH^- \rightleftharpoons AlOH^{2+}$ | $\beta_{Al1} = 10^{9.27}$ | (25) |
| $Al^{3+} + 2OH^- \rightleftharpoons Al(OH)_2^+$ | $\beta_{Al2} = 10^{18.7}$ | (26) |
| $Al^{3+} + 3OH^- \rightleftharpoons Al(OH)_{3(aq)}$ | $\beta_{Al3} = 10^{27}$ | (27) |
| $Al^{3+} + 4OH^- \rightleftharpoons Al(OH)_4^-$ | $\beta_{Al4} = 10^{33.03}$ | (28) |

The calculation formulas for the concentration of each component in the aluminum ion homogeneous system are as follows:

$$\alpha_{Al^{3+}} = 1 + \beta_{Al1}[OH^-] + \beta_{Al2}[OH^-]^2 + \beta_{Al3}[OH^-]^3 + \beta_{Al4}[OH^-]^4 \quad (29)$$

$$[Al^{3+}] = C_{Al}/\alpha_{Al^{3+}} \quad (30)$$

$$[AlOH^{2+}] = [Al^{3+}]\beta_{Al1}[OH^-] \quad (31)$$

$$[Al(OH)_2^+] = [Al^{3+}]\beta_{Al2}[OH^-]^2 \quad (32)$$

$$[Al(OH)_{3(aq)}] = [Al^{3+}]\beta_{Al3}[OH^-]^3 \quad (33)$$

$$[Al(OH)_4^-] = [Al^{3+}]\beta_{Al4}[OH^-]^4 \quad (34)$$

where $C_{Al}$ is the total concentration of aluminum ions, and $\alpha_{Al^{3+}}$ is the side reaction coefficient.

The reactions in aluminum ions heterogeneous system and the corresponding reaction constants were listed in Table 10.

**Table 10.** The reactions and the reaction constants in aluminum ions heterogeneous system.

| Reactions | Reaction Constants | |
|---|---|---|
| $Al(OH)_{3(s)} \rightleftharpoons Al^{3+} + 3OH^-$ | $K_{Als0} = 10^{-32.89}$ | (35) |
| $Al(OH)_{3(s)} \rightleftharpoons Al(OH)_2^+ + 2OH^-$ | $K_{Als1} = \beta_{Al1}K_{Als0}$ | (36) |
| $Al(OH)_{3(s)} \rightleftharpoons Al(OH)^{2+} + OH^-$ | $K_{Als2} = \beta_{Al2}K_{Als0}$ | (37) |
| $Al(OH)_{3(s)} \rightleftharpoons Al(OH)_{3(aq)}$ | $K_{Als3} = \beta_{Al3}K_{Als0}$ | (38) |
| $Al(OH)_{3(s)} + OH^- \rightleftharpoons Al(OH)_4^-$ | $K_{Als4} = \beta_{Al4}K_{Als0}$ | (39) |

The calculation formulas for the concentration of each component in the aluminum ions heterogeneous system are as follows:

$$[Al^{3+}] = K_{Als0}/[OH^-]^3 \quad (40)$$

$$[AlOH^{2+}] = K_{Als1}/[OH^-]^2 \quad (41)$$

$$[Al(OH)_2^+] = K_{Als2}/[OH^-] \quad (42)$$

$$[Al(OH)_{3(aq)}] = K_{Als3} \quad (43)$$

$$[Al(OH)_4^-] = K_{Als4}[OH^-] \quad (44)$$

$$[Al(OH)_{3(s)}] = C_{Al} - [Al^{3+}] - [AlOH^{2+}] - [Al(OH)_2^+] - [Al(OH)_{3(aq)}] - [Al(OH)_4^-] \quad (45)$$

Based on the formulars below, the species distribution of $3.87 \times 10^{-3}$ mol/L aluminum ions were calculated, as shown in Fig. 43.

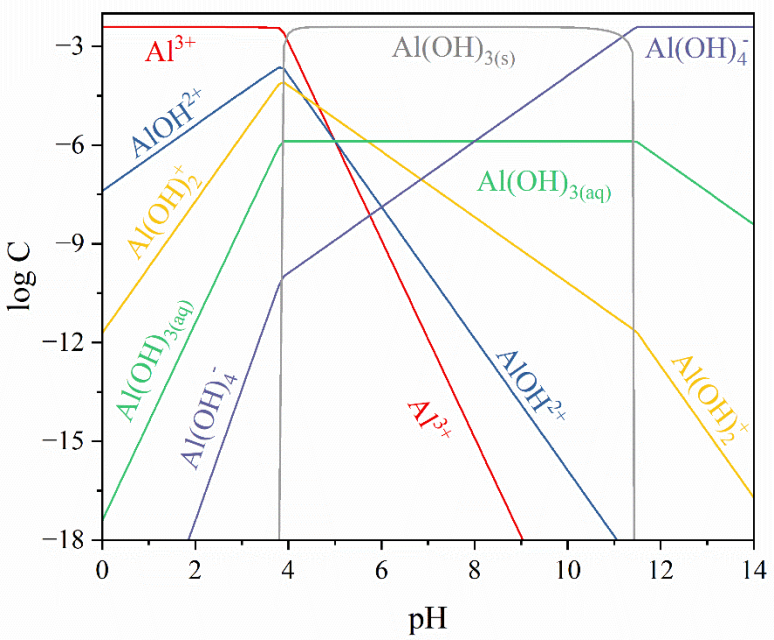


**Fig. 43.** Species distribution diagram of $3.87 \times 10^{-3}$ mol/L aluminum ions.

As shown in Fig. 43, the precipitate of $Al(OH)_3$ exists between a pH of 3.8 and 11.4. As a result, it is not suggested to adjust the pH of AMD to over 11.4. In addition, the concentrations of $Al(OH)_2^+$ and $Al(OH)^{2+}$ increase and then decrease after reaching the highest concentration at a pH value of 3.8. After the pH reached 11.4, the concentration of $Al(OH)^{2+}$ decreased faster. The anion specie of $Al(OH)_4^-$ increased from pH 0 to pH 11.4 with a lower slope from pH 3.8.

The reactions in manganese ions homogeneous system and the corresponding reaction constants were listed in Table 11. The initial concentration of manganese ions is $1.48 \times 10^{-4}$ mol/L.

**Table 11.** The reactions and the reaction constants in manganese ions homogeneous system.

| Reactions | Reaction Constants | |
|---|---|---|
| $Mn^{2+} + OH^- \rightleftharpoons MnOH^+$ | $\beta_{Mn1} = 10^{3.40}$ | (46) |
| $Mn^{2+} + 2OH^- \rightleftharpoons Mn(OH)_{2(aq)}$ | $\beta_{Mn2} = 10^{5.80}$ | (47) |
| $Mn^{2+} + 3OH^- \rightleftharpoons Mn(OH)_3^-$ | $\beta_{Mn3} = 10^{7.20}$ | (48) |
| $Mn^{2+} + 4OH^- \rightleftharpoons Mn(OH)_4^{2-}$ | $\beta_{Mn4} = 10^{7.70}$ | (49) |

where β is the reaction constant.

The calculation formulas for the concentration of each component in the manganese ion homogeneous system are as follows:

$$\alpha_{Mn^{2+}} = 1 + \beta_{Mn1}[OH^-] + \beta_{Mn2}[OH^-]^2 + \beta_{Mn3}[OH^-]^3 + \beta_{Mn4}[OH^-]^4 \quad (50)$$

$$[Mn^{2+}] = C_{Mn}/\alpha_{Mn^{2+}} \quad (51)$$

$$[MnOH^{+}] = [Mn^{2+}]\beta_{Mn1}[OH^{-}] \quad (52)$$

$$[Mn(OH)_{2(aq)}] = [Mn^{2+}]\beta_{Mn2}[OH^{-}]^2 \quad (53)$$

$$[Mn(OH)_3^{-}] = [Mn^{2+}]\beta_{Mn3}[OH^{-}]^3 \quad (54)$$

$$[Mn(OH)_4^{-}] = [Mn^{2+}]\beta_{Mn4}[OH^{-}]^4 \quad (55)$$

where $C_{Mn}$ is the total concentration of manganese ions, and $\alpha_{Mn^{2+}}$ is the side reaction coefficient.

The reactions in manganese ions heterogeneous system and the corresponding reaction constants were listed in Table 12.

**Table 12.** The reactions and the reaction constants in manganese ions heterogeneous system.

| Reactions | Reaction Constants | |
|---|---|---|
| $Mn(OH)_{2(s)} \rightleftharpoons Mn^{2+} + 2OH^{-}$ | $K_{Mns0} = 10^{-12.72}$ | (56) |
| $Mn(OH)_{2(s)} \rightleftharpoons Mn(OH)^{+} + OH^{-}$ | $K_{Mns1} = \beta_{Mn1}K_{Mns0}$ | (57) |
| $Mn(OH)_{2(s)} \rightleftharpoons Mn(OH)_{2(aq)}$ | $K_{Mns2} = \beta_{Mn2}K_{Mns0}$ | (58) |
| $Mn(OH)_{2(s)} + OH^{-} \rightleftharpoons Mn(OH)_3^{-}$ | $K_{Mns3} = \beta_{Mn3}K_{Mns0}$ | (59) |
| $Mn(OH)_{2(s)} + 2OH^{-} \rightleftharpoons Mn(OH)_4^{2-}$ | $K_{Mns4} = \beta_{Mn4}K_{Mns0}$ | (60) |

The calculation formulas for the concentration of each component in the manganese ions heterogeneous system are as follows:

$$[Mn^{2+}] = K_{Mns0}/[OH^{-}]^2 \quad (61)$$

$$[MnOH^{+}] = K_{Mns1}/[OH^{-}] \quad (62)$$

$$[Mn(OH)_{2(aq)}] = K_{Mns2} \quad (63)$$

$$[Mn(OH)_3^{-}] = K_{Mns3}[OH^{-}] \quad (64)$$

$$[Mn(OH)_4^{2-}] = K_{Mns4}[OH^{-}]^2 \quad (65)$$

$$\left[Mn(OH)_{2(s)}\right] = C_{Mn} - [Mn^{2+}] - [Mn(OH)^{+}] - \left[Mn(OH)_{2(aq)}\right] - [\mathrm{Mn}(OH)_3^{-}] - [Mn(OH)_4^{2-}] \quad (66)$$

Based on the formulars, the species distribution of $1.48 \times 10^{-4}$ mol/L manganese ions were calculated, as shown in Fig. 44.

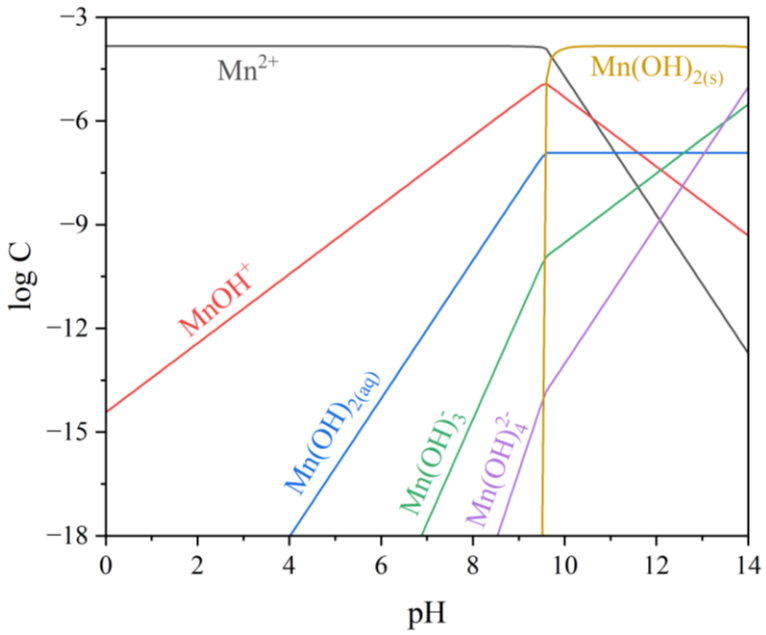


**Fig. 44.** Species distribution diagram of $1.48 \times 10^{-4}$ mol/L manganese ions.

As shown in Fig. 44, theoretically, the formation of $Mn(OH)_{2(s)}$ occurred at a pH of 9.6 and maintained stable till pH 14.0, as the increase of pH. The concentrations of $Mn(OH)^{+}$ increase and then decrease after the formation of $Mn(OH)_{2(s)}$. The anion specie of $Mn(OH)_3^-$ and $Mn(OH)_4^{2-}$ increase appears at a pH of 8.0 and increases with the increasing pH value.

The initial concentration of cobalt ions is $6.11 \times 10^{-6}$ mol/L. The reactions in cobalt ions homogeneous system and the corresponding reaction constants were listed in Table 13.

**Table 13.** The reactions and the reaction constants in cobalt ions homogeneous system.

| Reactions | Reaction Constants | |
|---|---|---|
| $Co^{2+} + OH^- \rightleftharpoons CoOH^+$ | $\beta_{Co1} = 10^{3.76}$ | (67) |
| $Co^{2+} + 2OH^- \rightleftharpoons Co(OH)_{2(aq)}$ | $\beta_{Co2} = 10^{9.38}$ | (68) |

The calculation formulas for the concentration of each component in the cobalt ion homogeneous system are as follows:

$$\alpha_{Co^{2+}} = 1 + \beta_{Co1}[OH^-] + \beta_{Co2}[OH^-]^2 \quad (69)$$

$$[Co^{2+}] = C_{Co}/\alpha_{Co^{2+}} \quad (70)$$

$$[CoOH^+] = [Co^{2+}]\beta_{Co1}[OH^-] \quad (71)$$

$$[Co(OH)_{2(aq)}] = [Co^{2+}]\beta_{Co2}[OH^-]^2 \quad (72)$$

$$\alpha_{Co^{2+}} = 1 + \beta_{Co1}[OH^-] + \beta_{Co2}[OH^-]^2 \quad (73)$$

$$[Co^{2+}] = C_{Co}/\alpha_{Co^{2+}} \quad (74)$$

where $C_{Co}$ is the total concentration of cobalt ions, and $\alpha_{Co^{2+}}$ is the side reaction coefficient.

The reactions in cobalt ions heterogeneous system and the corresponding reaction constants were listed in Table 14.

**Table 14.** The reactions and the reaction constants in cobalt ions heterogeneous system.

| Reactions | Reaction Constants | |
|---|---|---|
| $Co(OH)_{2(s)} \rightleftharpoons Co^{2+} + 2OH^-$ | $K_{Cos0} = 10^{-14.23}$ | (75) |
| $Co(OH)_{2(s)} \rightleftharpoons Co(OH)^+ + OH^-$ | $K_{Cos1} = \beta_{Co1}K_{Cos0}$ | (76) |
| $Co(OH)_{2(s)} \rightleftharpoons Co(OH)_{2(aq)}$ | $K_{Cos2} = \beta_{Co2}K_{Cos0}$ | (77) |

The calculation formulas for the concentration of each component in the cobalt ions heterogeneous system are as follows:

$$[Co^{2+}] = K_{Cos0}/[OH^-]^2 \quad (78)$$

$$[Co(OH)^+] = K_{Cos1}/[OH^-] \quad (79)$$

$$[Co(OH)_{2(aq)}] = K_{Cos2} \quad (80)$$

$$\left[Co(OH)_{2(s)}\right] = C_{Co} - [Co^{2+}] - [Co(OH)^+] - \left[Co(OH)_{2(aq)}\right] \quad (81)$$

$$[Co^{2+}] = K_{Cos0}/[OH^-]^2 \quad (82)$$

$$[Co(OH)^+] = K_{Cos1}/[OH^-] \quad (83)$$

Based on the formulars, the species distribution of 6.11 × $10^{-6}$ mol/L cobalt ions were calculated, as shown in Fig. 45.

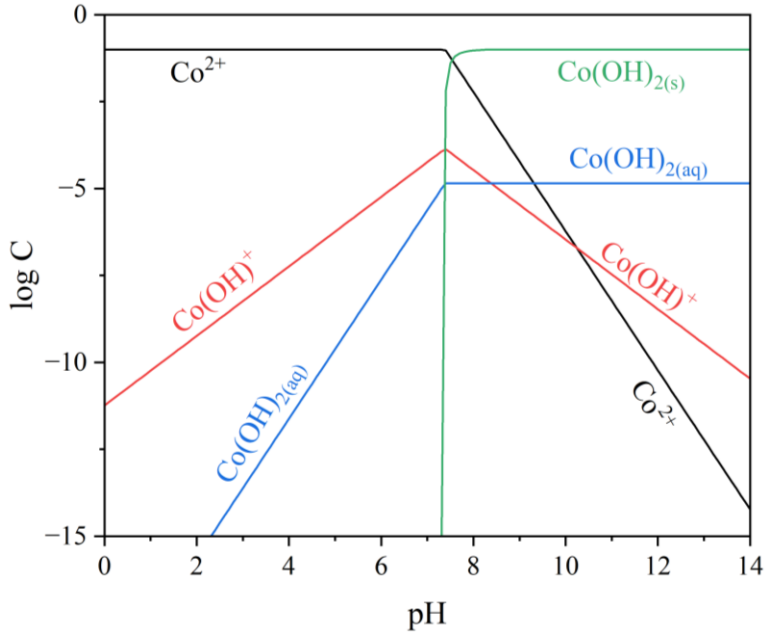


**Fig. 45.** Species distribution diagram of $6.11 \times 10^{-6}$ mol/L cobalt ions.

As shown in Fig. 45, the precipitate of $Co(OH)_3$ formed at a pH of 7.4, then remained stable till pH 14.0. In addition, the concentrations of $Co(OH)^+$ increase and then decrease after reaching the highest concentration at a pH value of 7.4. The concentration of $Co^{2+}$ decreases after the formation of $Co(OH)_{2(s)}$.

The reactions in nickel ions homogeneous system and the corresponding reaction constants were listed in Table 15. The initial concentration of nickel ions is $2.61 \times 10^{-5}$ mol/L.

**Table 15.** The reactions and the reaction constants in nickel ions homogeneous system.

| Reactions | Reaction Constants | |
|---|---|---|
| $Ni^{2+} + OH^- \rightleftharpoons NiOH^+$ | $\beta_{Ni1} = 10^{4.97}$ | (84) |
| $Ni^{2+} + 2OH^- \rightleftharpoons Ni(OH)_{2(aq)}$ | $\beta_{Ni2} = 10^{8.55}$ | (85) |
| $Ni^{2+} + 3OH^- \rightleftharpoons Ni(OH)_3^-$ | $\beta_{Ni2} = 10^{11.33}$ | (86) |

where β is the reaction constant.

The calculation formulas for the concentration of each component in the nickel ion homogeneous system are as follows:

$$\alpha_{Ni^{2+}} = 1 + \beta_{Ni1}[OH^-] + \beta_{Ni2}[OH^-]^2 + \beta_{Ni3}[OH^-]^3 \quad (87)$$

$$[Ni^{2+}] = C_{Ni}/\alpha_{Ni^{2+}} \quad (88)$$

$$[NiOH^+] = [Ni^{2+}]\beta_{Ni1}[OH^-] \quad (89)$$

$$[Ni(OH)_{2(aq)}] = [Ni^{2+}]\beta_{Ni2}[OH^-]^2 \quad (90)$$

$$[\mathrm{Ni}(OH)_3^-] = [NI^{2+}]\beta_{Ni3}[OH^-]^3 \quad (91)$$

where $C_{Ni}$ is the total concentration of nickel ions, and $\alpha_{Ni^{2+}}$ is the side reaction coefficient.

The reactions in nickel ions heterogeneous system and the corresponding reaction constants were listed in Table 16.

**Table 16.** The reactions and the reaction constants in nickel ions heterogeneous system.

| Reactions | Reaction Constants | |
|---|---|---|
| $Ni(OH)_{2(s)} \rightleftharpoons \mathrm{Ni}^{2+} + 2OH^-$ | $K_{Nis0} = 10^{-15.26}$ | (92) |
| $Ni(OH)_{2(s)} \rightleftharpoons Ni(OH)^+ + OH^-$ | $K_{Nis1} = \beta_{Ni1}K_{Nis0}$ | (93) |
| $Ni(OH)_{2(s)} \rightleftharpoons Ni(OH)_{2(aq)}$ | $K_{Nis2} = \beta_{Ni2}K_{Nis0}$ | (94) |
| $Ni(OH)_{2(s)} + OH^- \rightleftharpoons Ni(OH)_3^-$ | $K_{Nis3} = \beta_{Ni3}K_{Nis0}$ | (95) |

The calculation formulas for the concentration of each component in the nickel ions heterogeneous system are as follows:

$$[Ni^{2+}] = K_{Nis0}/[OH^-]^2 \quad (96)$$

$$[Ni(OH)^+] = K_{Nis1}/[OH^-] \quad (97)$$

$$[Ni(OH)_{2(aq)}] = K_{Nis2} \quad (98)$$

$$[\mathrm{Ni}(OH)_3^-] = K_{Nis3}[OH^-] \quad (99)$$

$$\left[Ni(OH)_{2(s)}\right] = C_{Ni} - [Ni^{2+}] - [Ni(OH)^+] - \left[Ni(OH)_{2(aq)}\right] - [\mathrm{Ni}(OH)_3^-] \quad (100)$$

Based on the formulars, the species distribution of 2.61 × $10^{-5}$ mol/L nickel ions were calculated, as shown in Fig. 46.

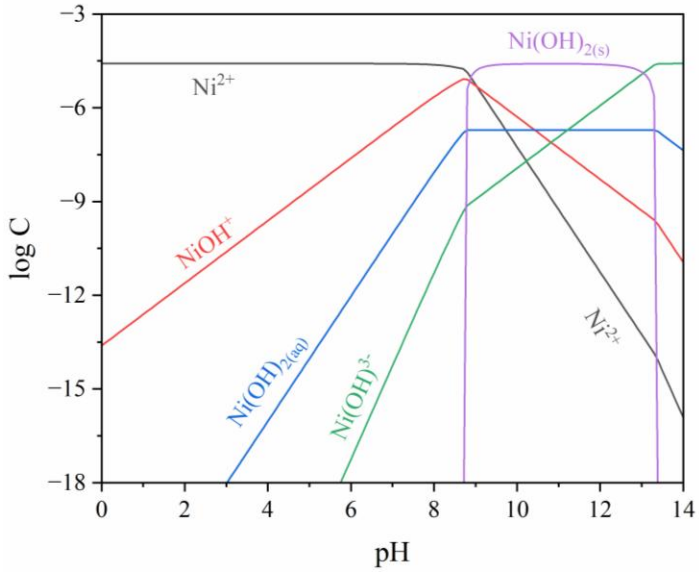


**Fig. 46.** Species distribution diagram of 2.61 × $10^{-5}$ mol/L nickel ions.

As shown in Fig. 46, at low pH values (below pH 4), the predominant species is $Ni^{2+}$. As pH increases, nickel undergoes hydrolysis, and the species $NiOH^+$ becomes more prevalent between pH 4 and 8. Around pH 8.7, $Ni(OH)_{2(s)}$, the solid form of nickel hydroxide, starts to precipitate, indicating solubility limits. Above pH 8, soluble species such as $Ni(OH)_{2(aq)}$ and $Ni(OH)_3^-$ become more significant. In strongly basic solutions (pH above 12), $Ni(OH)_3^-$ becomes the dominant species.

The initial concentration of zinc ions is 1.36 × $10^{-4}$ mol/L. The reactions in zinc ions homogeneous system and the corresponding reaction constants were listed in Table 17.

**Table 17.** The reactions and the reaction constants in zinc ions homogeneous system.

| Reactions | Reaction Constants | |
|---|---|---|
| $Zn^{2+} + OH^- \rightleftharpoons ZnOH^+$ | $\beta_{Zn1} = 10^{4.40}$ | (101) |
| $Zn^{2+} + 2OH^- \rightleftharpoons Zn(OH)_{2(aq)}$ | $\beta_{Zn2} = 10^{11.30}$ | (102) |
| $Zn^{2+} + 3OH^- \rightleftharpoons Zn(OH)_3^-$ | $\beta_{Zn3} = 10^{14.14}$ | (103) |
| $Zn^{2+} + 4OH^- \rightleftharpoons Zn(OH)_4^{2-}$ | $\beta_{Zn3} = 10^{17.66}$ | (104) |

The calculation formulas for the concentration of each component in the zinc ion homogeneous system are as follows:

$$\alpha_{Zn^{2+}} = 1 + \beta_{Zn1}[OH^-] + \beta_{Zn2}[OH^-]^2 + \beta_{Zn3}[OH^-]^3 + \beta_{Zn4}[OH^-]^4 \quad (105)$$

$$[Zn^{2+}] = C_{Zn}/\alpha_{Zn^{2+}} \quad (106)$$

$$[ZnOH^+] = [Zn^{2+}]\beta_{Zn1}[OH^-] \quad (107)$$

$$[Zn(OH)_{2(aq)}] = [Zn^{2+}]\beta_{Zn2}[OH^-]^2 \quad (108)$$

$$[Zn(OH)_3^-] = [Zn^{2+}]\beta_{Zn3}[OH^-]^3 \quad (109)$$

$$[Zn(OH)_4^-] = [Zn^{2+}]\beta_{Zn4}[OH^-]^4 \quad (110)$$

where $C_{Zn}$ is the total concentration of zinc ions, and $\alpha_{Zn^{2+}}$ is the side reaction coefficient.

The reactions in zinc ions heterogeneous system and the corresponding reaction constants were listed in Table 18.

**Table 18.** The reactions and the reaction constants in zinc ions heterogeneous system.

| Reactions | Reaction Constants | |
|---|---|---|
| $Zn(OH)_{2(s)} \rightleftharpoons \mathrm{Zn}^{2+} + 2OH^-$ | $K_{Zns0} = 10^{-16.5}$ | (111) |
| $Zn(OH)_{2(s)} \rightleftharpoons Zn(OH)^+ + OH^-$ | $K_{Zns1} = \beta_{Zn1}K_{Zns0}$ | (112) |
| $Zn(OH)_{2(s)} \rightleftharpoons Zn(OH)_{2(aq)}$ | $K_{Zns2} = \beta_{Zn2}K_{Zns0}$ | (113) |
| $Zn(OH)_{2(s)} + OH^- \rightleftharpoons Zn(OH)_3^-$ | $K_{Zns3} = \beta_{Zn3}K_{Zns0}$ | (114) |
| $Zn(OH)_{2(s)} + 2OH^- \rightleftharpoons Zn(OH)_4^{2-}$ | $K_{Zns4} = \beta_{Zn4}K_{Zns0}$ | (115) |

The calculation formulas for the concentration of each component in the zinc ions heterogeneous system are as follows:

$$[Zn^{2+}] = K_{Zns0}/[OH^-]^2 \quad (116)$$

$$[ZnOH^+] = K_{Zns1}/[OH^-] \quad (117)$$

$$[Zn(OH)_{2(aq)}] = K_{Zns2} \quad (118)$$

$$[Zn(OH)_3^-] = K_{Zns3}[OH^-] \quad (119)$$

$$[Zn(OH)_4^-] = K_{Zns4}[OH^-]^2 \quad (120)$$

$$\left[Zn(OH)_{2(s)}\right] = C_{Zn} - [Zn^{2+}] - [ZnOH^+] - \left[Zn(OH)_{2(aq)}\right] - [Zn(OH)_3^-] - [Zn(OH)_4^-] \quad (121)$$

Based on the formulars, the species distribution of $1.36 \times 10^{-4}$ mol/L zinc ions were calculated, as shown in Fig. 47.

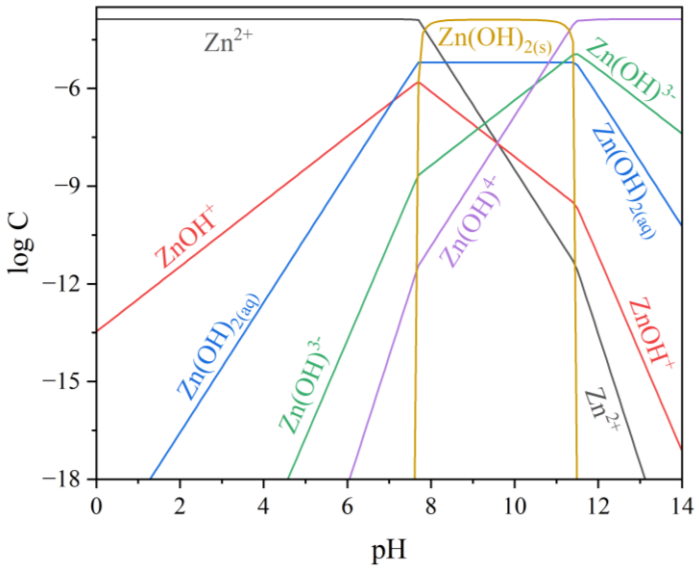


**Fig. 47.** Species distribution diagram of $1.36 \times 10^{-4}$ mol/L zinc ions.

As shown in Fig. 47, At low pH (below pH 6), the dominant species is $Zn^{2+}$, indicating that zinc remains in its ionic form in strongly acidic conditions. As the pH increases, $ZnOH^{+}$ appeared, which is prominent between pH 6 and 8. Around pH 7.7, solid zinc hydroxide $Zn(OH)_{2(s)}$ begins to precipitate, marking the solubility threshold of zinc hydroxide. Above pH 7.7, soluble species like $Zn(OH)_{2(aq)}$ and $Zn(OH)_3^-$ become important, with $Zn(OH)_4^{2-}$ appearing in more basic solutions (pH above 11).

The reactions in cadmium ions homogeneous system and the corresponding reaction constants were listed in Table 19. The initial concentration of cadmium ions is $2.49 \times 10^{-6}$ mol/L.

**Table 19.** The reactions and the reaction constants in cadmium ions homogeneous system.

| Reactions | Reaction Constants | |
|---|---|---|
| $Cd^{2+} + OH^- \rightleftharpoons CdOH^+$ | $\beta_{Cd1} = 10^{4.17}$ | (122) |
| $Cd^{2+} + 2OH^- \rightleftharpoons Cd(OH)_{2(aq)}$ | $\beta_{Cd2} = 10^{8.33}$ | (123) |
| $Cd^{2+} + 3OH^- \rightleftharpoons Cd(OH)_3^-$ | $\beta_{Cd3} = 10^{9.02}$ | (124) |
| $Cd^{2+} + 4OH^- \rightleftharpoons Cd(OH)_4^{2-}$ | $\beta_{Cd3} = 10^{8.62}$ | (125) |

where β is the reaction constant.

The calculation formulas for the concentration of each component in the cadmium ion homogeneous system are as follows:

$$\alpha_{Cd^{2+}} = 1 + \beta_{Cd1}[OH^-] + \beta_{Cd2}[OH^-]^2 + \beta_{Cd3}[OH^-]^3 + \beta_{Cd4}[OH^-]^4 \quad (126)$$

$$[Cd^{2+}] = C_{Cd}/\alpha_{Cd^{2+}} \quad (127)$$

$$[CdOH^{+}] = [Cd^{2+}]\beta_{Cd1}[OH^{-}] \quad (128)$$

$$[Cd(OH)_{2(aq)}] = [Cd^{2+}]\beta_{Cd2}[OH^{-}]^2 \quad (129)$$

$$[Cd(OH)_3^-] = [Cd^{2+}]\beta_{Cd3}[OH^{-}]^3 \quad (130)$$

$$[Cd(OH)_4^-] = [Cd^{2+}]\beta_{Cd4}[OH^{-}]^4 \quad (131)$$

where $C_{Cd}$ is the total concentration of cadmium ions, and $\alpha_{Cd^{2+}}$ is the side reaction coefficient.

The reactions in cadmium ions heterogeneous system and the corresponding reaction constants were listed in Table 20.

**Table 20.** The reactions and the reaction constants in cadmium ions heterogeneous system.

| Reactions | Reaction Constants | |
|---|---|---|
| $Cd(OH)_{2(s)} \rightleftharpoons Cd^{2+} + 2OH^-$ | $K_{Cds0} = 10^{-14.14}$ | (132) |
| $Cd(OH)_{2(s)} \rightleftharpoons Cd(OH)^+ + OH^-$ | $K_{Cds1} = \beta_{Cd1}K_{Cds0}$ | (133) |
| $Cd(OH)_{2(s)} \rightleftharpoons Cd(OH)_{2(aq)}$ | $K_{Cds2} = \beta_{Cd2}K_{Cds0}$ | (134) |
| $Cd(OH)_{2(s)} + OH^- \rightleftharpoons Cd(OH)_3^-$ | $K_{Cds3} = \beta_{Cd3}K_{Cds0}$ | (135) |
| $Cd(OH)_{2(s)} + 2OH^- \rightleftharpoons Cd(OH)_4^{2-}$ | $K_{Cds4} = \beta_{Cd4}K_{Cds0}$ | (136) |

The calculation formulas for the concentration of each component in the cadmium ions heterogeneous system are as follows:

$$[Cd^{2+}] = K_{Cds0}/[OH^{-}]^2 \quad (137)$$

$$[CdOH^{+}] = K_{Cds1}/[OH^{-}] \quad (138)$$

$$[Cd(OH)_{2(aq)}] = K_{Cds2} \quad (139)$$

$$[Cd(OH)_3^-] = K_{Cds3}[OH^{-}] \quad (140)$$

$$[Cd(OH)_4^-] = K_{Cds4}[OH^{-}]^2 \quad (141)$$

$$\left[Cd(OH)_{2(s)}\right] = C_{Cd} - [Cd^{2+}] - [CdOH^{+}] - \left[Cd(OH)_{2(aq)}\right] - [Cd(OH)_3^-] - [Cd(OH)_4^-] \quad (142)$$

Based on the formulars, the species distribution of 2.49 × $10^{-6}$ mol/L cadmium ions were calculated, as shown in Fig. 48.

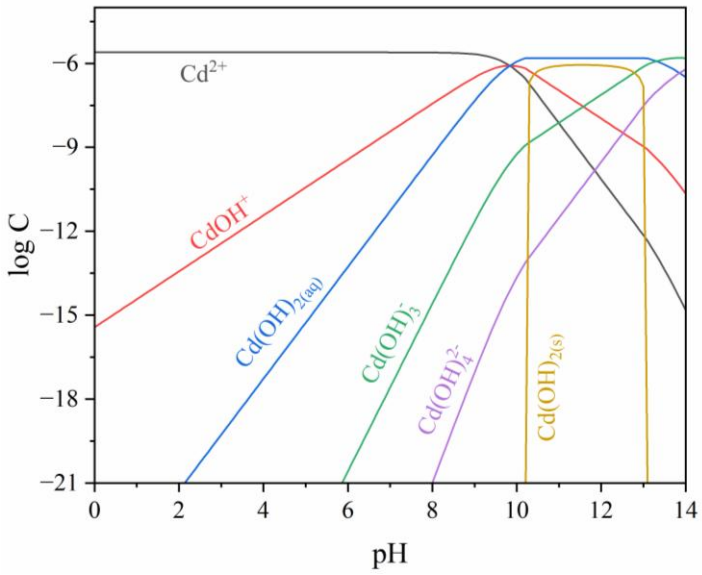


**Fig. 48.** Species distribution diagram of $2.49 \times 10^{-6}$ mol/L cadmium ions.

As shown in Fig. 48, at low pH values (below pH 7), the predominant species is $Cd^{2+}$, with $CdOH^+$ emerging as pH increases. Between pH 8 and 10, soluble hydroxo complexes like $Cd(OH)_{2(aq)}$ and $Cd(OH)_3^-$ are prevalent. Around pH 10.2, $Cd(OH)_{2(s)}$, the solid form of cadmium hydroxide, starts to precipitate, indicating solubility limits.

The initial concentration of magnesium ions is $4.10 \times 10^{-3}$ mol/L. The reactions in magnesium ions homogeneous system and the corresponding reaction constants were listed in Table 21. Magnesium

**Table 21.** The reactions and the reaction constants in magnesium ions homogeneous system.

| Reactions | Reaction Constants | |
|---|---|---|
| $Mg^{2+} + OH^- \rightleftharpoons MgOH^+$ | $\beta_{Mg1} = 10^{2.58}$ | (143) |
| $Mg^{2+} + 2OH^- \rightleftharpoons Mg(OH)_{2(aq)}$ | $\beta_{Mg2} = 10^{5.81}$ | (144) |

The calculation formulas for the concentration of each component in the magnesium ion homogeneous system are as follows:

$$\alpha_{Mg^{2+}} = 1 + \beta_{Mg1}[OH^-] + \beta_{Mg2}[OH^-]^2 \quad (145)$$

$$[Mg^{2+}] = C_{Mg}/\alpha_{Mg^{2+}} \quad (146)$$

$$[MgOH^+] = [Mg^{2+}]\beta_{Mg1}[OH^-] \quad (147)$$

$$[Mg(OH)_{2(aq)}] = [Mg^{2+}]\beta_{Mg2}[OH^-]^2 \quad (148)$$

where $C_{Mg}$ is the total concentration of magnesium ions, and $\alpha_{Mg^{2+}}$ is the side reaction coefficient.

The reactions in magnesium ions heterogeneous system and the corresponding reaction constants were listed in Table 22.

**Table 22.** The reactions and the reaction constants in magnesium ions heterogeneous system.

| Reactions | Reaction Constants | |
|---|---|---|
| $Mg(OH)_{2(s)} \rightleftharpoons Mg^{2+} + 2OH^-$ | $K_{Mgs0} = 10^{-11.25}$ | (149) |
| $Mg(OH)_{2(s)} \rightleftharpoons Mg(OH)^+ + OH^-$ | $K_{Mgs1} = \beta_{Mg1} K_{Mgs0}$ | (150) |
| $Mg(OH)_{2(s)} \rightleftharpoons Mg(OH)_{2(aq)}$ | $K_{Mgs2} = \beta_{Mg2} K_{Mgs0}$ | (151) |

The calculation formulas for the concentration of each component in the magnesium ions heterogeneous system are as follows:

$$[Mg^{2+}] = K_{Mgs0}/[OH^-]^2 \quad (152)$$

$$[Mg(OH)^+] = K_{Mgs1}/[OH^-] \quad (153)$$

$$[Mg(OH)_{2(aq)}] = K_{Mgs2} \quad (154)$$

$$[Mg(OH)_{2(s)}] = C_{Mg} - [Mg^{2+}] - [Mg(OH)^+] - [Mg(OH)_{2(aq)}] \quad (155)$$

Based on the formulars, the species distribution of 4.10 × $10^{-3}$ mol/L magnesium ions were calculated, as shown in Fig. 49.

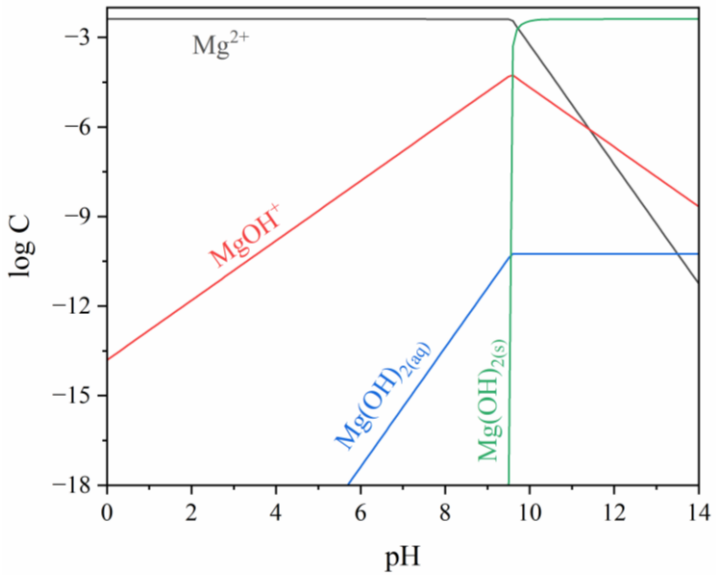

**Fig. 49.** Species distribution diagram of $4.10 \times 10^{-3}$ mol/L magnesium ions.

As shown in Fig. 49, At low pH (below pH 6), the dominant species is $Mg^{2+}$, indicating that magnesium remains in its ionic form in strongly acidic conditions. As the pH increases, $MgOH^{+}$ appears. Around pH 9.4, solid magnesium hydroxide $Mg(OH)_{2(s)}$ begins to precipitate, marking the solubility threshold of magnesium hydroxide. Above pH 7.7, soluble species like $Mg(OH)_{2(aq)}$ and $Mg(OH)_3^-$ become important, with $Mg(OH)_4^{2-}$ appearing in more basic solutions (pH above 11).

Due to the indeterminate valence state of tin, species distribution diagrams of both $Sn^{2+}$ and $Sn^{4+}$ are calculated. The reactions in $Sn^{2+}$ homogeneous system and the corresponding reaction constants were listed in Table 23. The initial concentration of $Sn^{2+}$ is $2.27 \times 10^{-6}$ mol/L.

**Table 23.** The reactions and the reaction constants in $Sn^{2+}$ homogeneous system.

| Reactions | Reaction Constants | |
|---|---|---|
| $Sn^{2+} + OH^- \rightleftharpoons SnOH^+$ | $\beta_{Sn21} = 10^{10.63}$ | (156) |
| $Sn^{2+} + 2OH^- \rightleftharpoons Sn(OH)_{2(aq)}$ | $\beta_{Sn22} = 10^{20.99}$ | (157) |
| $Sn^{2+} + 3OH^- \rightleftharpoons Sn(OH)_3^-$ | $\beta_{Sn23} = 10^{25.43}$ | (158) |

where β is the reaction constant.

The calculation formulas for the concentration of each component in the $Sn^{2+}$ homogeneous system are as follows:

$$\alpha_{Sn^{2+}} = 1 + \beta_{Sn21}[OH^-] + \beta_{Sn22}[OH^-]^2 + \beta_{Sn23}[OH^-]^3 + \beta_{Sn24}[OH^-]^4 \quad (159)$$

$$[Sn^{2+}] = C_{Sn2}/\alpha_{Sn^{2+}} \quad (160)$$

$$[SnOH^+] = [Sn^{2+}]\beta_{Sn21}[OH^-] \quad (161)$$

$$[Sn(OH)_{2(aq)}] = [Sn^{2+}]\beta_{Sn22}[OH^-]^2 \quad (162)$$

$$[Sn(OH)_3^-] = [Sn^{2+}]\beta_{Sn23}[OH^-]^3 \quad (163)$$

where $C_{Sn2}$ is the total concentration of $Sn^{2+}$, and $\alpha_{Sn^{2+}}$ is the side reaction coefficient.

The reactions in $Sn^{2+}$ heterogeneous system and the corresponding reaction constants were listed in Table 24.

**Table 24.** The reactions and the reaction constants in $Sn^{2+}$ heterogeneous system.

| Reactions | Reaction Constants | |
|---|---|---|
| $Sn(OH)_{2(s)} \rightleftharpoons Sn^{2+} + 2OH^-$ | $K_{Sn2s0} = 10^{-27.26}$ | (164) |

| | | |
|---|---|---|
| $Sn(OH)_{2(s)} \rightleftharpoons Sn(OH)^+ + OH^-$ | $K_{Sn2s1} = \beta_{Sn21} K_{Sn2s0}$ | (165) |
| $Sn(OH)_{2(s)} \rightleftharpoons Sn(OH)_{2(aq)}$ | $K_{Sn2s2} = \beta_{Sn22} K_{Sn2s0}$ | (166) |
| $Sn(OH)_{2(s)} + OH^- \rightleftharpoons Sn(OH)_3^-$ | $K_{Sn2s3} = \beta_{Sn23} K_{Sn2s0}$ | (167) |

The calculation formulas for the concentration of each component in the $Sn^{2+}$ heterogeneous system are as follows:

$$[Sn^{2+}] = K_{Sn2s0}/[OH^-]^2 \quad (168)$$

$$[Sn(OH)^+] = K_{Sn2s1}/[OH^-] \quad (169)$$

$$[Sn(OH)_{2(aq)}] = K_{Sn2s2} \quad (170)$$

$$[Sn(OH)_3^-] = K_{Sn2s3}[OH^-] \quad (171)$$

$$[Sn(OH)_{2(s)}] = C_{Sn} - [Sn^{2+}] - [Sn(OH)^+] - [Sn(OH)_{2(aq)}] - [Sn(OH)_3^-] \quad (172)$$

Based on the formulars, the species distribution of 2.27 × $10^{-6}$ mol/L $Sn^{2+}$ were calculated, as shown in Fig. 50.

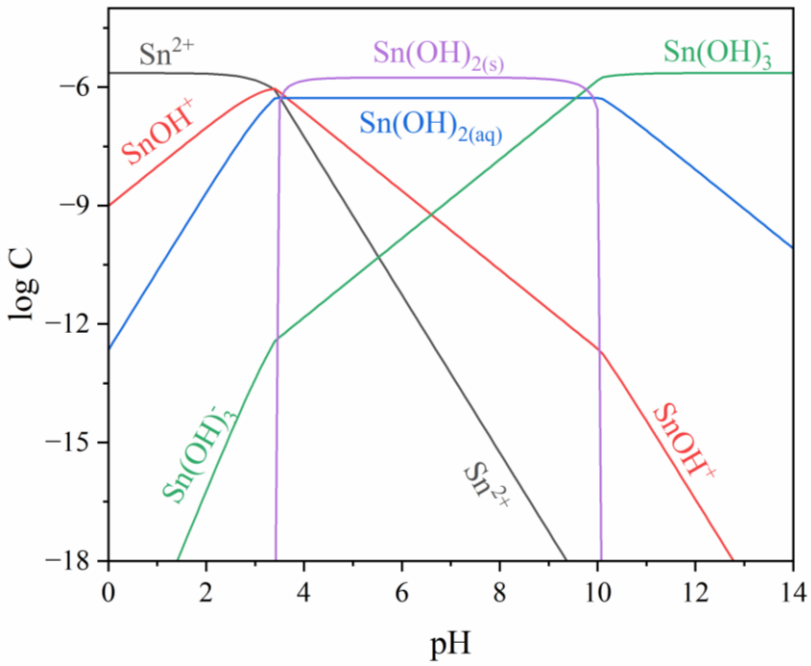


**Fig. 50.** Species distribution diagram of 2.27 × $10^{-6}$ mol/L $Sn^{2+}$.

As shown in Fig. 50, at low pH values (below pH 3.4), the predominant species is $Sn^{2+}$, with $SnOH^+$ emerging as pH increases. At pH 3.5, the solid form of $Sn(OH)_{2(s)}$ starts to precipitate and remains stable until pH 10.1. Above pH 10.1, soluble species like $Sn(OH)_{2(aq)}$ and $Sn(OH)_3^-$ become important, leading to a redissolution of $Sn(OH)_{2(s)}$ precipitates.

Fixing the initial concentration of tin ions $2.27 \times 10^{-6}$ mol/L, the species distribution diagram of $Sn^{4+}$ ions was also calculated. The reactions in $Sn^{4+}$ homogeneous system and the corresponding reaction constants were listed in Table 25.

**Table 25.** The reactions and the reaction constants in $Sn^{4+}$ homogeneous system.

| Reactions | Reaction Constants | |
|---|---|---|
| $Sn^{4+} + OH^- \rightleftharpoons SnOH^{3+}$ | $\beta_{Sn41} = 10^{14.61}$ | (173) |
| $Sn^{4+} + 2OH^- \rightleftharpoons Sn(OH)_2^{2+}$ | $\beta_{Sn42} = 10^{27.80}$ | (174) |
| $Sn^{4+} + 3OH^- \rightleftharpoons Sn(OH)_3^+$ | $\beta_{Sn43} = 10^{42.47}$ | (175) |
| $Sn^{4+} + 3OH^- \rightleftharpoons Sn(OH)_{4(aq)}$ | $\beta_{Sn44} = 10^{56.79}$ | (176) |
| $Sn^{4+} + 3OH^- \rightleftharpoons Sn(OH)_5^-$ | $\beta_{Sn45} = 10^{59.58}$ | (177) |
| $Sn^{4+} + 3OH^- \rightleftharpoons Sn(OH)_6^{2-}$ | $\beta_{Sn46} = 10^{62.65}$ | (178) |

The calculation formulas for the concentration of each component in the $Sn^{4+}$ homogeneous system are as follows:

$$\alpha_{Sn^{4+}} = 1 + \beta_{Sn41}[OH^-] + \beta_{Sn42}[OH^-]^2 + \beta_{Sn43}[OH^-]^3 + \beta_{Sn44}[OH^-]^4 + \beta_{Sn45}[OH^-]^5 + \beta_{Sn46}[OH^-]^6 \quad (179)$$

$$[Sn^{4+}] = C_{Sn4}/\alpha_{Sn^{4+}} \quad (180)$$

$$[Sn(OH)^{3+}] = [Sn^{4+}]\beta_{Sn41}[OH^-] \quad (181)$$

$$[Sn(OH)_2^{2+}] = [Sn^{4+}]\beta_{Sn42}[OH^-]^2 \quad (182)$$

where $C_{Sn4}$ is the total concentration of $Sn^{4+}$, and $\alpha_{Sn^{4+}}$ is the side reaction coefficient.

The reactions in $Sn^{4+}$ heterogeneous system and the corresponding reaction constants were listed in Table 26.

**Table 26.** The reactions and the reaction constants in $Sn^{4+}$ heterogeneous system.

| Reactions | Reaction Constants | |
|---|---|---|
| $Sn(OH)_{4(s)} \rightleftharpoons Sn^{4+} + 4OH^-$ | $K_{Sn4s0} = 10^{-56}$ | (183) |
| $Sn(OH)_{4(s)} \rightleftharpoons SnOH^{3+} + 3OH^-$ | $K_{Sn4s1} = \beta_{Sn41}K_{Sn4s0}$ | (184) |
| $Sn(OH)_{4(s)} \rightleftharpoons Sn(OH)_2^{2+} + 2OH^-$ | $K_{Sn4s2} = \beta_{Sn42}K_{Sn4s0}$ | (185) |
| $Sn(OH)_{4(s)} \rightleftharpoons Sn(OH)_3^+ + OH^-$ | $K_{Sn4s3} = \beta_{Sn43}K_{Sn4s0}$ | (186) |
| $Sn(OH)_{4(s)} \rightleftharpoons Sn(OH)_{4(aq)}$ | $K_{Sn4s4} = \beta_{Sn44}K_{Sn4s0}$ | (187) |
| $Sn(OH)_{4(s)} + OH^- \rightleftharpoons Sn(OH)_5^-$ | $K_{Sn4s5} = \beta_{Sn45}K_{Sn4s0}$ | (188) |
| $Sn(OH)_{4(s)} + 2OH^- \rightleftharpoons Sn(OH)_6^{2-}$ | $K_{Sn4s6} = \beta_{Sn46}K_{Sn4s0}$ | (189) |

The calculation formulas for the concentration of each component in the $Sn^{4+}$ heterogeneous system are as follows:

$$[Sn^{4+}] = K_{Sn4s0}/[OH^-]^4 \quad (190)$$

$$[Sn(OH)^{3+}] = K_{Sn4s1}/[OH^-]^3 \quad (191)$$

$$[Sn(OH)_2^{2+}] = K_{Sn4s2}/[OH^-]^2 \quad (192)$$

$$[Sn(OH)_3^{+}] = K_{Sn4s3}/[OH^-] \quad (193)$$

$$[Sn(OH)_{4(aq)}] = K_{Sn4s4} \quad (194)$$

$$[Sn(OH)_5^-] = K_{Sn4s5}[OH^-] \quad (195)$$

$$[Sn(OH)_6^{2-}] = K_{Sn4s6}[OH^-]^2 \quad (196)$$

$$[Sn(OH)_{4(s)}] = C_{Sn4} - [Sn^{4+}] - [Sn(OH)^{3+}] - [Sn(OH)_2^{2+}] - [Sn(OH)_3^{+}] - [Sn(OH)_{4(aq)}] - [Sn(OH)_5^-] - [Sn(OH)_6^{2-}] \quad (197)$$

Based on the formulars, the species distribution of 2.27 × $10^{-6}$ mol/L $Sn^{4+}$ was calculated, as shown in Fig. 51.

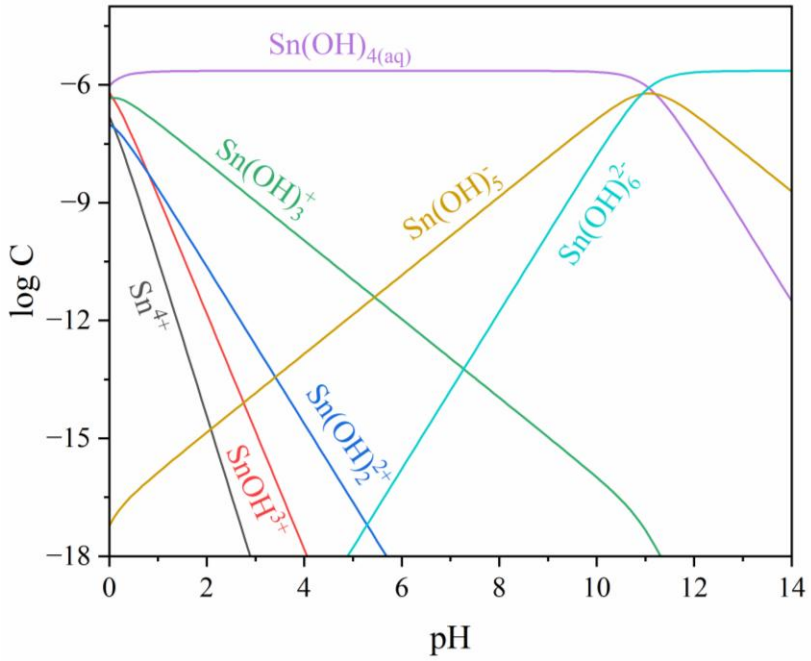


**Fig. 51.** Species distribution diagram of 4.10 × $10^{-3}$ mol/L $Sn^{4+}$.

As shown in Fig. 51, at low pH (0–2), Sn exists mainly as free $Sn^{4+}$ and $SnOH^{3+}$. Between pH 2–6, $Sn(OH)_3^+$ and $Sn(OH)_2^{2+}$ dominate, with $Sn(OH)_{4(aq)}$ becoming the major species across a wide pH range from ~4 to 11. At higher pH (>11), $Sn(OH)_5^-$ and $Sn(OH)_6^{2-}$ become predominant,

indicating increasing deprotonation. Overall, $Sn(OH)_{4(aq)}$ is the most stable and abundant species across the mid-pH range, while more charged hydroxyl complexes form under alkaline conditions.

Therefore, if the valence state of tin is 4+, no hydroxide precipitation will form at the given initial concentration; conversely, if it is 2+, the $Sn(OH)_2$ precipitate remains stable within the pH range of 3.4 to 10.1. In the precipitation experiments (Task 2.0), a significant decrease in Sn ion concentration was observed, indicating the formation of a solid precipitate. This suggests that Sn in AMD primarily exists in the $Sn^{2+}$ state and precipitates as $Sn(OH)_2$ within the pH range of 3.4–10.1.

The species distribution diagrams of $Ca^{2+}$ is calculated. The reactions in $Ca^{2+}$ homogeneous system and the corresponding reaction constants were listed in Table 27. The initial concentration of $Ca^{2+}$ is $7.92 \times 10^{-3}$ mol/L.

**Table 27.** The reactions and the reaction constants in $Ca^{2+}$ homogeneous system.

| Reactions | Reaction Constants | |
|---|---|---|
| $Ca^{2+} + OH^- \rightleftharpoons CaOH^+$ | $\beta_{Ca1} = 10^{1.4}$ | (198) |
| $Ca^{2+} + 2OH^- \rightleftharpoons Ca(OH)_{2(aq)}$ | $\beta_{Ca2} = 10^{2.77}$ | (199) |

where β is the reaction constant.

The calculation formulas for the concentration of each component in the $Ca^{2+}$ homogeneous system are as follows:

$$\alpha_{Ca^{2+}} = 1 + \beta_{Ca1}[OH^-] + \beta_{Ca2}[OH^-]^2 \quad (200)$$

$$[Ca^{2+}] = C_{Ca}/\alpha_{Ca^{2+}} \quad (201)$$

$$[CaOH^+] = [Ca^{2+}]\beta_{Ca1}[OH^-] \quad (202)$$

$$[Ca(OH)_{2(aq)}] = [Ca^{2+}]\beta_{Ca2}[OH^-]^2 \quad (203)$$

where $C_{Ca2}$ is the total concentration of $Ca^{2+}$, and $\alpha_{Ca^{2+}}$ is the side reaction coefficient.

The reactions in $Ca^{2+}$ heterogeneous system and the corresponding reaction constants were listed in Table 28.

**Table 28.** The reactions and the reaction constants in $Ca^{2+}$ heterogeneous system.

| Reactions | Reaction Constants | |
|---|---|---|
| $Ca(OH)_{2(s)} \rightleftharpoons Ca^{2+} + 2OH^-$ | $K_{Cas0} = 10^{-5.26}$ | (204) |
| $Ca(OH)_{2(s)} \rightleftharpoons Ca(OH)^+ + OH^-$ | $K_{Cas1} = \beta_{Ca1}K_{Cas0}$ | (205) |

$$Ca(OH)_{2(s)} \rightleftharpoons Ca(OH)_{2(aq)} \qquad K_{Cas2} = \beta_{Ca2} K_{Cas0} \qquad (206)$$

The calculation formulas for the concentration of each component in the calcium ions heterogeneous system are as follows:

$$[Ca^{2+}] = K_{Cas0}/[OH^-]^2 \qquad (207)$$

$$[CaOH^+] = K_{Cas1}/[OH^-] \qquad (208)$$

$$[Ca(OH)_{2(aq)}] = K_{Cas2} \qquad (209)$$

$$[Ca(OH)_{2(s)}] = C_{Ca} - [Ca^{2+}] - [CaOH^+] - [Ca(OH)_{2(aq)}] \qquad (210)$$

Based on the formulars, the species distribution of 7.92 × $10^{-3}$ mol/L $Ca^{2+}$ was calculated, as shown in Fig. 52.

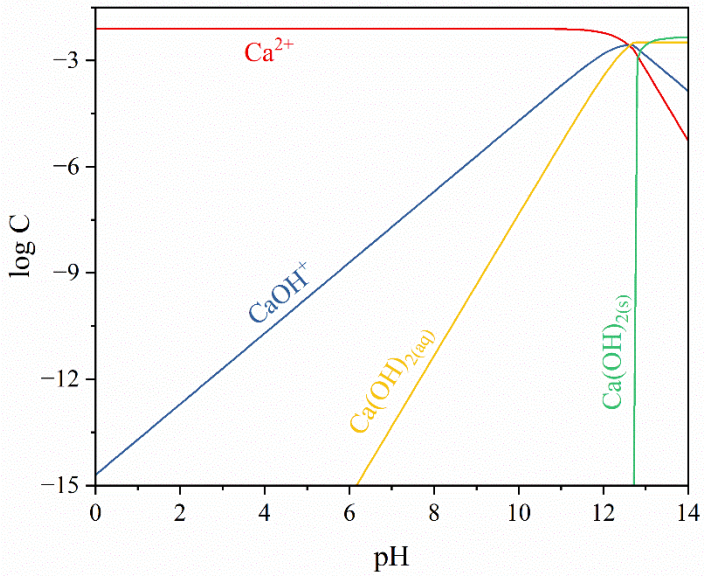


**Fig. 52.** Species distribution diagram of 7.92 × $10^{-3}$ mol/L $Ca^{2+}$.

As shown in Fig. 52, at low pH (acidic conditions), $Ca^{2+}$ is the dominant species. As the pH increases, $Ca^{2+}$ gradually hydrolyzes, forming $CaOH^+$ and $Ca(OH)_{2(aq)}$. At pH 12.8, $Ca(OH)_{2(s)}$ begins to precipitate and remain stable till pH 14.0. Therefore, no $Ca(OH)_{2(s)}$ precipitation would form within the experimental pH range (3.0-11.5).

According to all the species distribution diagrams, the theoretical order of pH for precipitating these metal ions in AMD from low to high is: $Fe^{3+}$, $Sn^{2+}$, $Al^{3+}$, $Co^{2+}$, $Zn^{2+}$, $Ni^{2+}$, $Mn^{2+}$, $Mg^{2+}$, $Cd^{2+}$, $Ca^{2+}$. Experimental results from precipitation studies are largely consistent with this theoretical sequence. However, the pH for the precipitation of the remaining ions, except for iron and

aluminum, is lower than the theoretical value. This discrepancy may be attributed to the initially produced $Al(OH)_3$ providing nucleation sites for the precipitation of subsequent ions, thereby reducing the nucleation energy and consequently lowering the pH at which they form precipitates.

*II. Characterizations of sludge precipitate particles*

During the flotation process, the collision and adhesion of particles and bubbles are key factors that determine flotation efficiency. Collision probability refers to the probability of mineral particles colliding with bubbles in the flotation tank. The probability of collision is affected by many factors. Usually, the smaller the mineral particles, the smaller the chance of contact between particles and bubbles, and the lower probability of collision. By adding flocculant, the mineral particles can be flocculated, and the apparent size of the mineral particles can be increased, thereby increasing the probability of collision. The adhesion probability is the probability of adhesion between mineral particles and bubbles after collision. The adhesion probability depends on the physical and chemical properties of the particle surface. During the flotation process, flotation agents are often added to change the hydrophilicity and hydrophobicity of the mineral surface to increase the adhesion probability. It is difficult for small mineral particles to overcome the resistance of the hydration layer between the mineral particles and bubbles when they collide, making it difficult for them to adhere to the bubbles. If the particles are too coarse, they will exceed the floating ability of the bubbles. Therefore, flotation efficiency is closely related to mineral particle size.

To evaluate the flotation property of precipitate particles, the particle size was tested, shown in Fig. 53. The median diameter ($D_{50}$) of the precipitate particles is 5.7 μm, and the 90th percentile diameter ($D_{90}$) is 13.64 μm, according to Fig. 53. The particle diameter of precipitation is too small (<20 μm), making it difficult for them to attach to flotation bubbles if direct flotation is performed, resulting in a low precipitation recovery. Therefore, it is necessary to add flotation reagents to aggregate the particles into appropriately sized agglomerates, enhancing flotation performance and increasing the recovery of metal ions.

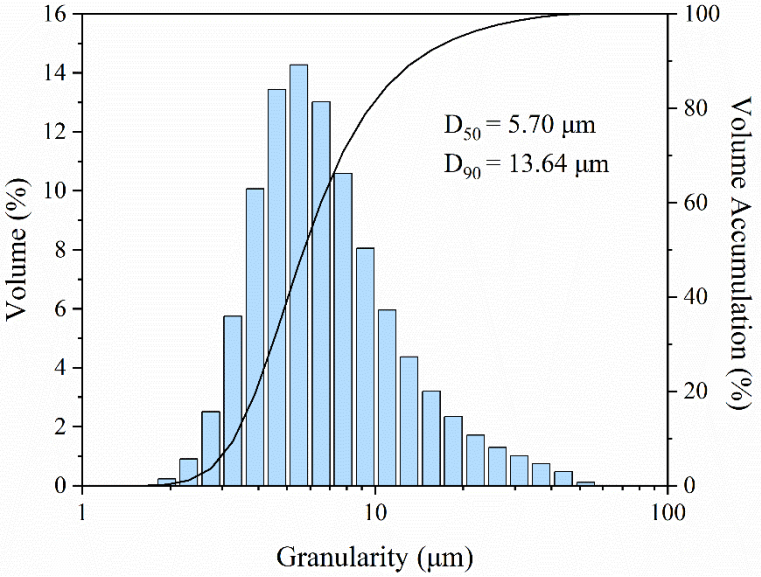


**Fig. 53.** Particle size of the sludge precipitation.

The flocculant is introduced to increase the apparent size of the mineral particles, thereby enhancing the collision probability between particles and bubbles. After adding flocculant to the slurry, the particle size was characterized, shown in Fig. 54. The median diameter ($D_{50}$) of the precipitate particles is 24.01 μm, and the 90th percentile diameter ($D_{90}$) is 46.88 μm. The $D_{50}$ and $D_{90}$ of particles after adding flocculant has a significantly increase compared to precipitation, indicating that the apparent size of the particles greatly expanded. Thus, the probability of collision between particles and bubbles is significantly optimized. Additionally, the size of the particles falls in the regular flotation range after introducing flocculant.

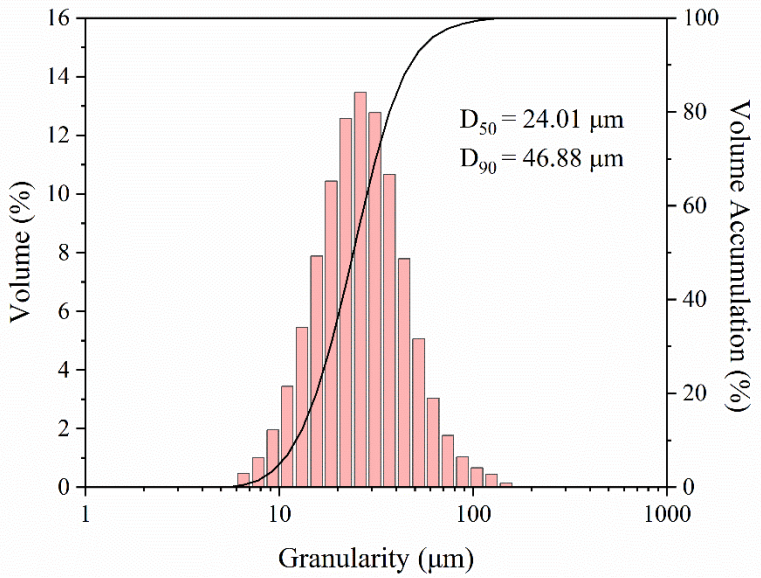

**Fig. 54.** Particle size of the sludge precipitation after adding flocculant.

After adding the A-100 flocculant, NaOL was then introduced to adjust the chemical properties of the particle surface, resulting in the increasing adhesion probability between precipitation particles and micro air bubbles. The particle size was tested after adding A-100 and NaOL, as shown in Fig. 55. The $D_{50}$ and $D_{90}$ of particles further increased to 25.48 μm and 51.55 μm, respectively, indicating the adsorption of oleate on the particle surfaces. Therefore, the adhesion property of particles was optimized, thereby the flotation property of precipitates was successfully enhanced.

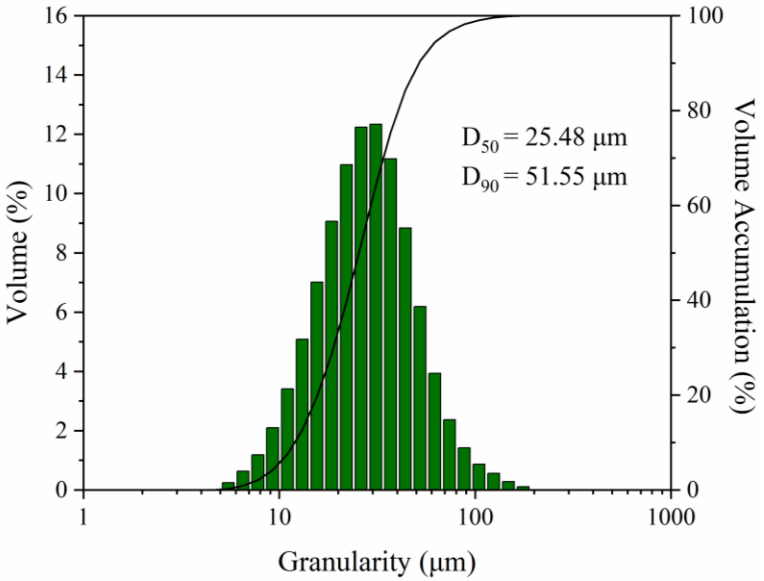


**Fig. 55.** Particle size of the sludge precipitation after adding flocculant and collector.

The appearance of the particles before and after adding reagents is observed under optical microscope. The appearance of precipitate particles is shown in Fig. 56, showing a relatively uniform, fine-grained structure without large visible clumps or aggregated particles. The precipitate particles appear well-dispersed, with minimal flocculation occurring. Fine particles with a diameter of less than 20 μm were observed, indicating challenges in collision between particles and adhesion between particles and air bubbles. The small particle size can also pose challenges in HDS circuit, due to their slow settling rates.

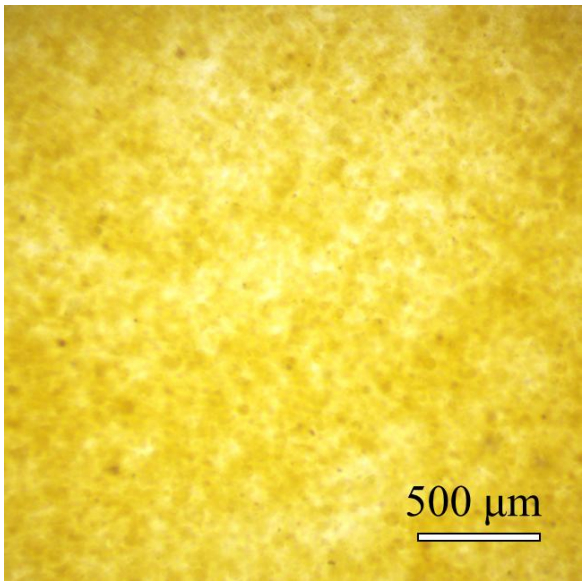


**Fig. 56.** The optical microscope image of the precipitates.

After introducing flocculant, the apparent size of the particles is significantly increased, as observed in Fig. 57. Flocculants are chemicals used to aggregate fine particles into larger flocs, facilitating the separation of solid particles from liquid phases. In this image, larger clusters of particles are observed, indicating successful flocculation. The particles are aggregated into larger flocs, resulting in a more distinguishable structure compared to Fig. 56. These flocs are significantly larger than the initial fine particles.

The addition of the flocculant has evidently induced aggregation, improving the likelihood of easier solid-liquid separation. The larger particle size aids in flotation or settling processes, making this step essential in both PFD and HDS processes.

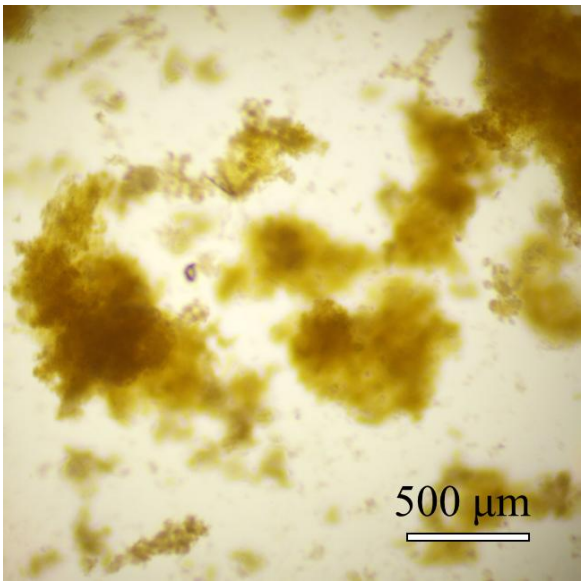


**Fig. 57.** The optical microscope image of the particles after adding flocculant.

Figure Fig**. 58** shows the result of adding both flocculant and collector. Collector is a reagent typically used to increase the hydrophobicity of certain particles, thereby promoting their attachment to bubbles in flotation processes.

The particle aggregates in Fig. 58 are even more pronounced and densely packed. The presence of both the flocculant and collector has enhanced the aggregation further, producing much larger and denser flocs compared to Fig. 57. This suggests that the synergistic effect of the flocculant and collector not only promotes aggregation but also modifies the surface properties of the precipitates. The dense clustering of particles would be beneficial in flotation processes where the goal is to separate hydrophobic particles from the aqueous phase. The larger floc size may improve the separation efficiency by making the aggregates more buoyant and easier to remove from the suspension.

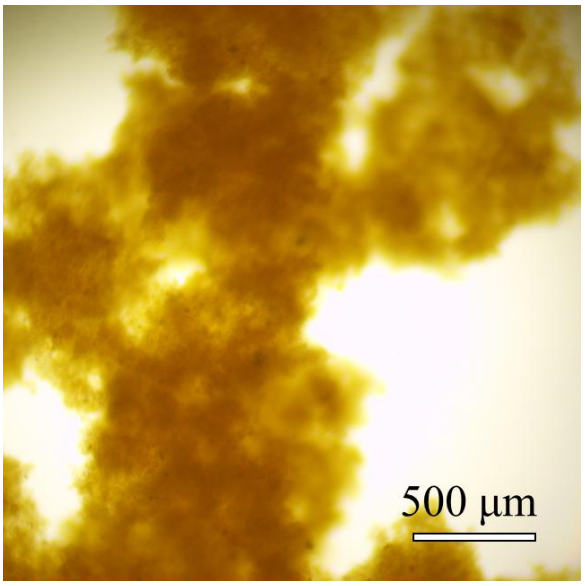


**Fig. 58.** The optical microscope image of the particles after adding flocculant and NaOL.

Overall, the images provided clearly demonstrate the impact of different additives on the behavior of precipitated particles. Without additives, the precipitate remains finely dispersed and difficult to separate. The addition of flocculants significantly enhances particle aggregation, improving separation processes. Finally, the combination of flocculants and collectors produces even larger and denser aggregates, ideal for flotation-based separations. These results are consistent with the measured particle sizes, which can be found in previous reports.

*III.Interactions of precipitate particles and flotation agents*

Zeta potential can display charge changes on particle surface and illustrate the adsorption of the agent on the precipitation surface. It helps understand and modify surface properties, enabling the design of dispersants, stabilizers, or surfactants to prevent aggregation and ensure optimal particle dispersion in various applications. The Zeta potential of precipitation surfaces with different agents at pH values of 6.0-10.0 were depicted in Fig. 59, where P, F, and C represent precipitation, flocculant, and collector, respectively. As can be seen, the precipitation surface is negatively charged in the pH range of 6.0 to 10.0, and the zeta potential increased negatively with the increasing pH. The changes in surface potential of precipitation particles after treatment of agents are basically the same at the same pH, thus the pH of 10.0 was selected to discuss. At pH=10.0, the zeta potential of the precipitated particles with flocculant increased negatively from -5.04 mV to -10.93 mV, which indicated that the anionic flocculant was adsorbed on the surface of the precipitated particles. After reacting with A-100 followed by NaOL, the zeta potential further

shifted negatively to -12.23 mV, indicating that NaOL were also adsorbed on the surface of precipitated particles on the basis of A-100 pre-adsorption.

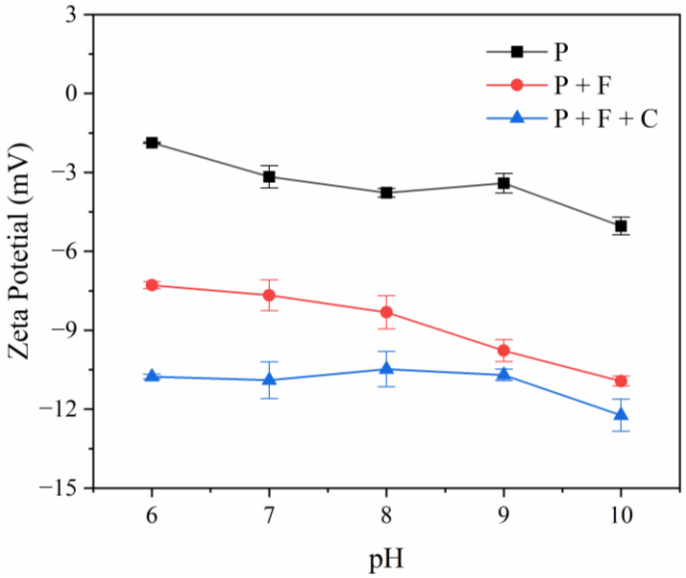


**Fig. 59.** Zeta potential of precipitation as a function of pH with different agents.

The FTIR spectrum of precipitation after being treated with flotation agents is depicted in Figures Fig**. 60**(a), Fig**. 60**(b), and Fig**. 60**(c), where P, F, and C represent precipitation, flocculant, and collector, respectively. In the spectrum of P+F, the new peak at 1450.20 $cm^{-1}$ was contributed to C-N stretching [48]. For P+C, four new peaks located at 2927.41, 2854.12, 1546.63, and 1469.49 $cm^{-1}$ were observed, of which 2927.41 and 2854.12 $cm^{-1}$ resulted from the asymmetric $CH_3$ stretching and asymmetric $CH_2$ stretching vibrations, respectively. The peaks at 1469.49 and 1546.63 $cm^{-1}$ were assigned to the symmetric C=O stretching and the asymmetric C−O stretching of NaOL, respectively [49, 50]. The two new adsorption peaks at 2931.26 and 1473.35 $cm^{-1}$ observed in spectrum of P+F+C were contributed to the asymmetric $CH_3$ stretching and the symmetric C=O stretching with shifts of +3.85 and +3.86 $cm^{-1}$, respectively. Meanwhile, the absorption peak of C-N stretching was absorbed and covered after adding NaOL. Therefore, combined with the negatively increasing zeta potential results, A-100 and NaOL both chemically adsorb on the surface of precipitate particles. Further, the possible adsorption mechanism of A-100 and NaOL on precipitation surface can be presented as Fig. 61.

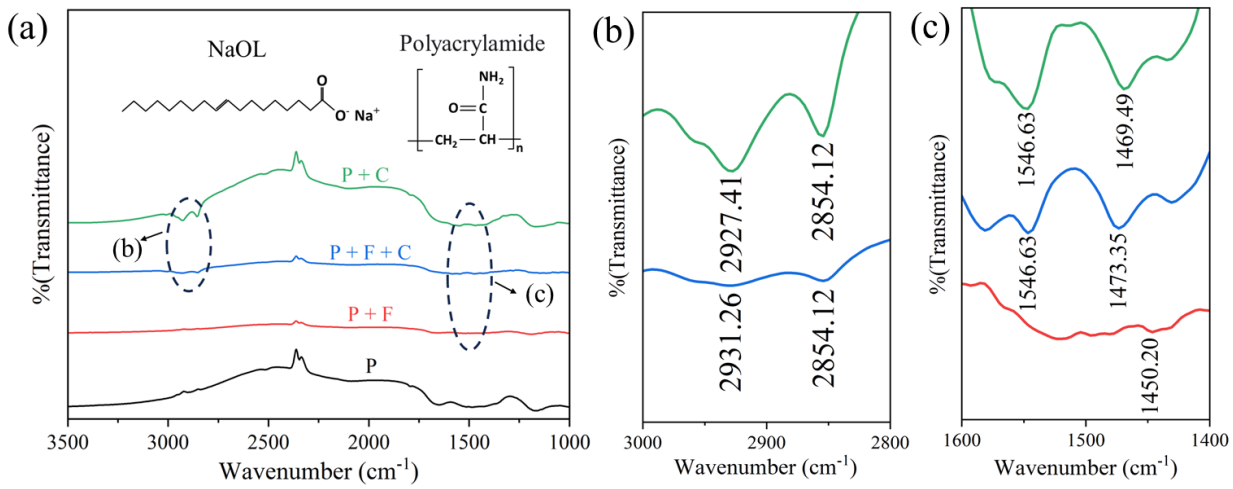


**Fig. 60.** FTIR spectra of precipitation with different agents in wavenumber range of (a) 3500-1000 $cm^{-1}$, (b) 3000-2800 $cm^{-1}$, and (c) 1600-1400 $cm^{-1}$.

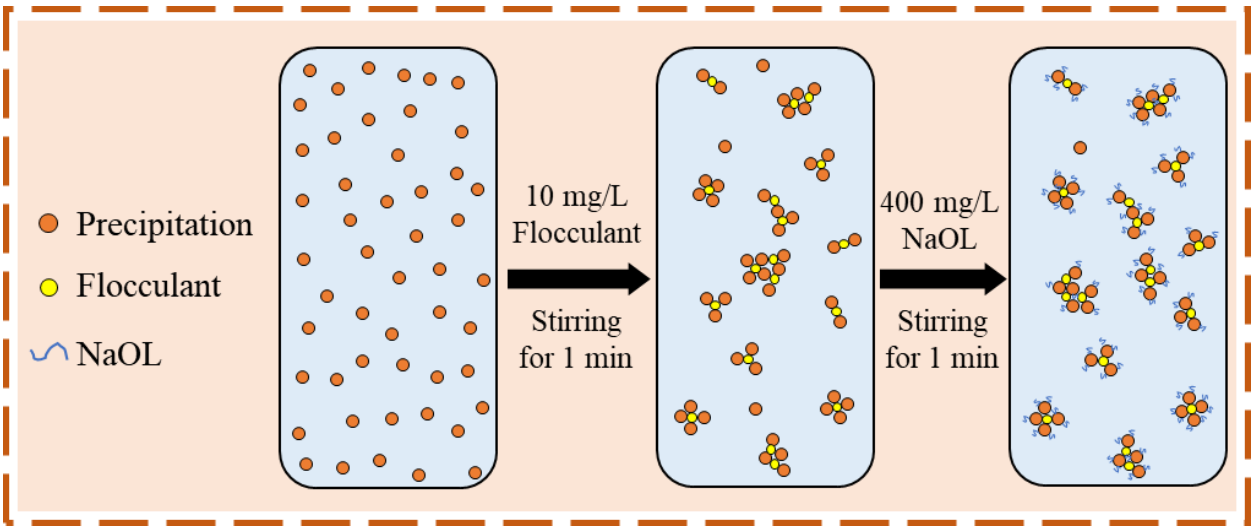


**Fig. 61.** Model diagram of the hydrophobic agglomeration process.

Consequently, it is confirmed that A-100 increased the apparent size of precipitated particles, thereby increasing the probability of collision between particles and bubbles. NaOL increased the hydrophobicity of the precipitation surface, thereby increasing the probability of adhesion between bubbles and precipitate particles. As a result, the floatability of precipitated particles is enhanced, and the removal of metal ions in AMD is more thorough.

To explain the agglomeration behavior of particles during flotation, the total interaction energies between precipitate particles adding 10 mg/L A-100 were calculated according to DLVO theoretical, which has been widely used to explain the agglomeration behavior of particles during

flotation. In this study, the total energy between precipitated particles can be described as (Yoon and Mao 1996):

$$V_{Total}^{D} = V_E + V_W \tag{211}$$

where $V_E$ and $V_W$ are electrostatic interaction energy and Van der Waals interaction energy, respectively.

The precipitated particles were assumed to be spherical, then the $V_E$ can be calculated as (Fu, Han et al. 2021):

$$V_E = 4\pi\varepsilon_0\varepsilon_r \frac{R_1 R_2}{R_1 + R_2} \psi_0^2 \ln\left[1 + e^{-\kappa H}\right] \tag{212}$$

where $\varepsilon_0$ is the permittivity of vacuum ($8.854 \times 10^{-12}$ C$^2$/J/m), $\varepsilon_r$ is absolute dielectric constant of water (78.54 at 25 °C) (Li, Liu and Liu 2018), $R_1$ and $R_2$ are radius of precipitated particles, which was assumed as $R_1 = R_2 = d_{50}/2 = 2.85$ μm in the calculation. $\psi_0$ is the surface potential of the precipitate particles, which can be approximated by zeta potential values. The radius of precipitated particles and the zeta potential values can be found in previous quarterly reports. H is the interaction distance between the particles. $\kappa^{-1}$ is the Debye length (nm), which can be calculated using classic Debye-Huckel theory (Eun 1996, Li, Liu and Liu 2018):

$$\kappa = \left[\frac{2e^2 N_A}{\varepsilon_0 \varepsilon_r k_B T} \sum_i c_i z_i^2\right]^{1/2} \tag{213}$$

where c is the ion strength in the medium, $e$ is the electronic charge ($1.602\times10^{-19}$ C), z is the ion valence, $k_B$ is the Boltzmann constant ($1.381\times10^{-23}$ J/K), $N_A$ is the Avogadro number ($6.023\times10^{23}$ mol$^{-1}$) T is the absolute temperature (K). $\kappa$ was calculated as $1.87\times10^{7}$ nm$^{-1}$.

When flotation reagents are adsorbed on the precipitation surface, the $V_W$ is calculated as (Fu, Han et al. 2021):

$$V_W = -\frac{1}{6}\frac{R_1 R_2}{R_1 + R_2}\left[\frac{A_{232}}{H} - \frac{2A_{123}}{H + \delta} + \frac{A_{121}}{H + 2\delta}\right] \tag{214}$$

where δ is the thickness of the adsorption layer, $A_{232}$, $A_{123}$ and $A_{121}$ can be obtained as follows:

$$A_{232} = (\sqrt{A_{22}} - \sqrt{A_{33}})^2 \tag{215}$$

$$A_{123} = (\sqrt{A_{11}} - \sqrt{A_{22}}) \times (\sqrt{A_{33}} - \sqrt{A_{22}}) \quad (216)$$

$$A_{121} = (\sqrt{A_{11}} - \sqrt{A_{22}})^2 \quad (217)$$

where $A_{11}$ is the Hamaker constant of precipitate in vacuum, which can be assumed as equal to hematite ($23.2\times10^{-20}$ J) (Li, Yin et al. 2017). $A_{22}$ is the Hamaker constant of the reagent in vacuum, polyacrylamide is $7.98\times10^{-20}$ J, and NaOL is $4.7\times10^{-20}$ J (Zou, Zhao and Sun 2018, Fu, Han et al. 2021). $A_{33}$ is the Hamaker constant of water in vacuum, $4.0\times10^{-20}$ J (Li, Cui et al. 2023).

Based on the equations (14), (15), (16), (17), (18), (19), and (29), the total interaction energies between precipitation with different agents were calculated and illustrated in Fig. 62. The negative interaction energy illustrates the existence of attraction energy among particles, while the positive interaction energy indicates repulsion energy. Upon the introduction of flocculant, the $V_{Total}^{D}$ between precipitation particles were negative as the interaction distance was less than 10 nm, confirming the existence of attraction energy. The curve exhibited positive energy between distances of 10 to 130 nm, indicating a repulsion between precipitation particles. The observed energy barrier was $2.34\times10^{-19}$ J, indicating extra energy input is required. In this case, the energy barrier was overcome through the collaborative action of stirring, leading to the flocculation of the precipitate particles.

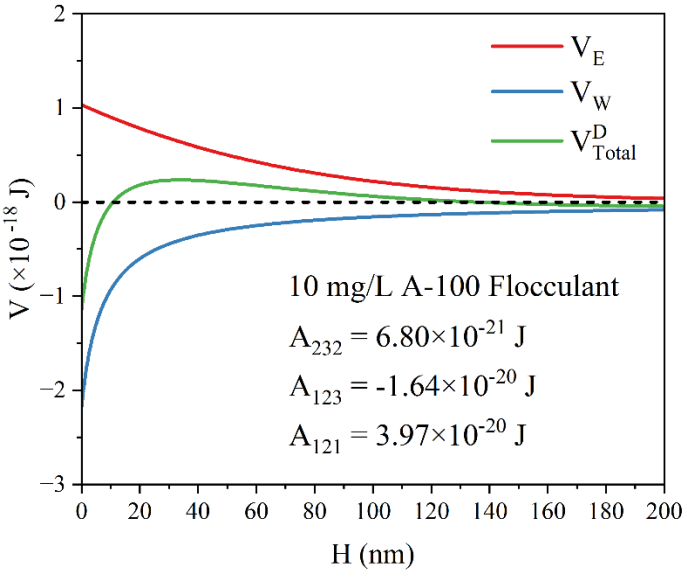

**Fig. 62.** Interaction energy between precipitation particles as a function of interaction distance with addition of 10 mg/L A-100.

## 4. PROJECT OUTPUTS

### Journal Articles

Liu, P., Wang, X., & Zhang, W. (2025). The development of an efficient precipitation-flotation-dewatering (PFD) process for acid mine drainage treatment. Separation and Purification Technology, 353, 128542.

### Peer-Reviewed Conference Articles

Not available.

### Non-Reviewed Conference Articles

Not available.

### Abstract & Conference Presentation

MINEXCHANGE 2024 SME Annual Conference & Expo / Poster title: The Development of a Novel Precipitation-Flotation-Dewatering (PFD) Process for Acid Mine Drainage Treatment / (02/25/2024 – 02/28/2024).

### Other Publication Products

Not available.

### Patent & Patent Applications

Not available.

## 5. FOLLOW-ON FUNDING

Not available.

## 6. CHANGES/PROBLEMS

Not available.

## 7. SPECIAL REPORTING REQUIREMENTS

Not available.

## 8. ACKNOWLEDGEMENT

## REFERENCES


Ai, C., S. Hou, Z. Yan, X. Zheng, C. Amanze, L. Chai, G. Qiu and W. Zeng (2020). "Recovery of Metals from Acid Mine Drainage by Bioelectrochemical System Inoculated with a Novel Exoelectrogen, Pseudomonas sp. E8." Microorganisms **8**(1): 41.

Amrou, R. (2020). Évaluation de L'utilisation des mélanges Till-Boues de Traitement du Dma Comme Couche de rétention D'humidité Dans un Recouvrement de Type CEBC M.A.Sc., Ecole Polytechnique, Montreal (Canada).

Aubé, B. and M. Sc (2004). "The Science of Treating Acid Mine Drainage and Smelter Effluents."

Aubé, B. C. (1999). "Innovative Modification to High Density Sludge Process." Proceedings for Sudbury '99, Mining and the Environment II.

Aubé, B. C. and J. M. Zinck (1999). Comparison of AMD treatment processes and their impact on sludge characteristics. proceedings for Sudbury.

Cheng, G., M. Zhang, Y. Cao, Y. Lu, Y. Feng and S. Zhao (2020). "Preparation and evaluation of lignite flotation collector derived from waste hot-pot oil." Fuel **267**: 117138.

Eun, H.-M. (1996). 1 - Enzymes and Nucleic Acids: General Principles. Enzymology Primer for Recombinant DNA Technology. H.-M. Eun. San Diego, Academic Press**:** 1-108.

Fan, G., M. Zhang, W. Peng, G. Zhou, L. Deng, L. Chang, Y. Cao and P. Li (2021). "Clean products from coal gasification waste by flotation using waste engine oil as collector: Synergetic cleaner disposal of wastes." Journal of Cleaner Production **286**: 124943.

Fu, J., H. Han, Z. Wei, W. Sun and T. Yue (2021). "Recovery of ultrafine scheelite particles by magnetic seeding flocculation and its mechanism." Colloids and Surfaces A: Physicochemical and Engineering Aspects **628**: 127266.

Herrera, P., H. Uchiyama, T. Igarashi, K. Asakura, Y. Ochi, N. Iyatomi and S. Nagae (2007). "Treatment of acid mine drainage through a ferrite formation process in central Hokkaido, Japan: Evaluation of dissolved silica and aluminium interference in ferrite formation." Minerals Engineering **20**(13): 1255-1260.

Kefeni, K. K., T. A. M. Msagati and B. B. Mamba (2017). "Acid mine drainage: Prevention, treatment options, and resource recovery: A review." Journal of Cleaner Production **151**: 475-493.

Kuyucak, N. (2021). "Water in Mining and Environment for Sustainability." Mine Water and the Environment **40**(4): 815-817.

Li, D., W. Yin, Q. Liu, S. Cao, Q. Sun, C. Zhao and J. Yao (2017). "Interactions between fine and coarse hematite particles in aqueous suspension and their implications for flotation." Minerals Engineering **114**: 74-81.

Li, H., M. Liu and Q. Liu (2018). "The effect of non-polar oil on fine hematite flocculation and flotation using sodium oleate or hydroxamic acids as a collector." Minerals Engineering **119**: 105-115.

Li, W., Y. Cui, Z. Pan, F. Jiao, C. Yang, X. Wang, Z. Zhang and W. Qin (2023). "Hydrophobic agglomeration flotation of fine cassiterite induced by kerosene and sodium oleate." Powder Technology.
Mapukata, S., K. Mudzanani, N. M. Chauke, D. Maiga, T. Phadi and M. Raphulu (2024). "Acid Mine Drainage Treatment and Control: Remediation Methodologies, Mineral Beneficiation and Water Reclamation Strategies."
Matlock, M. M., B. S. Howerton and D. A. Atwood (2002). "Chemical precipitation of heavy metals from acid mine drainage." Water research **36**(19): 4757-4764.
Mondejar, M. E., R. Avtar, H. L. B. Diaz, R. K. Dubey, J. Esteban, A. Gómez-Morales, B. Hallam, N. T. Mbungu, C. C. Okolo, K. A. Prasad, Q. She and S. Garcia-Segura (2021). "Digitalization to achieve sustainable development goals: Steps towards a Smart Green Planet." Science of The Total Environment **794**: 148539.
Motsi, T., N. Rowson and M. Simmons (2009). "Adsorption of heavy metals from acid mine drainage by natural zeolite." International journal of mineral processing **92**(1-2): 42-48.
Mulopo, J. (2015). "Continuous pilot scale assessment of the alkaline barium calcium desalination process for acid mine drainage treatment." Journal of Environmental Chemical Engineering **3**(2): 1295-1302.
Peiravi, M., S. R. Mote, M. K. Mohanty and J. Liu (2017). "Bioelectrochemical treatment of acid mine drainage (AMD) from an abandoned coal mine under aerobic condition." Journal of Hazardous Materials **333**: 329-338.
Salo, M. and M. Bomberg (2022). "Sulfate-reducing bioreactors subjected to high sulfate loading rate or acidity: variations in microbial consortia." AMB Express **12**(1): 95.
Van Rooyen, M., P. van Staden and K. du Preez (2021). "Sulphate removal technologies for the treatment of mine-impacted water." Journal of the Southern African Institute of Mining and Metallurgy **121**(10): 523-530.
Yoon, R.-H. and L. Mao (1996). "Application of Extended DLVO Theory, IV: Derivation of Flotation Rate Equation from First Principles." Journal of Colloid and Interface Science **181**(2): 613-626.
Zou, W., J. Zhao and C. Sun (2018) "Adsorption of Anionic Polyacrylamide onto Coal and Kaolinite Calculated from the Extended DLVO Theory Using the van Oss-Chaudhury-Good Theory." Polymers **10** DOI: 10.3390/polym10020113.